AN ABSTRACT OF THE THESIS OF

Rainer D. Beck for the degree of Doctor of Philosophy in
Chemistry presented on August 25, 1989
Title: High Resolution Stimulated Raman Spectroscopy

Abstract approved: Redacted for Privacy
Professor Joseph W. Nibler

The high resolution stimulated Raman spectrometer at OSU was modified to improve its sensitivity and to extend its range of applications to low Raman shifts and to the spectroscopy of solids and liquids. As part of the characterization of the spectrometer, optical Stark effects on rotational and vibrational transitions of N_2 were investigated and the pure rotational spectrum of C_4N_2 was recorded for the first time.

Stimulated Raman spectroscopy (SRS) was used for the first time for high resolution Raman spectroscopy of cold molecular liquids and crystals. Accurate measurements of the linewidth and the Raman shift for the very narrow vibrational transition in condensed nitrogen (liquid, solid-β, and solid-α phases) were made between 110 and 15 K. These measurements establish the temperature dependence of the N_2 vibrational frequency and linewidth for the condensed phases and show the effect of the phase transitions on the vibrational Raman spectrum.

This data was used in the analysis of SRS spectra of large N_2

clusters formed in free jet expansions which were observed for the first time with the SRS technique. By probing at different points along the axis of the expansion changes in the vibrational Raman spectrum are observed which signify the formation of liquid aggregates, followed by strong supercooling and subsequent freezing to the solid beta phase. High spatial resolution of the SRS probing results in good time resolution for the observation of the extremely fast condensation and freezing phase transitions. Aggregate temperatures are determined by using the temperature dependence of the vibrational frequency measured in the static samples and the assumption that the observed clusters are large enough to be treated as bulk material. That this assumption is valid is shown by several independent size estimates which indicate that the means cluster diameter is in the range of 50 - 500 nm. Monomer temperatures are determined from the rotational Q-branch structure and the extent of aggregation is found to be about 10 % from the relative Raman intensity of monomer and cluster spectra. The results show that SRS offers unique diagnostic capabilities for the study of condensation processes in free jet expansions.

High Resolution Stimulated Raman Spectroscopy

by

Rainer D. Beck

A THESIS

submitted to

Oregon State University

in partial fulfillment of
the requirements for the
degree of

Doctor of Philosophy

Completed August 25, 1989

Commencement June 1990

APPROVED:

Redacted for Privacy

Professor of Chemistry in charge of major

Redacted for Privacy

Head of department of Chemistry

Redacted for Privacy

Dean of Graduate School

Date thesis is presented August 25, 1989

Typed by researcher for Rainer D. Beck

To my mother

ACKNOWLEDGEMENTS

I would like to thank my research adviser Dr. Joseph W. Nibler for his guidance and support over the last four years. I admire his creativity and enthusiasm, and I am grateful for the freedom that he gave me both in scientific matters and also with my many other interests. His example taught me to be methodical and patient, but at the same time, always to keep my eyes open for the unexpected. Finally, he confirmed the suspicion that I had for a long time: that science can, besides being hard work, be very exciting and a lot of fun.

I also want to thank Dr. George Pubanz for getting me started with the stimulated Raman spectrometer and for instilling a healthy respect for the ring dye laser in me right from the beginning. I appreciate the cooperation of Kirk Brown on the pure rotational spectroscopy of C_4N_2 and of Dr. Max Hineman on the spectroscopy of some of the condensed phase samples. I am grateful to everybody in our group for contributing to a friendly atmosphere that made it fun to work in.

TABLE OF CONTENTS

TABLE OF CONTENTS (cont.)

LIST OF FIGURES

LIST OF FIGURES (cont.)

FIGURES (cont.)

LIST OF TABLES

HIGH RESOLUTION STIMULATED RAMAN SPECTROSCOPY

CHAPTER I: INTRODUCTION

The research described in this thesis is centered on the development of new applications of high resolution stimulated Raman spectroscopy (SRS) for the study of condensed phase samples and molecular aggregates formed in free jet expansions.

Chapter I briefly introduces the field of nonlinear Raman spectroscopy and gives an account of the historical development of the stimulated Raman technique. Chapter II presents the theoretical background information on stimulated Raman scattering, Raman lineshapes, and free jet expansions. A description of the experimental setup is given in chapter III together with representative gas phase spectra taken with the SRS spectrometer. Chapter IV describes the extension of the SRS spectrometer to the low shift region and reports the results of a study of the pure rotational Raman spectrum of C_4N_2. Chapter V shows the previously unexploited potential of SRS for the high resolution spectroscopy of very narrow Raman transitions in condensed molecular phases. As a first example and test case the vibrational spectrum of N_2 was studied in its various condensed phases. Finally, another first time application of SRS, described in chapter VI, is the successful detection of aggregation of N_2 in free jet expansions. The results presented in chapter VI show that SRS is capable of monitoring the internal temperature and the phase of the N_2 aggregates in the jet expansion.

NONLINEAR RAMAN SPECTROSCOPY

Raman spectroscopy started with the discovery of the Raman effect in 1928 by the Indian physicist Sir Chandrasekharan V. Raman[1]. The Raman effect is a form of inelastic light scattering in which the scattering molecules receive or give up part of their internal energy. Since Raman spectroscopy complements the information from infrared absorption spectra in many cases, it was soon established as a method for molecular structure determination as well as an analytical technique. However, an inherent problem of the technique, the weakness of the effect, was only overcome after lasers were invented in the early 1960's which led to a period of rebirth in conventional Raman spectroscopy. Experiments with lasers also led to the first observation of nonlinear optical effects several of which are related to Raman scattering.

Woodbury and Ng[2] observed in 1962 that, when a powerful laser beam propagates through a medium, laser-like light at new frequencies is generated in a stimulated Raman process. In this process the Raman shifted wave becomes strong enough that it couples to the incident laser beam through the nonlinear polarizability of the medium. Because of this coupling the Raman shifted wave is amplified coherently which leads to a directed emission of frequency-shifted laser radiation. Variations of the stimulated Raman effect are the Raman gain and Raman loss processes, schematically depicted in Fig. I.1, the latter of which is sometimes referred to as inverse Raman scattering. Here two laser beams are incident on the medium and the stimulated Raman effect leads to an amplification of the beam at lower

Spontaneous Raman Scattering

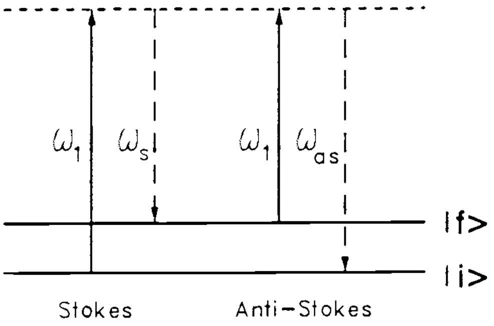

Stimulated Raman Scattering

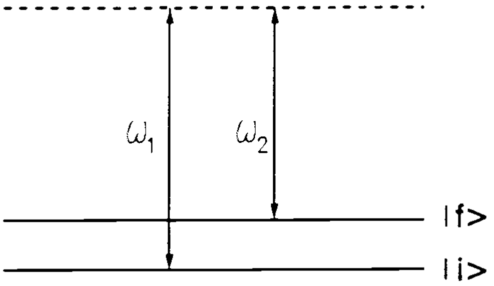

Raman Gain Spectroscopy if increase in ω_2 is monitored
Raman Loss Spectroscopy if decrease in ω_1 is monitored

Coherent Anti-Stokes Raman Scattering CARS

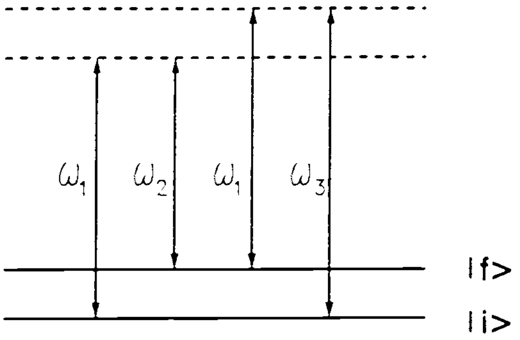

CARS: input frequencies ω_1, ω_2 ; signal frequency: $\omega_3 = 2\omega_1 - \omega_2$
CSRS: input frequencies ω_1, ω_3 ; signal frequency: $\omega_2 = 2\omega_1 - \omega_3$

Figure I.1: Energy level diagrams depicting the various Raman processes discussed in the text.

frequency (Raman gain) accompanied by a attenuation of the higher frequency beam (Raman loss) when the frequency difference matches a Raman active transition of the molecule. Either one of these effects can be used to record the Raman spectrum of the medium as the frequency difference is tuned across the Raman resonances. Since Raman gain and loss always occur simultaneously, a distinction between the effects is somewhat artificial which is why we will refer to both processes as stimulated Raman spectroscopy (SRS) in the remainder of this thesis.

Two other nonlinear Raman effects are coherent anti-Stokes Raman scattering (CARS) and its counterpart coherent Stokes Raman scattering (CSRS) which are also shown in Fig. I.1. Here three incident waves couple to produce coherent radiation at a new frequency.

Coherent Raman spectroscopy offers several advantages over conventional, spontaneous (incoherent) Raman spectroscopy, which are listed below:

- Much larger signal is generated for a given incident laser power.
- Signal is contained in a coherent laser beam which can be detected more efficiently than random scattering into the full 4π solid angle.
- Resolution is determined by the laser linewidth; not by the monochromator.
- Discrimination against fluorescence can be achieved by detecting an anti-Stokes signal that is higher in frequency than both incident laser beams (and all fluorescence caused by these beams).

These advantages led to the development of a series of nonlinear Raman techniques which are distinguished mainly by the way in which the Raman resonance is detected. The following discussion is limited to the stimulated Raman technique which was used in the research described in this thesis since it is especially well suited for high resolution spectroscopy.

HISTORICAL DEVELOPMENT OF STIMULATED RAMAN SPECTROSCOPY

The first observation of the inverse Raman effect was reported by Jones and Stoicheff[3] in 1964. Although they pointed out the potential value of this effect as a spectroscopic technique, the lack of tunable lasers with narrow linewidth prevented the spectroscopic application of SRS for more than a decade. One exception to this is the work of Lallemand et al.[4] (1966) who used a pressure-tuned hydrogen Raman shifter to record the Raman spectrum of H_2 in a second cell with very high resolution. This approach can not be easily extended to other molecules because they lack the fortuitous combination of large Raman cross section and narrow high-pressure linewidth found for H_2.

Until the early 1970's when the first dye lasers became available, the main applications of SRS were frequency conversion methods in which molecules like H_2 and CH_4 were used to Raman-shift laser lines. After 1972 a few applications of SRS are reported in the literature (Reinhold and Maier[5] 1972), (Kincaid and Fontana[6] 1976) but the systematic development of SRS as a tool for high resolution Raman spectroscopy didn't start until 1977 when Owyoung and Jones introduced the CW-SRS technique[7].

CW-SRS combines the use of a highly stable tunable CW dye laser with lock-in detection to succeed in detecting transmission changes as small as 10^{-7}. This provided sufficient sensitivity to record SRS spectra of a variety of liquid samples. By using a multipass cell Owyoung and Esherick were able to further increase the sensitivity and record the first fully resolved Q-branch spectrum of the υ_1 mode in methane at 35 torr. This constitutes the first case where SRS provided spectroscopic information which was not available from spontaneous Raman spectroscopy and thereby establishes the significance of SRS as a precision tool for Raman spectroscopy. The outstanding property of CW-SRS is its extremely high resolution which is only limited by the laser linewidths. With CW lasers linewidths of a few MHz are easily achievable and most recent developments show that solid state lasers can be built that approach the theoretical Townes limit of less than one Hz linewidth. In order to exploit this very high resolution one has to use samples of very low pressure and temperature to reduce collisional and Doppler broadening, conditions which can be achieved in a free jet expansion. Unfortunately, due to the low laser power, the sensitivity of CW-SRS is insufficient to record spectra under these conditions.

A major improvement in the sensitivity of SRS was made possible through the quasi-CW technique developed by Esherick and Owyoung in 1980[8]. Quasi-CW SRS uses a high power pulsed pump laser and a CW probe laser which is chopped to avoid saturation of the detector. By using a pulsed pump laser one gives up some of the resolution compared to the CW-SRS method since the transform width of the pump laser (60 MHz for 10 nsec pulse) limits the resolution. However, one gains significantly in sensitivity because of the high pump laser power. Assuming a 1 MW, 10 nsec pump pulse and a 250 mW CW probe laser, one estimates a sensitivity improvement of 10^4 relative to a CW system. Another advantage of quasi-CW SRS, besides the higher pump power, is that the Raman signal consists of a fast, transient dip in the probe laser power of 10 nsec duration which can be ac-coupled into a boxcar averager. By using a high pass filter with a cutoff above 10 MHz one can achieve near quantum limited sensitivity since the main amplitude noise contributions of CW single mode ion lasers are at frequencies below this cutoff.

Owyoung and Esherick have used quasi-CW SRS to record completely resolved Q-branch spectra of several polyatomic molecules (SF_6, SiH_4, CD_4)[9,10,11] which was not possible with conventional Raman methods since the very closely spaced lines in these spectra require very low density samples (1-4 torr) and very high resolution simultaneously. Other groups have used high resolution quasi-CW SRS to get accurate measurements of Raman linewidths and lineshapes at various pressures and temperatures[12,13]. This data is used to develop accurate models of Raman spectra which are needed in remote sensing applications of hostile environments like flames, combustion engines, and the exhaust flame of a jet engine, where a related nonlinear Raman technique (CARS) has been shown to be extremely useful.

Other applications of SRS include the study of biochemical fluorophores in solutions (Morris[14]) where the ability of SRS to discriminate against sample fluorescence is exploited, the work of Heritage et al.[15] who showed that SRS is sensitive enough to detect monolayer films of benzene on a sapphire substrate, and time resolved experiments using SRS to study dephasing processes in liquids and solids.[16,17]

Still higher sensitivity than in quasi-CW SRS was achieved by combining SRS in a double resonance experiment with either photo-ionization or fluorescence excitation. In these experiments the stimulated Raman process populates an upper vibrational-rotational level which is then selectively excited to a higher electronic state. In this way the highly sensitive techniques of ionization detection or laser induced fluorescence (LIF) can be used to record Raman spectra. The price for the increased sensitivity is the added complexity of the experiments because of the need for a second tunable UV laser source necessary for most simple molecules. Esherick and Owyoung developed the ionization detection version (IDSRS)[18] and demonstrated a 1000 fold improvement in sensitivity by recording the Q-branch spectrum of NO at 0.01 torr. They attained a tenfold better signal/noise ratio than a spectrum recorded with the quasi-CW technique at 1 torr. They also showed that IDSRS can be used in a free jet expansion where they recorded the rovibrational spectrum of the degenerate Fermi dyad υ_{16} and $\upsilon_2+\upsilon_{18}$ of benzene.[19] Orr[20] and coworkers have used LIF detection in a scheme which they call Raman-LIFDR to study the υ_2 vibration of D_2CO and showed similar sensitivity improvements. Finally, still another version of a double resonance nonlinear Raman technique was reported by Bronner[21] et al. who ionized ground state molecules in a free jet expansion and monitored a decrease in the ion current when a second laser was tuned so that molecules were Raman pumped into an excited vibrational state. They demonstrated an "ion-dip" signal from the Q-branch of the υ_1 band of benzene in a free jet expansion at a density of 10^{11} molecules/cm^3 or a pressure of $3 \cdot 10^{-6}$ torr.

CHAPTER II: THEORETICAL BACKGROUND

1. STIMULATED RAMAN SCATTERING

Nonlinear Optics

Stimulated Raman scattering is one of many nonlinear optical effects that have been observed since the invention of the laser. Nonlinear optical effects can be defined as the area of optical phenomena which arise from a nonlinear response of the material to an applied electromagnetic field. Since these nonlinear effects are usually weak enough that only the coherent radiation from a large number of molecules is detectable, a semi-classical theory is satisfactory. In the semi-classical approach the electromagnetic field is treated classically, whereas the material is described by quantum mechanics. A thorough theoretical description of nonlinear optical effects was first given by Bloembergen[22]. A large amount of literature was published subsequently on the theory of the various nonlinear Raman effects. The following discussion of stimulated Raman scattering is based on review articles by Jones[23,24] and Nibler[25,26] and references cited therein.

Light-Matter Interaction

The interaction between light and matter takes place, to first order, through the coupling of the electromagnetic field with the charges present in the material. The field can distort the charge distribution in the material and thereby cause a polarization. Nonlinear parts in the response of the medium become important at high field intensities and are able to couple the applied fields causing energy transfer between waves and generation of new frequencies through mixing processes. These effects can be treated quantitatively within the framework of Maxwell's equations. These are, written in the microscopic form, in cgs units:

$$\nabla \times \mathbb{E} = -\frac{1}{c}\frac{\partial \mathbb{B}}{\partial t} \qquad (1.1) \qquad\qquad \nabla\cdot\mathbb{E} = 4\pi\rho \qquad (1.2)$$

$$\nabla \times \mathbb{B} = \frac{4\pi\mathbb{J}}{c} + \frac{1}{c}\frac{\partial \mathbb{E}}{\partial t} \qquad (1.3) \qquad\qquad \nabla\cdot\mathbb{B} = 0 \qquad (1.4)$$

If there are no extra charges, other than those bound in the molecules, we can substitute for the electric charge density $\rho = -\nabla\cdot\mathbb{P}$ and for the electric current density $\mathbb{J} = \partial\mathbb{P}/\partial t$. By taking the curl of equation (1) we get:

$$\nabla \times (\nabla \times \mathbb{E}) = -\frac{1}{c^2}\frac{\partial}{\partial t}(\nabla \times \mathbb{B}) \qquad (1.5)$$

If we substitute for $\nabla \times \mathbb{B}$ using equation (3) we get a wave equation that contains the polarization $\mathbb{P}$ as a source term.

$$\nabla \times (\nabla \times \mathbb{E}) + \frac{1}{c^2}\frac{\partial^2\mathbb{E}}{\partial t^2} = -\frac{4\pi}{c^2}\frac{\partial^2\mathbb{P}}{\partial t^2} \qquad (1.6)$$

The remaining problem is now to write the polarization $\mathbb{P}$ in terms of the electric field $\mathbb{E}$ and to find solutions of the wave equation. For simplicity we will restrict the derivation to plane waves propagating in the z direction. The time dependence of the wave equation can be removed by a Fourier transformation into frequency space:

$$E(z,t) = \int_{-\infty}^{+\infty} \exp[-i\omega t]\;\; E(z,\omega)\;\; d\omega \qquad (1.7)$$

$$P(z,t) = \int_{-\infty}^{+\infty} \exp[-i\omega t] \; P(z,\omega) \; d\omega \tag{1.8}$$

For plane waves in an isotropic medium the following simplification can be made: $\nabla\times(\nabla\times\mathbb{E}) = -\frac{\partial^2 E}{\partial z^2}$ which simplifies the wave equation to:

$$\frac{\partial^2 E(z,\omega)}{\partial z^2} + \frac{\omega^2}{c^2} E(z,\omega) = -\frac{4\pi\omega^2}{c^2} P(z,\omega) \tag{1.9}$$

If we make use of the definition for the linear susceptibility we can isolate the nonlinear polarization on the right side of the wave equation:

$$\mathbb{P} = \mathbb{P}^{lin} + \mathbb{P}^{nl} = \chi^{(1)}\mathbb{E} + \mathbb{P}^{nl} = \frac{(\varepsilon-1)}{4\pi} \mathbb{E} + \mathbb{P}^{nl} = \frac{(n^2-1)}{4\pi} \mathbb{E} + \mathbb{P}^{nl} \tag{1.10}$$

$$\frac{\partial^2 E(z,\omega)}{\partial z^2} + \frac{\omega^2}{c^2} E(z,\omega) = -\frac{(n^2-1)}{c^2} \omega^2 E(z,\omega) - \frac{4\pi\omega^2}{c^2} P^{nl}(z,\omega) \tag{1.11}$$

$$\frac{\partial^2 E(z,\omega)}{\partial z^2} + k^2 E(z,\omega) = -\frac{4\pi k^2}{n^2} P^{nl}(z,\omega) \tag{1.12}$$

where the relation for the wave vector k was used $k^2 = \frac{\omega^2 n^2}{c^2}$.

The source polarization on the right side of the wave equation depends on the frequencies, phases and polarizations of the pump fields; its properties (more precisely the tensor and spectral properties of the susceptibility tensors $\chi^{(n)}$) are directly reflected in the growth and polarization properties of the signal wave. For instance, by tuning the applied field frequencies and monitoring the resultant changes in the signal amplitude, one performs nonlinear optical spectroscopy of the medium. Before we go into the details of stimulated Raman spectroscopy we need to look at the properties of the susceptibility of a medium and how its macroscopic and microscopic properties are reflected in it.

Nonlinear Susceptibility

With strong electric fields as for example in the focus of a laser beam, it is not sufficient to assume a linear response of the material to the field as is done in the simple Lorentz model of the index of refraction. A common, more general, approach is to express the polarization as a vectorial Taylor series expansion in the applied field $\mathbb{E}$.

$$\mathbb{P} = \chi^{(1)} \cdot \mathbb{E} + \chi^{(2)} \cdot \mathbb{E}\cdot\mathbb{E} + \chi^{(3)} \cdot \mathbb{E}\cdot\mathbb{E}\cdot\mathbb{E} + \ldots \qquad (1.13)$$

From this expression it can be seen how nonlinearities can give rise to new frequencies. If we, for instance, take an incident field with frequency ω, $\mathbb{E} = \mathbb{E}_0\cdot\cos(\omega t)$, then the second order contribution has a dc-component and a component oscillating at 2ω :

$$\mathbb{P}^{(2)} \sim \mathbb{E}^2 = \mathbb{E}_0^2 \frac{1}{2} \{ 1 + \cos(2\omega t)\} \qquad (1.14)$$

Even more frequencies arise when $\mathbb{E}$ itself contains more than one frequency. In this case it is convenient to write the applied electric field as the sum of its quasi monochromatic Fourier components with frequencies ω_j:

$$\mathbb{E} = \frac{1}{2} \sum_j \{ \mathbb{E}_j \exp[i(k_j z - \omega_j t)] + \text{c.c.} \} \qquad (1.15)$$

The resulting polarization, with frequency components at ω_p can then be expanded in this field. The first three terms are:

$$\mathbb{P}^{(1)} = \frac{1}{2} \sum_j \chi^{(1)}(-\omega_p, \omega_j)\, \mathbb{E}_j \cdot \exp[i(k_j\cdot z - \omega_j t + \Phi_j)] \qquad (1.16)$$

$$\mathbb{P}^{(2)} = \frac{1}{2} \sum_{j,l} \chi^{(2)}(-\omega_p, \omega_j, \omega_l)\, \mathbb{E}_j\, \mathbb{E}_l \cdot \exp[i\{(k_j+k_l)z - (\omega_j+\omega_l)t + (\Phi_j+\Phi_l)\}] \qquad (1.17)$$

$$\mathbb{P}^{(3)} = \frac{1}{2} \sum_{j,k,l} \chi^{(3)}(-\omega_p,\omega_j,\omega_k,\omega_l)\ \mathbb{E}_j\ \mathbb{E}_k\ \mathbb{E}_l \cdot \exp[i\{(k_j+k_k+k_l)z - (\omega_j+\omega_k+\omega_l)t + (\Phi_j+\Phi_k+\Phi_l)\}] \qquad (1.18)$$

The coefficients $\chi^{(n)}$ are the n-th order susceptibility tensors and the ϕ_i's are the mutual phase factors usually set to zero. Each susceptibility is a tensor of rank n+1.

$\chi^{(1)}$ is related to the dielectric constant which describes absorption and refractive effects: $\varepsilon = 1 + 4\pi\chi^{(1)}$.

$\chi^{(2)}$ and all higher even order terms vanish in isotropic media such as gases, liquids, and centro-symmetric crystals. However, in systems without a center of symmetry, $\chi^{(2)}$ is responsible for second harmonic generation (SHG), the Pockels effect, and the piezo effect.

$\chi^{(3)}$ is the first nonlinear term which is nonzero for all media. It is responsible for the coherent Raman effects discussed in this thesis as well as a number of other nonlinear effects such as third harmonic generation, self-focusing, and the Kerr effect.

Macroscopic Properties of $\chi^{(3)}$

The third order susceptibility $\chi^{(3)}$, "chi-three", is a fourth rank tensor that gives a macroscopic description of the nonlinear response of a medium to an applied electric field. $\chi^{(3)}$ has 81 components, of which only a few are independent in systems with symmetry. Levenson[27] has tabulated the nonzero elements for different crystal classes. For liquids and gases, only three susceptibility terms are independent:

$$\chi^{(3)}_{1111}, \chi^{(3)}_{1122}, \chi^{(3)}_{1212}, \chi^{(3)}_{1221}$$

with: $$\chi^{(3)}_{1111} = \chi^{(3)}_{1122} + \chi^{(3)}_{1212} + \chi^{(3)}_{1221}$$

If the input laser beams propagate along the z-axis and θ_i defines the polarization of E_i with respect to the x-axis, the general form for the induced polarization[1] is:

$$\begin{aligned} P^{(3)}_x(r,\omega_3) = D \cdot \Big[& \chi^{(3)}_{1111} \cos\theta_0 \cos\theta_1 \cos\theta_2 + \\ & \chi^{(3)}_{1122} \cos\theta_0 \sin\theta_1 \sin\theta_2 + \\ & \chi^{(3)}_{1212} \sin\theta_0 \cos\theta_1 \sin\theta_2 + \\ & \chi^{(3)}_{1221} \sin\theta_0 \sin\theta_1 \cos\theta_2 \Big] \\ & E_0 E_1 E_2 \exp[\, i(k_0 + k_1 + k_2)\, z \,] \end{aligned} \tag{1.19}$$

with $D = \frac{6}{n!}$ where n is the number of degenerate frequencies in the four wave mixing process. To avoid confusion it should be noted that the indices used in $\chi^{(3)}_{iiii}$ describe the cartesian coordinates of a fourth rank tensor i.e. $\chi^{(3)}_{1111} = \chi^{(3)}_{xxxx}$, whereas the indices on the electric fields are used to label frequency and polarization direction.

From this expression one can derive which components of $\chi^{(3)}$ contribute to the signal for different choices of polarizations in various nonlinear Raman experiments. For Raman gain spectroscopy $\omega_0 = -\omega_1$ and $\omega_3 = -\omega_2$ since one monitors the ω_2 beam ($\omega_1 > \omega_2$). In this case the relevant nonlinear polarization is:

---

[1] Note that the term "polarization" is used here with two different meanings. The polarization of the electric field describes the orientation of the electric field vector whereas the induced polarization in the material describes the induced dipole moment per unit volume.

$$
\begin{aligned}
P^{(3)}(z,\omega_2) &= 6\,\chi^{(3)}(-\omega_2,-\omega_1,\omega_1,\omega_2)\; E_1 E_1^{*} E_2 \;\exp[ik_2 z] \\
&= \chi_{SRG}\; E_1 E_1^{*} E_2 \;\exp[ik_2 z] \qquad (1.20)
\end{aligned}
$$

In the Raman loss case the polarization component at ω_1 is relevant:

$$
\begin{aligned}
P^{(3)}(z,\omega_1) &= 6\,\chi^{(3)}(-\omega_1,-\omega_2,\omega_1,\omega_2)\; E_1 E_2 E_2^{*} \;\exp[ik_1 z] \\
&= \chi_{SRL}\; E_1 E_2 E_2^{*} \;\exp[ik_1 z] \qquad (1.21)
\end{aligned}
$$

Table (II.1.1) shows which components of $\chi^{(3)}$ are sampled for different polarization of the two incident beams.

E_1	E_2	$D\,\chi^{(3)}_{SRS}(-\omega_3,\omega_0,\omega_1,\omega_2)$
↑	↑	$6\,\chi^{(3)}_{1111}$
→	↑	$6\,\chi^{(3)}_{1221}$
↗	→	$3\left[\chi^{(3)}_{1122} + \chi^{(3)}_{1212}\right]$
↻	→	$3\left[\chi^{(3)}_{1122} - \chi^{(3)}_{1212}\right]$

Stimulated Raman Amplitudes

Still in the macroscopic, classical picture one can derive an expression for the stimulated Raman signal by substituting the relevant $\chi^{(3)}$ term into the wave equation and finding a plane wave solution. Substituting (1.21) in (1.12) yields:

$$
\frac{\partial^2 E_1(z,\omega)}{\partial z^2} + k_1^2\, E_1(z,\omega) = \frac{4\pi k_1^2}{n_1^2 c^2}\, D\,\chi^{(3)}_{SRL} E_1\, E_2 E_2^{*} \qquad (1.22)
$$

To further simplify this equation we use the slowly varying envelope approximation which means we assume that the electric field envelope

$\tilde{E}$, defined by: $E(z,\omega) = \tilde{E}(z,\omega) \exp[ikz]$, changes little over a distance on the order of a wavelength. Then we can neglect the second derivative of $\tilde{E}$ with respect to z,

$$\frac{\partial^2 E_1(z,\omega)}{\partial z^2} = \frac{\partial^2 \tilde{E}_1}{\partial z^2} + 2ik_1 \frac{\partial \tilde{E}_1}{\partial z} - k_1^2 \tilde{E}_1 \tag{1.23}$$

The wave equations then simplify to (the tilde is omitted):

$$\frac{\partial E_1}{\partial z} = \frac{i2\pi\omega_1}{n_1 c} D \quad \chi^{(3)}_{SRL} \, |E_2|^2 \, E_1 \tag{1.24}$$

$$\frac{\partial E_2}{\partial z} = \frac{i2\pi\omega_2}{n_2 c} D \quad \chi^{(3)}_{SRG} \, |E_1|^2 \, E_2 \tag{1.25}$$

If we assume weak coupling, which means that the pump wave intensity does not change appreciably as the wave propagates through the medium, then the two gain equations for the pump and the probe wave decouple and can be integrated separately.

$$E_1(z) = E_1(z=0) \exp\left\{ \frac{2\pi i\omega_1}{n_1 c} D \, \chi^{(3)}_{SRL} \, |E_2|^2 z \right\} \tag{1.26}$$

This expression shows that the imaginary part of $\chi^{(3)}$ is responsible for the growth of the probe wave. The real part of $\chi^{(3)}$ causes a change in the index of the material which is called the Kerr effect. We can convert electric field E to intensity I by using $I = \frac{nc}{8\pi} |E|^2$

$$E_1(z) = E_1(z=0) \exp\left\{ \frac{16\pi^2\omega_1}{n_1 n_2 c^2} D \, \mathrm{Im}(\chi^{(3)}_{SRL}) I_2 z \right\} \tag{1.27}$$

$$I_1(z) = I_1(z=0) \exp\left\{ \frac{32\pi^2\omega_1}{n_1 n_2 c^2} D \, \mathrm{Im}(\chi^{(3)}_{SRL}) I_2 z \right\} = I_1(z=0) \exp[lI_2 z] \tag{1.28}$$

$$I_2(z) = I_2(z=0)\ \exp\left\{\frac{32\pi^2\omega_2}{n_2 n_1 c^2}\ D\ \mathrm{Im}(\chi^{(3)}_{SRG}) I_1 z\right\} = I_2(z=0)\ \exp[g I_1 z] \qquad (1.29)$$

which defines the Raman gain and loss factors l and g:

$$l = \frac{32\pi^2\omega_1}{n_1 n_2 c^2}\ D\ \mathrm{Im}(\chi^{(3)}_{SRL}) \qquad g = \frac{32\pi^2\omega_2}{n_2 n_1 c^2}\ D\ \mathrm{Im}(\chi^{(3)}_{SRG}) \qquad (1.30)$$

We can linearize the exponential since the Raman loss or gain is very small in most spectroscopic experiments ($lz \ll 1$):

$$\delta I_1 = l\ z\ I_1 = \frac{32\pi^2\omega_1}{n_1 n_2 c^2}\ D\ \mathrm{Im}(\chi^{(3)}_{SRL})\ I_1\ I_2 \cdot z \qquad (1.31)$$

$$\delta I_2 = g\ z\ I_2 = \frac{32\pi^2\omega_2}{n_2 n_1 c^2}\ D\ \mathrm{Im}(\chi^{(3)}_{SRG})\ I_2\ I_1 \cdot z \qquad (1.32)$$

These equations give the SRS signal in terms of laser intensity (units: Watt per cm^2) and the interaction length z with the sample.

From an experimental point of view it is more useful to express the signal in terms of the total laser power P in the beams by integrating over the interaction volume. This can be done analytically by assuming a Gaussian intensity distribution I(r,z) for the laser beams in the experiment. For the change in the power of the probe one finds:

$$\delta P_2 = g\ P(\omega_2)\ P(\omega_1)\ \frac{2}{\lambda}\ \arctan(n) \qquad (1.33)$$

where n describes the sample length measured in units of confocal parameters B.[2] This result shows that the total signal is independent

---

[2] The confocal parameter B is defined as twice the distance from the focus where the beam diameter has increased by a factor of $\sqrt{2}$. The

of the focal length as long as the interaction region is filled with the sample and that 50% of the signal is generated within one confocal parameter B about the focus of the beams and 90% within 6 B.

In order to obtain spectroscopic information from nonlinear effects caused by the third order susceptibility $\chi^{(3)}$ one has to establish the connection between the macroscopic, bulk polarization and the microscopic, molecular properties of the material. The connection between $\chi^{(3)}$ and the conventional Raman cross section can be derived using a semi-classical oscillator model or by a quantum mechanical perturbation calculation. Because the oscillator model produces the important relations quickly and is perhaps more intuitive we will present it here briefly.

Microscopic Form of $\chi^{(3)}$

The Oscillator Model

In the oscillator model one calculates the Raman contribution to the nonlinear susceptibility from the equation of motion of the Raman active vibrations. The behavior of the expectation value $\langle q \rangle \equiv q_{av}$ is

---

spotsize d at the focus and B are related and can be calculated from

$$B = \frac{\pi d^2}{2\lambda} = 2\pi\left(\frac{f}{D}\right)^2 \lambda$$

where f is the focal length of the focusing lens, D the beam diameter on the lens and λ the wavelength of the light. The ratio f/D is called the f number $f^{\#}$ of the imaging and as a rule of thumb the spotsize of a Gaussian beam at the focus is $d = 2\, f^{\#} \lambda$ and the depth of focus, described by the confocal parameter B, is $B = 2\pi\, (f^{\#})^2\, \lambda$. The spot size d is defined as the beam diameter at the 1/e points of the intensity.

identical to that of a harmonic oscillator driven by an external force. The equation of motion in this case can be written as[28]:

$$\frac{\partial^2 q_{av}}{\partial t^2} + \Gamma \frac{\partial q_{av}}{\partial t} + \omega_0^2 q_{av} = \frac{1}{2m} \frac{\partial \alpha}{\partial q} E^2 \Delta \tag{1.34}$$

Here Δ is the population difference between the two oscillator levels, m is the reduced mass of the oscillator, and Γ is the damping constant which is related to the dephasing time: $\Gamma = 1/T_2$. The driving force interacts through the field-induced dipole moment $M = \frac{\partial \alpha}{\partial q} q_{av} E$. The derivative of the polarizability tensor with respect to the normal coordinate q, $\frac{\partial \alpha}{\partial q}$, is related to the Raman matrix element by[3]

$$\alpha^R_{lm} = \sqrt{\frac{\hbar}{2m\omega_0}} \left(\frac{\partial \alpha}{\partial q} \right)_{lm} \tag{1.35}$$

For a solution of eqn.(1.34) one assumes that the molecular vibration is driven by the two laser fields near resonance by writing:

$$q_{av} = \frac{1}{2} \{ q \exp[i(k_1 - k_2) - i(\omega_1 - \omega_2)t] + c.c. \} \tag{1.36}$$

The Raman contribution to the nonlinear polarization is given by:

$$\mathbb{P}^{nl} = N\, q_{av} \frac{\partial \alpha}{\partial q} E \tag{1.37}$$

where N is the molecular number density. Inserting the solution of the equation of motion for q_{av} gives[28]:

$$\mathbb{P}^{nl} = \frac{N\Delta}{8\omega\, m} \frac{1}{\omega_0 - (\omega_1 - \omega_2) + i\Gamma} \cdot \sum_{l,n,o} \left(\frac{\partial \alpha}{\partial q} \right)_{lm} \left(\frac{\partial \alpha}{\partial q} \right)^*_{no} E_{1m} E^*_{1n} E_{2o} \exp[ik_2 z] \tag{1.38}$$

If we compare (1.38) with (1.18) and use (1.35) for the Raman matrix

---

[3] When the local field correction is taken into account, a factor $(n^2+1)^2/9$ is included on the right hand side of (1.35)

element we get:

$$\chi^{(3)}(-\omega_2,\omega_1,-\omega_1,\omega_2) = \frac{N\Delta}{24\hbar}\,\frac{\alpha^R_{lm}\,(\alpha^R_{no})^*}{\omega_0-(\omega_1-\omega_2)+i\Gamma} \tag{1.39}$$

For liquids and gases the susceptibility is averaged over all orientations of the molecules. The relation between the Raman matrix element α^R_{xx} and the integrated spontaneous Raman cross section is:

$$<|\alpha^R_{xx}|^2> = \left(\frac{c}{\omega}\right)^4 \left(\frac{\partial\sigma}{\partial\Omega}\right) \tag{1.40}$$

with $\left(\frac{\partial\sigma}{\partial\Omega}\right)_{xx} = \frac{d\sigma}{d\Omega}\,\frac{1}{1+\rho}$ where ρ is the depolarization ratio. Using this one finds:

$$\chi^{(3)}_{1111} = \frac{N\Delta}{24\hbar}\left(\frac{c}{\omega}\right)^4 \left(\frac{\partial\sigma}{\partial\Omega}\right)_{xx} \frac{1}{\omega_0-(\omega_1-\omega_2)+i\Gamma} \tag{1.41}$$

As seen in (1.30) the SRS signal depends only on the imaginary part of $\chi^{(3)}$; it is therefore useful to separate (1.39) into its real and imaginary part.

$$\mathrm{Re}(\chi^{(3)}_{1111}) = \frac{N\Delta}{24\hbar}\left(\frac{c}{\omega}\right)^4 \left(\frac{\partial\sigma}{\partial\Omega}\right)_{xx} \frac{\omega_0-(\omega_1-\omega_2)}{\left(\omega_0-(\omega_1-\omega_2)\right)^2+\Gamma^2} + \chi_{NR} \tag{1.42}$$

$$\mathrm{Im}(\chi^{(3)}_{1111}) = \frac{N\Delta}{24\hbar}\left(\frac{c}{\omega}\right)^4 \left(\frac{\partial\sigma}{\partial\Omega}\right)_{xx} \frac{\Gamma}{\left(\omega_0-(\omega_1-\omega_2)\right)^2+\Gamma^2} \tag{1.43}$$

Included in eqn. 1.42 is χ_{NR}, the nonresonant part of the susceptibility that exists for all samples due to the electronic polarizability. χ_{NR} varies slowly with frequency and is usually orders of magnitudes smaller than the resonant part but it does limit the sensitivity of some nonlinear Raman techniques where the signal depends on both the real and the imaginary part of $\chi^{(3)}$. The SRS signal depends only on the imaginary part of $\chi^{(3)}$, which is one of the advantages of SRS especially in condensed phases where the contribution from χ_{NR} can be appreciable and lead to distortions in the lineshapes for CARS.

Eqn. 1.43 is the fundamental susceptibility equation that relates the SRS signal to the conventional Raman cross section. The lineshapes measured with SRS are identical to conventional Raman lineshapes which simplifies the analysis of lineshape measurements. One difference between SRS and conventional Raman spectra that should be pointed out is the fact that the SRS signal depends on the number density difference Δ, whereas in conventional Raman spectroscopy the Stokes signal is proportional to the ground state population and the anti-Stokes signal proportional to the population of the upper state. In vibrational Raman spectra this difference is negligible, especially at low temperatures, but in pure rotational Raman spectra it leads to significant changes in the intensity contours and limits the sensitivity of SRS in cases of very small shift.

Quantum Mechanical Derivation of $\chi^{(3)}$

Since the density matrix formalism is usually used for this purpose a short introduction will be given here:

If a wavefunction for some quantum mechanical system, in the Dirac notation , is given by

$$|\psi\rangle = \sum_n c_n(t)\ |\phi_n\rangle \qquad (1.44)$$

the density matrix for this system is defined as $\rho = |\psi\rangle\ \langle\psi|$ with its elements

$$\rho_{nm} = c_n c_m^* \tag{1.45}$$

The diagonal elements (n=m) describe the probabilities of finding the system in its various eigenstates. The off-diagonal elements (n≠m) represent the coherence intrinsic to a superposition of the states. The real advantage of the density matrix formalism is that it can correctly describe the observable properties of an ensemble of quantum mechanical systems.

For an ensemble the correct definition of the density matrix elements is

$$\rho = \sum_{\psi} P_{\psi} \, |\psi\rangle \, \langle\psi| \tag{1.46}$$

where P_{ψ} is the probability of finding the state ψ in the ensemble and the sum is over all possible states. The mean value for any observable A is given by $\langle A\rangle = \mathrm{Tr}\{\rho\cdot A\}$, so we can write for the electric dipole polarization

$$P(t) = N \,\langle\mu\rangle = N \,\mathrm{Tr}\{\rho(t)\cdot\mu\} \tag{1.47}$$

where μ is the dipole operator, N is the number density, and Tr{...} denotes the trace of a matrix.

The time evolution of the density matrix obeys the Liouville equation:

$$i\hbar \frac{\partial\rho}{\partial t} = \left[H_0 + H_{int},\ \rho \right] + i\hbar\, \Gamma_{random} \tag{1.48}$$

H_0 is the unperturbed Hamiltonian and $H_{int} = -\vec{\mu}\cdot\mathbb{E}$ is the dipole interaction of the molecule with the applied field. The random interactions in the ensemble are added by the phenomenological damping matrix $i\hbar\, \Gamma_{random}$. The diagonal elements Γ_{gg} represent population decay due to inelastic collisions (T_1 processes), while off-diagonal terms $\Gamma_{gt} = \Gamma_{tg} = \frac{1}{2}(\Gamma_{gg} + \Gamma_{tt}) + \Gamma^{e}_{gt}$ result from the broadening of the two states t and g plus a dephasing contribution, Γ^{e}_{tg}, caused by elastic collisions (T_2 processes).

Solving the Equation of Motion

An approximate solution to the equation of motion can be obtained by expressing $\rho(t)$ in the form of a perturbation series:

$$\rho(t) = \rho^{0}(t) + \lambda\, \rho^{(1)}(t) + \lambda^{2}\, \rho^{(2)}(t) + \lambda^{3}\, \rho^{(3)} + \ldots \tag{1.49}$$

Substituting this "Ansatz" in the equation of motion and equating equal powers in λ results in the following hierarchy of equations:

$$i\hbar \frac{\partial \rho^{(0)}}{\partial t} = \left[H_0 , \rho^{(0)} \right] + i\hbar\, \Gamma_r\, \rho^{(0)} \tag{1.50}$$

$$i\hbar \frac{\partial \rho^{(1)}}{\partial t} = \left[H_0 , \rho^{(1)} \right] + \left[H_{int} , \rho^{(0)} \right] + i\hbar\Gamma_r\, \rho^{(1)} \tag{1.51}$$

$$i\hbar \frac{\partial \rho^{(n)}}{\partial t} = \left[H_0 , \rho^{(n)} \right] + \left[H_{int} , \rho^{(n-1)} \right] + i\hbar\Gamma_r\, \rho^{(n)} \tag{1.52}$$

Successive solution of this system yields an expansion for the n-th order term of the density matrix $\rho^{(n)}$ which contains the applied electric field to the n th power. The result for the third order term $\rho^{(3)}$ is:

$$\rho^{(3)}_{gk}(\omega_a + \omega_b + \omega_c) = \frac{1}{\hbar^{3}\,(\omega_{gk} - \omega_a - \omega_b - \omega_c)} \; P_{abc} \sum_{jt}$$

$$\left\{ \frac{V^{c}_{gj}\, V^{b}_{jt}\, V^{a}_{tk}}{\omega_{jk} - \omega_a - \omega_b} \left[\frac{\rho^{0}_{tt} - \rho^{0}_{kk}}{\omega_{tk} - \omega_a} - \frac{\rho^{0}_{jj} - \rho^{0}_{tt}}{\omega_{jt} - \omega_b} \right] + \right.$$

$$+ \frac{V^a_{gt}\, V^b_{tj}\, V^c_{jk}}{\omega_{gj} - \omega_a - \omega_b} \left[\frac{\rho^0_{gg} - \rho^0_{tt}}{\omega_{gt} - \omega_a} - \frac{\rho^0_{tt} - \rho^0_{jj}}{\omega_{tj} - \omega_b} \right] \Bigg\} \qquad (1.53)$$

where P_{abc} denotes all permutations of $\omega_a\ \omega_b\ \omega_c$, $\omega_{jk} \equiv \frac{E_j - E_k}{\hbar} - i\,\Gamma_{jk}$

and $V^c_{gj} = \langle g| - \frac{1}{2}\, M\cdot E_c |j\rangle = -\frac{1}{2} \langle g|\, M\cdot e_c |j\rangle\, E_c = -\frac{1}{2}\, M^c_{gj}\, E_c$.

In order to clarify the definition of the various labels the following diagram for a general 4 wave mixing process is useful:

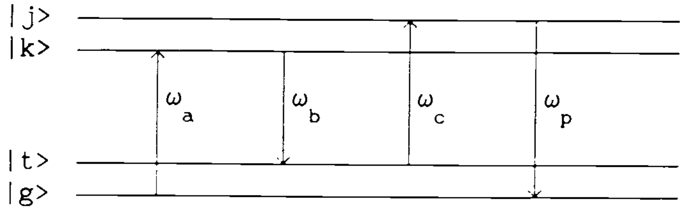

Here M^c_{gj} is the dipole transition matrix element between the molecular states |g> and |j>. The labels a,b,c,p characterize both frequency and polarization of the electric fields (p designates the signal polarization at $\omega_p = \omega_a - \omega_b + \omega_c$). The nonlinear susceptibility $\chi^{(n)}$ can then be related to the density matrix term of corresponding order n. $\chi^{(3)}$ for example is obtained from the expression for the third order polarization $P^{(3)}$:

$$P^{(3)}_p(\omega_p) = 2\,N \sum_{gk} \rho^{(3)}_{gk}\, M^p_{kg}$$

$$\overset{!}{\equiv} \frac{1}{4}\, \chi^{(3)}_{pabc}(-\omega_p, \omega_a, \omega_b, \omega_c) \cdot E_a\, E_b\, E_c \qquad (1.54)$$

With this we obtain the following expression for $\chi^{(3)}$:

$$\chi^{(3)}_{pabc}(\omega_p,\omega_a,\omega_b,\omega_c) = -N\hbar^{-3} \mathop{P}_{abc} \sum_{gkjt} \frac{1}{\omega_{gk}-\omega_p} \left\{ \frac{M^c_{gj}M^b_{jt}M^a_{tk}M^p_{kg}}{\omega_{jk}-\omega_a-\omega_b}\left[\frac{\rho^0_{tt}-\rho^0_{kk}}{\omega_{tk}-\omega_a} - \frac{\rho^0_{jj}-\rho^0_{tt}}{\omega_{jt}-\omega_b}\right] + \frac{M^a_{gt}M^b_{tj}M^c_{jk}M^p_{kg}}{\omega_{gj}-\omega_a-\omega_b}\left[\frac{\rho^0_{gg}-\rho^0_{tt}}{\omega_{gt}-\omega_a}-\frac{\rho^0_{tt}-\rho^0_{jj}}{\omega_{jt}-\omega_b}\right]\right\} \tag{1.55}$$

Rewriting this expression in a way that shows the resonant denominators explicitly is useful in determining which parts of $\chi^{(3)}$ contribute for a particular spectroscopic technique. All 48 terms that appear in equ. 1.56 are tabulated in table II.1.2.

$$\chi^{(3)}_{pabc}(\omega_p,\omega_a,\omega_b,\omega_c) = -N\hbar^{-3}\sum_{gkjt} M^p_{gk}M^a_{kt}M^b_{tj}M^c_{jg}\rho^0_{gg}\,(\text{sum of 48 terms}) \tag{1.56}$$

The summations runs over all molecular states (labeled by g, k, j, t) and the greek letters $\alpha, \beta, \gamma, \mu$ in table (II.1.2) give the order of the cartesian components of the dipole elements $M^{\alpha}_{gk}M^{\beta}_{kt}M^{\gamma}_{tj}M^{\mu}_{jg}$.

$$\frac{\gamma\beta\alpha\mu}{(\omega_{kg}+\omega_{c})(\omega_{tg}-(\omega_{b}-\omega_{c}))(\omega_{jg}-\omega_{p})} \qquad 1$$

$$\frac{\beta\gamma\alpha\mu}{(\omega_{kg}-\omega_{b})(\omega_{tg}-(\omega_{b}-\omega_{c}))(\omega_{jg}-\omega_{p})} \qquad 2$$

$$\frac{\gamma\alpha\beta\mu}{(\omega_{kg}+\omega_{c})(\omega_{tg}-(\omega_{a}-\omega_{c}))(\omega_{jg}-\omega_{p})} \qquad 3$$

$$\frac{\alpha\gamma\beta\mu}{(\omega_{kg}-\omega_{a})(\omega_{tg}-(\omega_{a}-\omega_{c}))(\omega_{jg}-\omega_{p})} \qquad 4$$

$$\frac{\beta\alpha\gamma\mu}{(\omega_{kg}-\omega_{b})(\omega_{tg}-(\omega_{a}+\omega_{b}))(\omega_{jg}-\omega_{p})} \qquad 5$$

$$\frac{\alpha\beta\gamma\mu}{(\omega_{kg}-\omega_{a})(\omega_{tg}-(\omega_{a}+\omega_{b}))(\omega_{jg}-\omega_{p})} \qquad 6$$

$$\frac{\mu\alpha\beta\gamma}{(\omega^{*}_{jg}-\omega_{c})(\omega^{*}_{tg}+(\omega_{b}-\omega_{c}))(\omega^{*}_{kg}+\omega_{p})} \qquad 7$$

$$\frac{\mu\alpha\gamma\beta}{(\omega^{*}_{jg}+\omega_{b})(\omega^{*}_{tg}-(\omega_{b}+\omega_{c}))(\omega^{*}_{kg}+\omega_{p})} \qquad 8$$

$$\frac{\mu\beta\alpha\gamma}{(\omega^{*}_{jg}-\omega_{c})(\omega^{*}_{tg}+(\omega_{b}-\omega_{c}))(\omega^{*}_{kg}+\omega_{p})} \qquad 9$$

$$\frac{\mu\beta\gamma\alpha}{(\omega^{*}_{jg}+\omega_{a})(\omega^{*}_{tg}+(\omega_{a}-\omega_{c}))(\omega^{*}_{kg}+\omega_{p})} \qquad 10$$

$$\frac{\mu\gamma\alpha\beta}{(\omega^{*}_{jg}+\omega_{b})(\omega^{*}_{tg}+(\omega_{a}+\omega_{b}))(\omega^{*}_{kg}+\omega_{p})} \qquad 11$$

$$\frac{\mu\gamma\beta\alpha}{(\omega^{*}_{jg}+\omega_{a})(\omega^{*}_{tg}+(\omega_{a}+\omega_{b}))(\omega^{*}_{kg}+\omega_{p})} \qquad 12$$

$$\frac{\gamma\beta\mu\alpha}{(\omega_{gj}-\omega_{a})(\omega_{kj}-(\omega_{a}-\omega_{c}))(\omega^{*}_{jt}+\omega_{p})} \qquad 13$$

$$\frac{\gamma\beta\mu\alpha}{(\omega_{kg}+\omega_{c})(\omega_{kj}-(\omega_{a}-\omega_{c}))(\omega^{*}_{jt}+\omega_{p})} \qquad 14$$

$$\frac{\gamma\beta\mu\alpha}{(\omega_{kg}+\omega_{c})(\omega_{tg}-(\omega_{b}-\omega_{c}))(\omega^{*}_{jt}+\omega_{p})} \qquad 15$$

$$\frac{\beta\gamma\mu\alpha}{(\omega_{gj}-\omega_{a})(\omega_{kj}-(\omega_{a}+\omega_{b}))(\omega^{*}_{jt}+\omega_{p})} \qquad 16$$

$$\frac{\beta\gamma\mu\alpha}{(\omega_{kg}-\omega_{b})(\omega_{kj}-(\omega_{a}+\omega_{b}))(\omega^{*}_{jt}+\omega_{p})} \qquad 17$$

$$\frac{\beta\gamma\mu\alpha}{(\omega_{kg}-\omega_{b})(\omega_{tg}-(\omega_{b}-\omega_{c}))(\omega^{*}_{jt}+\omega_{p})} \qquad 18$$

$$\frac{\gamma\alpha\mu\beta}{(\omega_{gj}-\omega_{b})(\omega_{kj}-(\omega_{b}-\omega_{c}))(\omega^{*}_{jt}+\omega_{p})} \qquad 19$$

$$\frac{\gamma\alpha\mu\beta}{(\omega_{kg}+\omega_{c})(\omega_{kj}-(\omega_{b}-\omega_{c}))(\omega^{*}_{jt}+\omega_{p})} \qquad 20$$

$$\frac{\gamma\alpha\mu\beta}{(\omega_{kg}+\omega_{c})(\omega_{tg}-(\omega_{a}-\omega_{c}))(\omega^{*}_{jt}+\omega_{p})} \qquad 21$$

$$\frac{\gamma\beta\alpha\mu}{(\omega_{gj}-\omega_{b})(\omega_{kj}-(\omega_{a}+\omega_{b}))(\omega^{*}_{jt}+\omega_{p})} \qquad 22$$

$$\frac{\alpha\gamma\mu\beta}{(\omega_{kg}-\omega_{a})(\omega_{kj}-(\omega_{a}+\omega_{b}))(\omega^{*}_{jt}+\omega_{p})} \qquad 23$$

$$\frac{\alpha\gamma\mu\beta}{(\omega_{kg}-\omega_{a})(\omega_{tg}-(\omega_{a}-\omega_{c}))(\omega^{*}_{jt}+\omega_{p})} \qquad 24$$

Table II.1.2a: Terms 1-24 in the full expression for $\chi^{(3)}$.

$$\frac{\beta\alpha\mu\gamma}{(\omega_{gj} + \omega_{c})(\omega_{kj} - (\omega_{b} - \omega_{c}))(\omega^{*}_{jt} + \omega_{p})} \qquad 25$$

$$\frac{\beta\alpha\mu\gamma}{(\omega_{kg} - \omega_{b})(\omega_{kj} - (\omega_{b} - \omega_{c}))(\omega^{*}_{jt} + \omega_{p})} \qquad 26$$

$$\frac{\beta\alpha\mu\gamma}{(\omega_{kg} - \omega_{b})(\omega_{tg} - (\omega_{a} + \omega_{b}))(\omega^{*}_{jt} + \omega_{p})} \qquad 27$$

$$\frac{\alpha\beta\mu\gamma}{(\omega_{gj} + \omega_{c})(\omega_{kj} - (\omega_{a} - \omega_{c}))(\omega^{*}_{jt} + \omega_{p})} \qquad 28$$

$$\frac{\alpha\beta\mu\gamma}{(\omega_{kg} - \omega_{a})(\omega_{kj} - (\omega_{a} - \omega_{c}))(\omega^{*}_{jt} + \omega_{p})} \qquad 29$$

$$\frac{\alpha\beta\mu\gamma}{(\omega_{kg} - \omega_{a})(\omega_{tg} - (\omega_{a} + \omega_{b}))(\omega^{*}_{jt} + \omega_{p})} \qquad 30$$

$$\frac{\alpha\mu\beta\gamma}{(\omega_{gj} + \omega_{c})(\omega_{kj} - (\omega_{a} - \omega_{c}))(\omega_{kt} - \omega_{p})} \qquad 31$$

$$\frac{\alpha\mu\beta\gamma}{(\omega_{kg} - \omega_{a})(\omega_{kj} - (\omega_{a} - \omega_{c}))(\omega_{kt} - \omega_{p})} \qquad 32$$

$$\frac{\alpha\mu\beta\gamma}{(\omega^{*}_{jg} - \omega_{c})(\omega^{*}_{tg} - (\omega_{b} - \omega_{c}))(\omega_{kt} - \omega_{p})} \qquad 33$$

$$\frac{\alpha\mu\gamma\beta}{(\omega_{gj} - \omega_{b})(\omega_{kj} - (\omega_{a} + \omega_{b}))(\omega_{kt} - \omega_{p})} \qquad 34$$

$$\frac{\alpha\mu\gamma\beta}{(\omega_{kg} - \omega_{a})(\omega_{kj} - (\omega_{a} + \omega_{b}))(\omega_{kt} - \omega_{p})} \qquad 35$$

$$\frac{\alpha\mu\gamma\beta}{(\omega^{*}_{jg} + \omega_{b})(\omega^{*}_{tg} + (\omega_{b} - \omega_{c}))(\omega_{kt} - \omega_{p})} \qquad 36$$

$$\frac{\beta\mu\alpha\gamma}{(\omega_{gj} + \omega_{c})(\omega_{kj} - (\omega_{b} - \omega_{c}))(\omega_{kt} - \omega_{p})} \qquad 37$$

$$\frac{\beta\mu\alpha\gamma}{(\omega_{kg} - \omega_{b})(\omega_{kj} - (\omega_{b} - \omega_{c}))(\omega_{kt} - \omega_{p})} \qquad 38$$

$$\frac{\beta\mu\alpha\gamma}{(\omega^{*}_{jg} - \omega_{c})(\omega^{*}_{tg} + (\omega_{a} - \omega_{c}))(\omega_{kt} - \omega_{p})} \qquad 39$$

$$\frac{\beta\mu\gamma\alpha}{(\omega_{gj} - \omega_{a})(\omega_{kj} - (\omega_{a} + \omega_{b}))(\omega_{kt} - \omega_{p})} \qquad 40$$

$$\frac{\beta\mu\gamma\alpha}{(\omega_{kg} - \omega_{b})(\omega_{kj} - (\omega_{a} + \omega_{b}))(\omega_{kt} - \omega_{p})} \qquad 41$$

$$\frac{\beta\mu\gamma\alpha}{(\omega^{*}_{jg} + \omega_{a})(\omega^{*}_{tg} + (\omega_{a} - \omega_{c}))(\omega_{kt} - \omega_{p})} \qquad 42$$

$$\frac{\gamma\mu\alpha\beta}{(\omega_{gj} - \omega_{b})(\omega_{kj} - (\omega_{b} - \omega_{c}))(\omega_{kt} - \omega_{p})} \qquad 43$$

$$\frac{\gamma\mu\alpha\beta}{(\omega_{kg} + \omega_{c})(\omega_{kj} - (\omega_{b} - \omega_{c}))(\omega_{kt} - \omega_{p})} \qquad 44$$

$$\frac{\gamma\mu\alpha\beta}{(\omega^{*}_{jg} + \omega_{b})(\omega^{*}_{tg} + (\omega_{a} + \omega_{b}))(\omega_{kt} - \omega_{p})} \qquad 45$$

$$\frac{\gamma\mu\beta\alpha}{(\omega_{gj} - \omega_{a})(\omega_{kj} - (\omega_{a} - \omega_{c}))(\omega_{kt} - \omega_{p})} \qquad 46$$

$$\frac{\gamma\mu\beta\alpha}{(\omega_{kg} + \omega_{c})(\omega_{kj} - (\omega_{a} - \omega_{c}))(\omega_{kt} - \omega_{p})} \qquad 47$$

$$\frac{\gamma\mu\beta\alpha}{(\omega^{*}_{jg} + \omega_{a})(\omega^{*}_{tg} + (\omega_{a} + \omega_{b}))(\omega_{kt} - \omega_{p})} \qquad 48$$

Table II.1.2b: Terms 25-48 in the full expression for $\chi^{(3)}$.

The Stimulated Raman Susceptibilities $\chi^{(3)}_{SRL}$ and $\chi^{(3)}_{SRG}$

In the Raman loss case we have $\omega_a = \omega_p = \omega_1$ and $\omega_b = \omega_c = \omega_2$. Looking for resonances that take molecules from the ground state to the excited vibrational state (i.e. setting g=i= initial and t=f=final) we select all terms that contain the factor $\omega_{tg} - (\omega_a - \omega_c)$ in the denominator (terms 3,4,21,24). These can be added up to give a ρ^0_{ii} contribution:

$$\frac{\rho^0_{ii}}{\omega_{fi} - \omega_1 + \omega_2} \sum_k \left(\frac{R^\gamma_{ik} R^\alpha_{kf}}{\omega_{ki} + \omega_2} + \frac{R^\alpha_{ik} R^\gamma_{kf}}{\omega_{ki} - \omega_1} \right) \sum_j \left(\frac{R^\beta_{fj} R^\mu_{ji}}{\omega_{ji} - \omega_1} + \frac{R^\mu_{fj} R^\beta_{ji}}{\omega^*_{jf} + \omega_1} \right) \tag{1.57}$$

At the same time the reverse process takes molecules from the upper vibrational state to the ground state. Setting g=f and t=i we look for denominators that contain $\omega^*_{tg} + (\omega_a - \omega_c)$. Terms 9,10,39 and 42 add up to the ρ^0_{ff} contribution:

$$\frac{-\rho^0_{ff}}{\omega_{fi} - \omega_1 + \omega_2} \sum_k \left(\frac{R^\gamma_{ik} R^\alpha_{kf}}{\omega^*_{kf} + \omega_2} + \frac{R^\alpha_{ik} R^\gamma_{kf}}{\omega^*_{kf} - \omega_1} \right) \sum_j \left(\frac{R^\beta_{fj} R^\mu_{ji}}{\omega_{ji} - \omega_1} + \frac{R^\mu_{fj} R^\beta_{ji}}{\omega^*_{jf} + \omega_1} \right) \tag{1.58}$$

Adding these and summing over all resonant pairs of levels i,f gives

$$\chi^{(3)}_{SRL} = 6\,\chi^{(3)}(-\omega_1, -\omega_2, \omega_1, \omega_2)$$

$$= \sum_{i,f} \frac{N}{4\hbar^3(\omega_{fi} - \omega_1 + \omega_2)} \sum_j \left(\frac{R^\beta_{fj} R^\mu_{ji}}{\omega_{ji} - \omega_1} + \frac{R^\mu_{fj} R^\beta_{ji}}{\omega^*_{jf} + \omega_1} \right)$$

$$\times \sum_k \left[\rho^0_{ii} \left(\frac{R^\gamma_{ik} R^\alpha_{kf}}{\omega_{ki} + \omega_2} + \frac{R^\alpha_{ik} R^\gamma_{kf}}{\omega_{ki} - \omega_1} \right) - \rho^0_{ff} \left(\frac{R^\gamma_{ik} R^\alpha_{kf}}{\omega^*_{kf} + \omega_1} + \frac{R^\alpha_{ik} R^\gamma_{kf}}{\omega^*_{kf} - \omega_2} \right) \right] \tag{1.59}$$

The corresponding relation for SRG is obtained from terms 9,10,39 and 42 for state i and 3,4,21 and 24 for state f, yielding,

$$\chi^{(3)}_{SRG} = 6\,\chi^{(3)}(-\omega_2,-\omega_1,\omega_1,\omega_2)$$

$$= \sum_{i,j} \frac{N}{4\hbar^3(\omega^*_{fi}-\omega_1+\omega_2)} \sum_j \left(\frac{R^\beta_{ij}R^\mu_{jf}}{\omega_{jf}-\omega_2} + \frac{R^\mu_{ij}R^\beta_{jf}}{\omega^*_{ji}+\omega_2}\right)$$

$$\times \sum_k \left[\rho^0_{ii}\left(\frac{R^\gamma_{fk}R^\alpha_{ki}}{\omega^*_{ki}+\omega_2} + \frac{R^\alpha_{fk}R^\gamma_{ki}}{\omega^*_{ki}-\omega_1}\right) - \rho^0_{ff}\left(\frac{R^\gamma_{fk}R^\alpha_{ki}}{\omega^*_{kf}+\omega_1}+\frac{R^\alpha_{fk}R^\gamma_{ki}}{\omega^*_{kf}-\omega_2}\right)\right] \qquad (1.60)$$

When the Raman resonance condition is met, $\omega_{fi} = \omega_1 - \omega_2 \cong \omega_{ji} - \omega_{jf}$, the two bracketed terms in (1.57) and (1.58) are equal and one sees that the Raman susceptibility is proportional to the difference in population densities $N(\rho^0_{ii}-\rho^0_{ff}) = N_i - N_f$. If the frequencies ω_1, ω_2, ω_3 are far from any electronic resonances in the sample each of the sums in parentheses is essentially identical and equal to a Raman polarizability element of the type:

$$\alpha_{\beta\mu} = \frac{1}{\hbar}\sum_j \left(\frac{R^\beta_{fj}R^\mu_{ji}}{\omega_{ji}-\omega_1} + \frac{R^\mu_{ij}R^\beta_{jf}}{\omega^*_{ji}+\omega_2}\right) \qquad (1.61)$$

The Raman polarizability element $\alpha_{\beta\mu}$ can be written in terms of the spontaneous Raman cross section $\frac{\partial\sigma}{\partial\Omega}$:

$$|\alpha_{\beta\mu}|^2 = \left(\frac{c}{\omega}\right)^4 \left(\frac{\partial\sigma}{\partial\Omega}\right)_{\beta\mu} \qquad (1.62)$$

If we take, for simplicity, the case where pump and probe beams are polarized in the same direction we can write the relationship between $\chi^{(3)}_{SRL}$, $\chi^{(3)}_{SRG}$ and the spontaneous Raman cross section:

$$\chi^{(3)}_{SRL} = \chi_{nr} + \sum_{if} \frac{1}{4\hbar}\left(\frac{c}{\omega}\right)^4 \frac{N_i - N_f}{\omega_0 - (\omega_1-\omega_2) - i\Gamma_{fi}} \left(\frac{\partial\sigma}{\partial\Omega}\right)_{fi} \qquad (1.63)$$

$$\chi^{(3)}_{SRG} = \chi_{nr} + \sum_{if} \frac{1}{4\hbar} \left(\frac{c}{\omega}\right)^{4} \frac{N_i - N_f}{\omega_0 - (\omega_1 - \omega_2) + i\Gamma_{fi}} \left(\frac{\partial\sigma}{\partial\Omega}\right)_{fi} \tag{1.64}$$

In the absence of one photon resonances the nonresonant electronic susceptibility χ_{nr} and the Raman cross section $\left(\frac{\partial\sigma}{\partial\Omega}\right)$ are real quantities. Since the stimulated Raman signal depends only on the imaginary part of $\chi^{(3)}$ we can rewrite the expression for the SRS signal in the final form which is useful for predicting the Raman signal for a particular sample and experimental conditions:

$$\delta P_1 = \frac{24c}{n_1 n_2 \hbar\, \omega_1^2} P_1 P_2 \Delta N \left(\frac{\partial\sigma}{\partial\Omega}\right) \frac{-\Gamma}{\left(\omega_0 - (\omega_1 - \omega_2)\right)^2 + \Gamma^2} \tag{1.65}$$

$$\delta P_2 = \frac{24c}{n_1 n_2 \hbar\, \omega_2^2} P_1 P_2 \Delta N \left(\frac{\partial\sigma}{\partial\Omega}\right) \frac{\Gamma}{\left(\omega_0 - (\omega_1 - \omega_2)\right)^2 + \Gamma^2} \tag{1.66}$$

2. RAMAN LINESHAPES

As a true high resolution technique SRS is not only capable of resolving closely spaced lines but also gives the true Raman lineshape of the transitions in many cases. Unlike in conventional Raman spectroscopy, where the observed lineshape is almost always determined by the slit function of the monochromator, the true Raman lineshape observed with SRS contains spectroscopic information on the sample. In the gas phase Doppler broadening is related to the sample temperature and flow velocity. Pressure broadening coefficients can be related to intermolecular interactions. In condensed phases the lineshape is determined by vibrational relaxation processes which also reveal intermolecular forces and the dynamics in the condensed phases. In order to understand the observed lineshapes and to separate experimental effects from broadening effects characteristic of the sample a review of the various broadening mechanisms is given in the following section.

Vibrational Relaxation

The general theory of vibrational relaxation treats the model of an ensemble of oscillators in contact with a "bath"[29]. In this theory the vibrational Raman lineshape is the Fourier transform of the time correlation function (TCF) of the vibrational coordinate <Q(0)Q(t)>:

$$I(\omega) = \int_{-\infty}^{+\infty} \langle Q(0)Q(t)\rangle \exp[-iwt]\, dt \qquad (2.1)$$

$$\text{with } \langle Q(t)Q(0)\rangle = \langle Q^2(0)\rangle \exp[i\omega t]\, C(t) \qquad (2.2)$$

The decay of the correlation function C(t) is caused by the modulation $\delta\omega(t)$ of the vibrational frequency around its average value ω. ω is actually shifted compared to the frequency ω_0 of the isolated oscillator due to the interactions with the bath.

$$\omega = \omega_0 + \langle\omega\rangle \tag{2.3}$$

$$\delta\omega(t) = \frac{1}{\hbar}(V_{11}(t) - V_{00}(t)) - \langle w\rangle \tag{2.4}$$

The correlation function C(t) is then given by:

$$C(t) = \langle \exp[\ i\int \delta\omega(t)\ dt]\ \rangle \tag{2.5}$$

In the evaluation of this expression one can distinguish between two limiting cases. In the *fast modulation limit* the product of the correlation time τ_c and the rms frequency fluctuations $\sqrt{\langle(\delta\omega(t))^2\rangle}$ is very small: $\tau_c \sqrt{\langle(\delta\omega(t))^2\rangle} \ll 1$

where τ_c is defined as $\tau_c = \int dt\langle\delta\omega(t)\delta\omega(0)\rangle/\langle(\delta\omega)^2\rangle$

A culmulant expansion[30] up to second order gives an exponential decay of C(t) with a rate of

$$(T_2)^{-1} = \int dt\ \langle\delta\omega(t)\delta\omega(0)\rangle \tag{2.6}$$

The Raman lineshape in the fast modulation limit is a Lorentzian profile with a FWHM given in wavenumbers by: $\Delta\tilde{\nu} = \dfrac{1}{\pi c T_2}$

If $\tau_c \sqrt{\langle(\delta\omega(t))^2\rangle} \cong 1$ higher order terms in the expansion of (2.5) must be included and C(t) does not follow a simple exponential decay. In the extreme case of a static distribution of oscillator frequencies ($\tau_c = \infty$) C(t) can be calculated as:

$$C(t) = \exp[\ -\frac{t}{T_2} - \frac{1}{2}\ t^2\sigma^2] \tag{2.7}$$

where σ is the width of the Gaussian frequency distribution.

In the limit of *slow modulation* the lineshape is a Voigt profile.

To describe the lineshape in a particular phase one has to specify what is meant by *oscillator* and *bath* in each case. In the gas phase relaxation is due to isolated binary collisions between the vibrating molecule and any other molecule. The bath states are the energy levels (translational, rotational, and vibrational) of all the other molecule. In the liquid the vibration is still largely localized on a single molecule but correlations between the molecules start to become important. Translational and rotational motion are diffusive and are treated classically for the bath degrees of freedom. In the solid state, finally, long range order exists which leads to collective excitations such as vibron, phonons and librons which are treated as quasi-particles. In this respect the solid is more like a gas again where relaxation occurs due to collisions with other quasi-particles which requires a fully quantum mechanical treatment.

Before the lineshapes are discussed separately for the different phases in more detail it is convenient at this point to recall the common convention for the relaxation times T_1, T_2 and τ which has its origin in the Bloch equations for magnetic dipole transitions. The total decay of the coherent vibrational amplitude, i.e. the time correlation function $\langle Q(0)Q(t)\rangle$ is characterized by the decay time T_2. Two contributions contribute to the decay. Energy relaxation due to transitions from the excited vibrational level to the ground state is described by a lifetime T_1. Dephasing (pure dephasing time T_2') describes the decay of the vibrational amplitude due to loss of coherence between the oscillators in the ensemble. The linewidth $\Delta\omega$ is then given by:

$$\frac{\Delta\omega}{2} = \frac{1}{T_2} = \frac{1}{T'_2} + \frac{1}{2T_1} \qquad (2.8)$$

The factor of 2 in the T_1 part stems from the fact that T_1 is an energy relaxation time. If one uses it in an expression that describes the decay of a vibrational amplitude one has to use $2T_1$ since the energy of an oscillator is proportional to the square of the amplitude.

Sometimes one distinguishes between a homogeneous dephasing time τ_{hom} which characterizes coherence loss due to fluctuations in the frequency of each oscillator and a inhomogeneous dephasing time τ_{inh} which describes coherence loss due to constant differences in the frequencies of different oscillators.

Gas Phase Lineshapes

Molecular motion plays an important role for the Raman lineshapes of gas phase samples. Generally the effects due to the intermolecular interactions and the molecular motion cannot be treated separately but for the sake of simplicity we will discuss the various contributions individually and refer to the literature for more advanced theories of gas phase Raman lineshapes[31].

Doppler broadening

At very low density where collisions are absent or rare the Raman lineshape is determined by Doppler broadening. One way to understand Doppler broadening[32] is to look at the recoil that the molecule experiences when it absorbs, emits, or inelastically scatters a photon. Since momentum has to be conserved in such a process, part of the photon energy $\hbar\omega$ is transferred to the kinetic energy of the molecule and will not be available to induce a transition between molecular energy levels. For that reason the molecule "sees" a frequency that is shifted by $\delta\omega = \vec{k}\cdot\vec{v}$ where $\vec{v}$ is the molecular velocity and $\vec{k}$ is the wavevector of the light. In a gas at thermal equilibrium the molecular velocities are characterized by the Maxwell-Boltzmann distribution with a rms velocity $\bar{v}$:

$$\bar{v} = (\ <v^2>\ )^{1/2} = \sqrt{\frac{2kT}{m}} \qquad (2.9)$$

The resulting line profile for a molecular resonance in gas is the familiar Doppler profile $G(\Delta)$ with a width Γ' proportional to the frequency and $\bar{v}$.

$$G(\Delta) = \frac{\sqrt{\pi}}{\Gamma'} \exp\left[\frac{-\Delta^2}{\Gamma'^2}\right] \tag{2.10}$$

$$\Gamma'_{FWHM} = 2\sqrt{\ln 2}\ \Gamma' = 2\nu_L \sqrt{\frac{2\ln 2\ kT}{mc^2}} \tag{2.11}$$

where Δ is the detuning from the resonance and ν_L is the frequency of the lightwave in wavenumbers.

In inelastic scattering, where there are two waves involved (incident and scattered), the Doppler shift depends on the net momentum transfer to the molecule which is given by the vector product:

$$\delta\omega = (\vec{k}_{in} - \vec{k}_{sc})\cdot\vec{v}_{mol} \tag{2.12}$$

One can see that both the frequency difference and the relative propagation direction of the two waves will influence the Doppler width. For co-propagating waves the Doppler width reduces to a minimum and is proportional to the Raman shift $|\omega_{in} - \omega_{sc}|$. It is one of the advantages of the stimulated Raman techniques that they exploit forward scattering geometry, whereas spontaneous Raman scattering usually has to be observed at 90° in order to discriminate against the incident light. The Doppler width in the general case is given by:

$$\Gamma'_{FWHM} = |\vec{k}_{in} - \vec{k}_{sc}| \sqrt{\frac{8\ln 2\ kT}{mc^2}} \tag{2.13}$$

A useful expression for estimating the Doppler width for a particular experiment is given by eqn. 2.14 were ν_{in} is the incident laser frequency in wavenumbers, ν_R the Raman shift, and γ the angle between the direction of the incident light and the direction in which the scattered light is observed. In a SRS experiment γ corresponds to the crossing angle between pump and probe beam.

$$\Gamma'[\mathrm{cm}^{-1}] = \left(4(\nu_{in}^2 + \nu_{in}\nu_R)\sin\frac{\gamma}{2} + \nu_R^2\right)^{\frac{1}{2}} \cdot 7.162\cdot10^{-7}\sqrt{\frac{T[\mathrm{K}]}{M[\mathrm{amu}]}} \qquad (2.14)$$

with T in Kelvin and M in amu. The lines in the vibrational Raman spectrum of nitrogen have a Doppler width of about 0.009 cm^{-1} or 170 MHz at 300 K. Comparing this to the collisional broadening coefficient of about 2 MHz/Torr[33] one finds that the Doppler effect starts to dominate the vibrational linewidth of N_2 for pressures below about 100 Torr. For rotational Raman lines the Doppler effect is much smaller in almost all cases, except for H_2, and collisional broadening dominates the linewidth to pressures below 1 Torr.

Collisional Broadening

Collisional broadening occurs, in the simplest case, because the lifetime of a coherent vibrational or rotational state becomes limited by elastic or inelastic collisions. Elastic collisions perturb the phase of the vibration (= dephasing characterized by the dephasing time T_2'), whereas inelastic collisions remove molecules from their particular energy level (population change characterized by lifetime T_1). In both cases the resulting lineshape is a Lorentzian profile with a FWHM which is inversely proportional to the overall lifetime T_2

as given by eqn. 2.8. The lineshape function for the pure Lorentzian is:

$$L(\Delta) = \frac{1}{\pi} \frac{\Gamma}{(\Delta^2 + \Gamma^2)} \tag{2.15}$$

with FWHM of $2\Gamma = (\pi c T_2)^{-1}$ in wavenumbers.

In a gas phase Raman spectrum there are usually both Gaussian and Lorentzian contributions whose relative weight depends on pressure and temperature. The resulting lineshape is described by a Voigt profile[33], which is a convolution of Lorentzian lines with central frequencies having a Gaussian distribution.

$$V(\Delta) = \frac{\pi}{2\Gamma'} [\; w(z) - w^*(z) \;] \tag{2.16}$$

with $z = (\Delta + i\Gamma)/\Gamma'$, Γ and Γ' are the Lorentzian and Gaussian linewidth contributions respectively, and w is the complex error function:

$$w(z) = \frac{i}{\pi} \int_{-\infty}^{+\infty} dt \; \frac{e^{-t^2}}{z-t} \tag{2.17}$$

Dicke Narrowing

For light molecules such as H_2 and D_2 the spacing between rotational energy levels is large, hence rotational relaxation through collisions becomes ineffective compared with that in heavier molecules. When only a small fraction of the collisions are rotationally inelastic and most collisions only affect the translational motion of the molecules the so-called Dicke[34] narrowing becomes observable. The physical origin for Dicke narrowing can be explained from a simple qualitative uncertainty principle argument.

Since the Doppler shift of a transition provides information on the velocity of a molecule and the uncertainty principle states that position and momentum of a molecule can only be determined simultaneously with minimum uncertainties given by $\Delta x \cdot \Delta p > \hbar$ one can not know the precise velocity at a given position. Only the average velocity for a certain displacement Δx is determined from the Doppler shift. Δx can be estimated from the uncertainty principle if we assume that the uncertainty in the momentum is equal to the momentum of the absorbed photon $\lambda/2\pi$: $\Delta x = \frac{h}{\lambda}$. If collisions are rare the velocity of the molecule will be constant during the time required to travel Δx. The spectral profile will then be the unperturbed Gaussian Doppler profile. If, on the other hand, there are many collisions while the molecule travels Δx the average velocity during this time will be close to zero and the linewidth will also go to zero in the absence of other broadening mechanisms. In the intermediate case there is a reduction in the Doppler broadening due to velocity averaging, so that the actual profile is somewhat narrower than the one calculated by neglecting velocity changing collisions.

The Galatry[35] line profile includes the effect of velocity changing collisions on the Doppler profile as well as collisional broadening due to phase perturbing and inelastic collisions and gives a more accurate representation of the Raman lineshapes than the simpler Voigt profile under conditions where Dicke narrowing is significant:

$$G(x,y,z) = \sqrt{\frac{1}{\pi}}\ \mathrm{Re}\left[\int dt\ \exp\left[\,-ixt-yt+\frac{1}{2z^2}\,(1-zt-\exp(-zt))\right]\right] \qquad (2.18)$$

In this expression the quantities x, y, and z, which are made dimensionless by dividing by the Doppler width Γ', are defined as:

$x = \frac{\Delta}{\Gamma'}$; Δ = dimensionless detuning from unperturbed frequency

$y = \frac{\Gamma}{\Gamma'}$; Γ = effective frequency of broadening collisions

$z = \frac{\beta}{\Gamma'}$; β = effective frequency of velocity changing collisions

The Galatry profile is based on a soft collision model in which the effects of individual collisions are assumed to negligible and only the cumulative action of many collisions results in a random velocity distribution. The molecular motion may then be modeled mathematically by the theory of Brownian motion. No correlation between velocity changing and state perturbing collisions is assumed. More elaborate models which take into account the details of the intermolecular interactions and of the collision process have also been developed[37].

Millot[37] et. al. have investigated the Q-branch spectrum of nitrogen with high resolution SRS for pressures from 100 to 1500 torr and found that a Galatry profile gives a very good fit for the observed line shape. They also showed that neglecting Dicke narrowing and using a Voigt line profile for nitrogen at 1 atm results in a 10% error in the collisional broadening coefficient.

Collisional Narrowing

Collisional or motional narrowing occurs for systems which consist of many closely spaced lines in the collision free limit, such as the rotational components of a vibrational Q-branch transition. This effect was first pointed out by Anderson[38] for magnetic resonance spectroscopy where it is referred to as exchange narrowing. The common physical model is a system that jumps randomly within a set of accessible energy levels. For a Raman Q-branch in gases and liquids these jumps are caused by rotationally inelastic collisions which lead to changes in the rotational quantum number J without changing the vibrational quantum number. If there is vibrational rotational coupling in the system (described by the coupling constant α) these changes in the J values cause small changes in the vibrational frequency which in turn will lead to vibrational dephasing and manifest itself in line broadening. If the system jumps very slowly between different states the spectrum reflects the distribution of accessible energy levels which is seen in a contour of a vibrational Q-branch at low gas pressure. The narrowing occurs in this model if the frequency of this level jumping, i.e the frequency of rotationally inelastic collisions ω_{col}, exceeds the mean frequency separation between the accessible levels. In this limit the linewidth is no longer given by the width of frequency distribution for the different J-levels $<\delta\omega>$ but is inversely proportional to ω_{col}:

$$\Delta\omega \cong \frac{< \delta\omega^2 >}{\omega_{col}} \tag{2.19}$$

For nitrogen as an example the spacing between the J= 7 and J= 9 components is about .7 cm^{-1} = 2.1 × 10^{10} Hz. Using the collision parameter σ = 3.7Å the frequency for rotationally inelastic collisions is approximately:

$$\omega_{col} = \frac{1}{5}\, \pi\sigma^2 \left(\frac{3kT}{m}\right)^{\frac{1}{2}} \rho L = 1.3 \times 10^9 \rho \tag{2.20}$$

where L is Loschmidt's number and ρ is the density in amagats. This predicts that for densities larger then 16 amagats (17.6 atm at 300K) the motional narrowing becomes dominant and causes the width of the vibrational band to decrease with increasing density.

Vibrational Raman Lineshapes in Liquids

Intramolecular vibrations in the liquid phase are usually treated classically by assuming a localized vibration of an anharmonic oscillator interacting with a bath. For a detailed account on the theory of vibrational relaxation in liquids see for example the review article by Oxtoby[29]. In general, the vibrational Raman lineshape in molecular liquids depends on energy relaxation and phase relaxation processes in the liquid. Vibrational energy relaxation (T_1 processes) can be important for polyatomic with several normal modes but in simple molecular liquids such as N_2 and O_2 the T_1 contribution to the linewidth is insignificant. The phase relaxation processes can be subdivided into three main categories:

(1) pure dephasing (direct perturbation of the vibrational motion through the intermolecular forces)

(2) intramolecular vibration-rotation coupling (changes in the vibrational frequency due to changes in the rotational quantum number J).

(3) resonant transfer of vibrational energy between molecules

In most simple liquids the fast modulation limit applies to the dephasing mechanisms (1)-(3)[39], which is reflected by the observed Lorentzian lineshapes. Studies of linewidth and shift as a function of temperature[40] and density[17] as well as experiments in which the diatomic liquid was diluted with a monoatomic solvent such as argon[41] make it possible to separate the contributions from the mechanisms (1)-(3). For liquid nitrogen it was found that at 78 K about 2/3 of the linewidth are due to pure dephasing and the remaining 1/3 are caused by vibration rotation coupling[42]. Resonant transfer has been shown to be unimportant in liquid N_2[43].

Raman Lineshapes in Crystals

The translational invariance of the crystalline state leads to a description in which the crystal is made up of identical unit cells repeated through space. Due to the intermolecular coupling, the modes of vibration in the lattice are collective, with each internal vibrational state of the molecule forming a band of elementary excitations called *vibrons*. The vibrons are treated as Bloch states, which are characterized by a wave vector $\vec{k}$. The vibrational modes are shifted with respect to the dilute gas phase and split into a number of components depending on the number of molecules Z per unit cell and on the space group symmetry. These shifts and splittings are generally of the order of a few cm^{-1} indicating the separation of energy scales of the intermolecular and intramolecular interactions. This separation is also reflected in the much lower frequencies of the phonons and librons, which are the delocalized translational and librational excitations in the crystal lattice. The harmonic theory of lattice dynamics which calculates the frequencies and splittings of vibron states in the molecular solids is well developed and has been treated extensively for example by Decius and Hexter[44] or Califano[45] .

Harmonic theory serves as a basis for the quantum mechanical treatment of vibrational relaxation in molecular crystals[46]. In this theory the vibrons and phonons are treated as particle-like excitations which can interact through cubic and quartic terms of the coupling Hamiltonian, given as an expansion in the crystal normal coordinates. The energy and phase relaxation processes caused by these interactions are graphically represented in Fig. II.2.1:

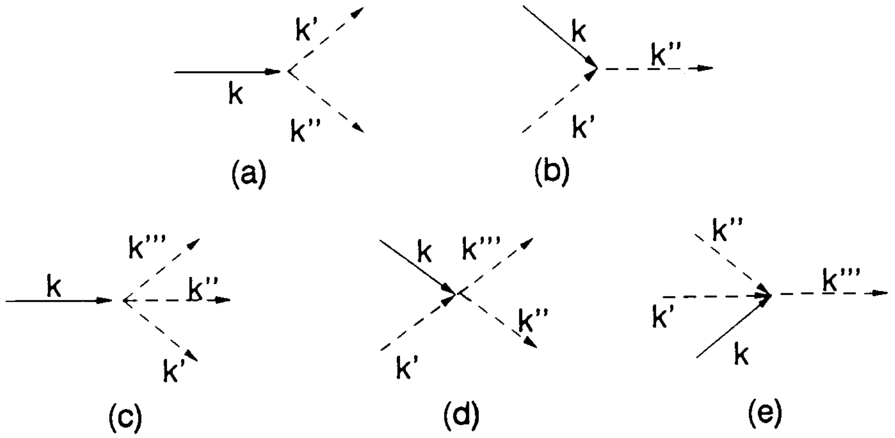

Figure II.2.1: Graphical representation of the third and fourth order contributions to the population and phase relaxation rate in a molecular crystal. (a) - (b): Cubic down- and up-conversion. (c)-(e): Quartic down-conversion, phonon-phonon scattering and up-conversion. Pure dephasing (f) is represented by diagram (d) with k''' = k.

The first two two contributions (a) and (b) are energy relaxation mechanisms which are third order in the crystal normal coordinates and by far the most commonly cited relaxation mechanisms in pure crystals. They correspond to three phonon processes whereby the initial phonon either splits into two new phonons of lower energy ((a), down conversion) or interacts with a higher energy phonon ((b), up conversion). The down conversion process leads to a finite relaxation rate at 0 K, whereas the up conversion gives zero contribution at low temperature. The next three contributions (c)-(e) arise from a fourth order interaction and are similar to the previous mechanisms, except that an additional phonon is required making this channel less likely in most circumstances. The process (f) contributes to the phase relaxation mechanism and consists of a fourth-order process, where the phonon frequency is modulated by exchange of two equal-frequency phonons on different phonon branches.

The temperature dependence of the linewidth is contained in the Boltzmann thermal occupation factors of the phonons involved. Impurities and defects which are presented in many real crystals can also effect the vibrational lineshape. These effects are most clearly seen at very low temperature where broadening due to thermal phonons is strongly reduced.

Crystal Impurities

The main source of impurities in molecular crystals are isotopic species present in natural abundance. These impurities do not effect the lattice phonons since the mass defects do not appreciably alter the intermolecular potential. In the case of high frequency vibrons these impurities introduce new energy levels that can serve as traps for vibrational energy, as long as the energy difference can be transferred to the thermal bath via acoustic phonons. In addition impurities can also scatter vibrons giving rise to dephasing.

Crystal Defects

In most real crystals a large concentration of defects exists due to strains and dislocations produced during the freezing process. The theory of disorder in crystals is well established and has been reviewed in a compact form by Elliott[47]. For molecular crystals Klaftner and Jortner[48] have treated the effect of crystal disorder on the lineshape of triplet excitons. This treatment has been extended by Hochstrasser[49] to the case of vibrons (vibrational excitons). The model gives the observed lineshape for the vibron as a function of the width W of the vibron band, the position of the $k=0$ state within this band, and the width σ of the distribution of site energies due to crystal disorder. Three cases can be distinguished:

(1) When $\sigma >> W$ the band is inhomogeneously broadened with width σ.

(2) When $\sigma << W$ a motional narrowing effect yields a symmetric Lorentzian line much narrower than σ.

(3) When $\sigma << w$ and the $k=0$ state lies near a band singularity of the vibron band the line is asymmetric and the coherence decay nonexponential.

The last case was used to explain the nonexponential vibrational relaxation in solid α-nitrogen which was observed in time resolved experiments by Abram et al[50].

Experimental Lineshape Contributions

Saturation Broadening

Just like a one-photon transition, a two-photon stimulated Raman transition can be driven into saturation if the driving fields are strong enough. What is meant by saturation can be visualized by considering a two level system coupled by, for the sake of simplicity, a one-photon transition. In the absence of the radiation field the population of the two levels relaxes to thermal equilibrium described by the Boltzmann distribution: $N_2 = N_1 \exp\{- \frac{\Delta E}{kT}\}$. In the presence of a resonant field the population will be described by a set of rate equations:

$$\frac{dN_1}{dt} = - \frac{dN_2}{dt} = - W(N_1(t) - N_2(t)) + \Gamma N_2 \qquad (2.21)$$

where $\Gamma = \frac{1}{T_1}$ is the relaxation rate of the upper level and $W = B_{12}I$ is the stimulated transition probability containing the Einstein coefficient B_{12}. With the field turned on the steady state population difference will be determined by the equilibrium between the driving field and relaxation processes:

$$\Delta N = \Delta N(I=0) \frac{1}{1 + 2BI\Gamma} = \Delta N_0 \frac{1}{1 + \frac{I}{I_{sat}}} \quad \text{with} \quad I_{sat} = \frac{1}{2\Gamma B} \qquad (2.22)$$

For $I << I_{sat}$ the system is in the so called small signal limit where the signal is proportional to the intensity: $\Delta N \cong \Delta N_0(1 - \frac{I}{I_{sat}})$ but for $I \cong I_{sat}$ the response of the system "saturates" and goes to zero for $I >> I_{sat}$. This type of behavior is often found in laser spectroscopy, although the situation is usually more complicated because more than 2 levels are involved which can be coupled by a variety of processes.

In SRS, saturation can occur if an appreciable fraction of the molecules are being pumped into the upper state. Since the susceptibility $\chi^{(3)}$ depends on the number density difference ΔN the SRS signal goes to zero when the transition saturates. To record "true" lineshapes which are not influenced by saturation it is important to remain in the small signal limit. To estimate the change in the population difference ΔN_R caused by the Raman pumping we divide eqn. (1.65) for the power change in the probe beam by the energy of one probe photon.

$$\Delta N_R = \frac{2\delta P_1}{\hbar\omega_1} = \frac{g}{(\hbar c)^2} P_1 P_2 = \frac{4\pi^2 c\ \Delta N}{n_1 n_2 \hbar^2 \omega^3} \frac{1}{\Gamma} \left(\frac{d\sigma}{d\Omega}\right) P_1 P_2 \tag{2.23}$$

Narrow Raman lines are saturated more easily than broad transitions as seen from the $\frac{1}{\Gamma}$ dependence of ΔN_R. Liquid nitrogen has a very narrow linewidth (Γ = 0.058 cm^{-1}) and is therefore a sample that should show saturation at relatively low power. With a value of $5.5 \cdot 10^{-31}$ cm^2 for the Raman cross section one calculates for the relative change in the vibrational population:

$$\frac{\Delta N_R}{\Delta N} \cong \frac{1.7 \cdot 10^{-8}}{(\text{Watt})^2} P_1 P_2 \tag{2.24}$$

This result shows that even in the quasi cw SRS experiments where the product $P_1 P_2$ is typically not larger than 10^6 (Watts)^2 saturation is not a problem. However, saturation can be observed in experiments that use two pulsed laser to pump a Raman transition such as CARS.

Optical Stark Effect on Ro-Vibrational Raman Transitions:

The strong electric field at the focus of a pulsed laser beam can lead to shifts of molecular energy levels through an "optical" Stark effect[51]. Both ro-vibrational and pure rotational spectra are affected, although the coupling mechanism differs in the two cases. For molecular vibrations the effect can be understood from the vibrational Hamiltonian in the presence of an optical field:

$$H = \frac{1}{2} m \dot{q}^2 + V(q) - \frac{1}{2} \alpha(q) E_L^2 \left(\frac{1}{2} + \frac{1}{2} \cos(2\omega_L t)\right) \qquad (2.25)$$

The laser field at ω_L couples through the polarizability $\alpha(q)$. The quadratic field dependence gives rise to a time independent term and a term oscillating at $2\omega_L$ which will be neglected subsequently because the oscillator cannot follow an oscillation at optical frequencies. The DC term will lead to a force on the molecule which changes the equilibrium internuclear separation q_e. By assuming a Morse potential

$$V(q) = D_e \{ 1 - \exp(-\beta(q-q_e)) \}^2 \qquad (2.26)$$

the change δq in the internuclear separation can be estimated:

$$\delta q = \frac{F}{k} = \left(\frac{E_L^2}{8D_e\beta^2}\right) \frac{d\alpha}{dq} \qquad (2.27)$$

where $F = -\frac{dV(q)}{dq}$ is the force on the molecule and $k = 2D_e\beta^2$ is the force constant of the molecule if one assumes a Morse potential. Since the change in q_e will affect the moment of inertia the rotational energy levels will be shifted by:

$$\delta\omega_R = - \omega_R^0 \left(\frac{E_L^2}{4D_e\beta^2 q_e}\right) \frac{d\alpha}{dq} \qquad (2.28)$$

The vibrational frequency will also be affected through the anharmonicity in the potential. The change in the force constant can be estimated by calculating $\frac{d^2V(q)}{dq^2}$ at the new internuclear separation $q_e + \delta q$. The new vibrational frequency is then:

$$\delta\omega_v = -\omega_v^0 \left(\frac{3\ E_0^2}{16De\beta}\right) \frac{d\alpha}{dq} \tag{2.29}$$

These equations show that the optical Stark shifts are quadratic in the total (nonresonant) electric field and linear in the polarizability derivative and thus depend on the square root of the spontaneous Raman cross section.

For an estimate of the magnitude of the effect on the Q-branch transition of N_2 we calculate with $\left(\frac{d\alpha}{dq}\right) = 1.7$ Å^2 and a field intensity of $7{\cdot}10^{10}$ J/cm^2 (15 mJ pump energy focused to beam waist of 75 μ) a shift of 0.01 cm^{-1}. Experimentally we have observed shifts for N_2 Q-branch lines of 0.015 ± 0.003. (see Fig. II.2.2) Reversing the calculation this shift gives a way to measure the peak intensity in the laser focus, which is more accurate then the value we obtained from a measurement of the pulse energy and beam waist size. Looking at Fig. II.2.2 one sees not only a shift of the lines to lower frequency, but also a significant broadening. This broadening is due to inhomogeneities of the electric field in the sampling volume, shot to shot pump power fluctuations and also the fact that the pulse has a Gaussian and not a square wave time profile. These effects, especially the latter, leads to a pump power dependent change of the observed line profiles which is shown in Fig. II.2.3. At low power the line is homogeneously broadened due to collisional broadening and the lineshape can be fit to a Lorentzian profile. At high pump power

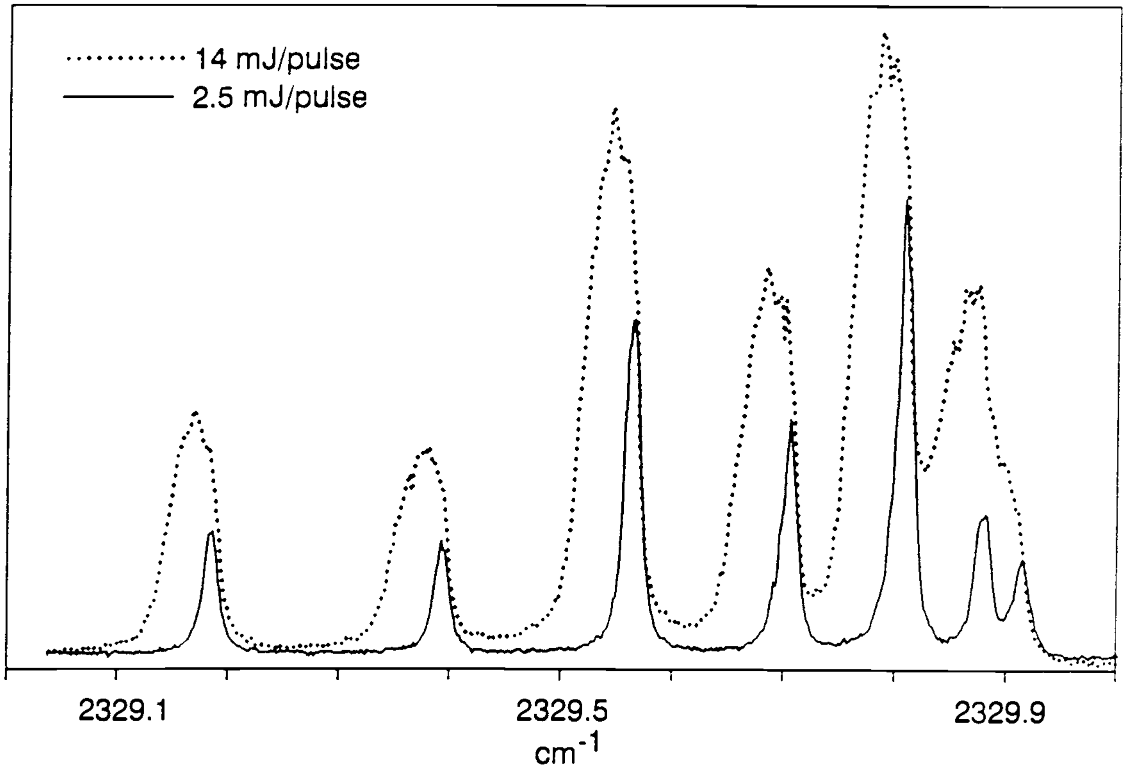

Figure II.2.2: Optical Stark effect on Q-branch spectrum of N_2.

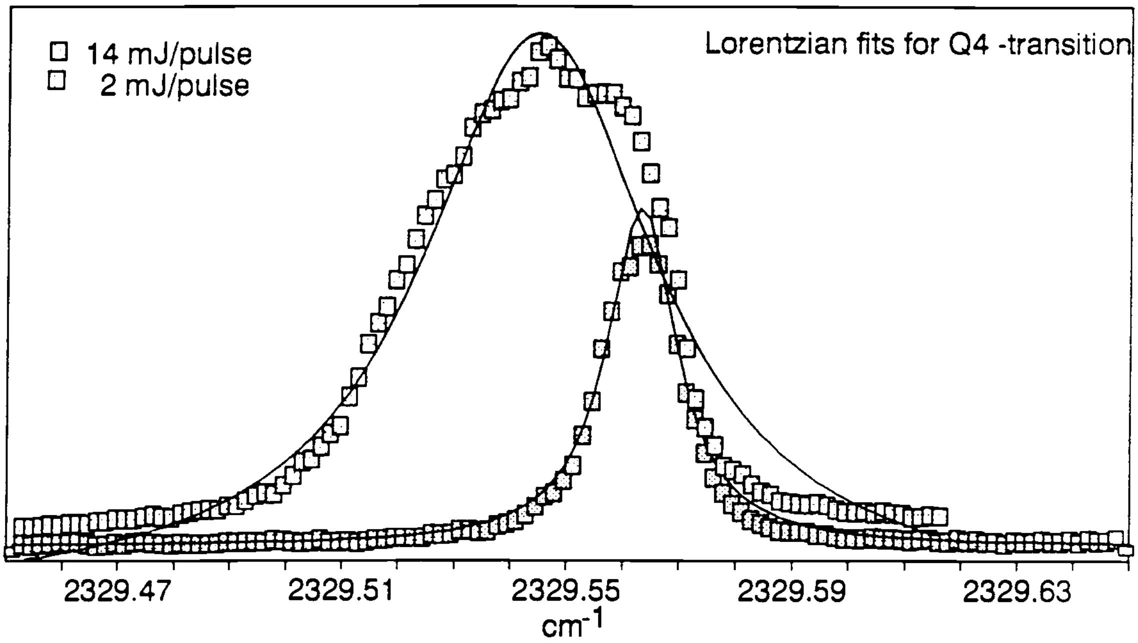

Figure II.2.3: Change in lineshape of Q_4 transition due to optical Stark effect.

the optical Stark effect distorts the lineshape causing steep shoulders and a flat maximum.

Pure Rotational Raman Transitions

There is another contribution to the optical Stark effect which is proportional to the polarizability anisotropy γ instead of the polarizability derivative $\frac{d\alpha}{dq}$. This effect can be observed in pure rotational Raman transitions where the shifts proportional to $\frac{d\alpha}{dq}$ are negligible in most cases (except for H_2). Farrow and Rahn[52] have first observed this effect in the pure rotational spectrum of N_2. Unlike the Stark effect associated with $\frac{d\alpha}{dq}$ which causes shift of the transition frequencies, the Stark contribution that operates through γ causes a splitting of the rotational lines as well as a shift of the line center.

The shifts for the energy levels of a rigid rotor can be calculated from the interaction Hamiltonian and the rigid rotor wave functions using time independent perturbation theory. The same Hamiltonian for the coupling between field and molecule is assumed here as in the previous section:

$$H' = -\frac{1}{2}\,\alpha\, E_L^2 \tag{2.30}$$

where the time dependent part is neglected again because of the high frequency of the optical field. The result of the perturbation calculation, to second order in the field, is:

$$\Delta E_{J,M} = \frac{1}{6}E_L^2\left\{\frac{3M^2 - J(J+1)}{(2J-1)(2J+3)}\right\}\gamma \tag{2.31}$$

This expression shows that each J level will be split into J+1 components since the ±M degeneracy is not removed by the field.

The observed splitting pattern in the rotational Raman spectra depends on the direction of polarization of pump and probe laser. This can be understood by combining the well known selection rules for one-photon transitions, which are $\Delta M = 0$ if the light is polarized parallel to the field and $\Delta M = \pm 1$ if the polarization of the light and the field direction are orthogonal. In ref 51 Farrow and Rahn have used three laser beams to investigate the $\Delta M = 0$ case (all beams parallel) and the $\Delta M = \pm 2$ case (pump and probe polarization orthogonal to the polarization of the laser producing the Stark field). In our experiment the Stark field is produced by the pump laser and therefore $E_{\mathrm{Stark}} \parallel E_{\mathrm{pump}}$ is always the case. However, rotational Raman spectra are usually recorded with crossed polarization of pump and probe beam to block scattered pump light with a polaroid filter. In this case, which is actually the most relevant in high resolution pure rotational SRS spectroscopy, the selection rules are $\Delta M = \pm 1$. We have investigated the optical Stark effect for several pure rotational N_2 transitions and compared the observed shifts and lineshapes with computer simulations based on eqn 2.31 for the level shift and intensities calculated from perturbation theory:

$$I_{J,M;J+2,M} = D \frac{[(J+1)^2-M^2][(J+2)^2-M^2]}{(2J+5)(2J+3)(2J+3)(2J+1)} \gamma^2 \quad \text{for } \Delta M = 0 \qquad (2.32)$$

where D is a proportionality constant.

$$I_{J,M;J+2,M\pm1} = D \frac{(J\pm M+1)(J\pm M+2)\{(J+2)^2-(M\pm1)^2\}}{(2J+1)(2J+3)(2J+3)(2J+5)} \gamma^2 \quad \text{for } \Delta M = \pm 1 \qquad (2.33)$$

Fig. II.2.4 shows several rotational lines of N_2 recorded at low and high pump power to show the effect of the Stark splitting and shift on the different lines. For the J=0 line, corresponding to a transition from J" = 0 to J' = 2, there is only one component since the J=0 level consists only of one sub level (M=0) and because of the selection rule $\Delta M = \pm 1$ transitions can only occur to the degenerate M = ±1 sub level of the J = 2 state. The line center is seen to shift to lower frequency with a shift proportional to the laser intensity. The broadening is again caused by inhomogeneities in the electric field, laser power fluctuations and the temporal pulse profile. In the simulated spectra field inhomogeneity is included but the electric field is taken as constant which causes the shoulders of the calculated profiles to be flatter than the experimental ones.

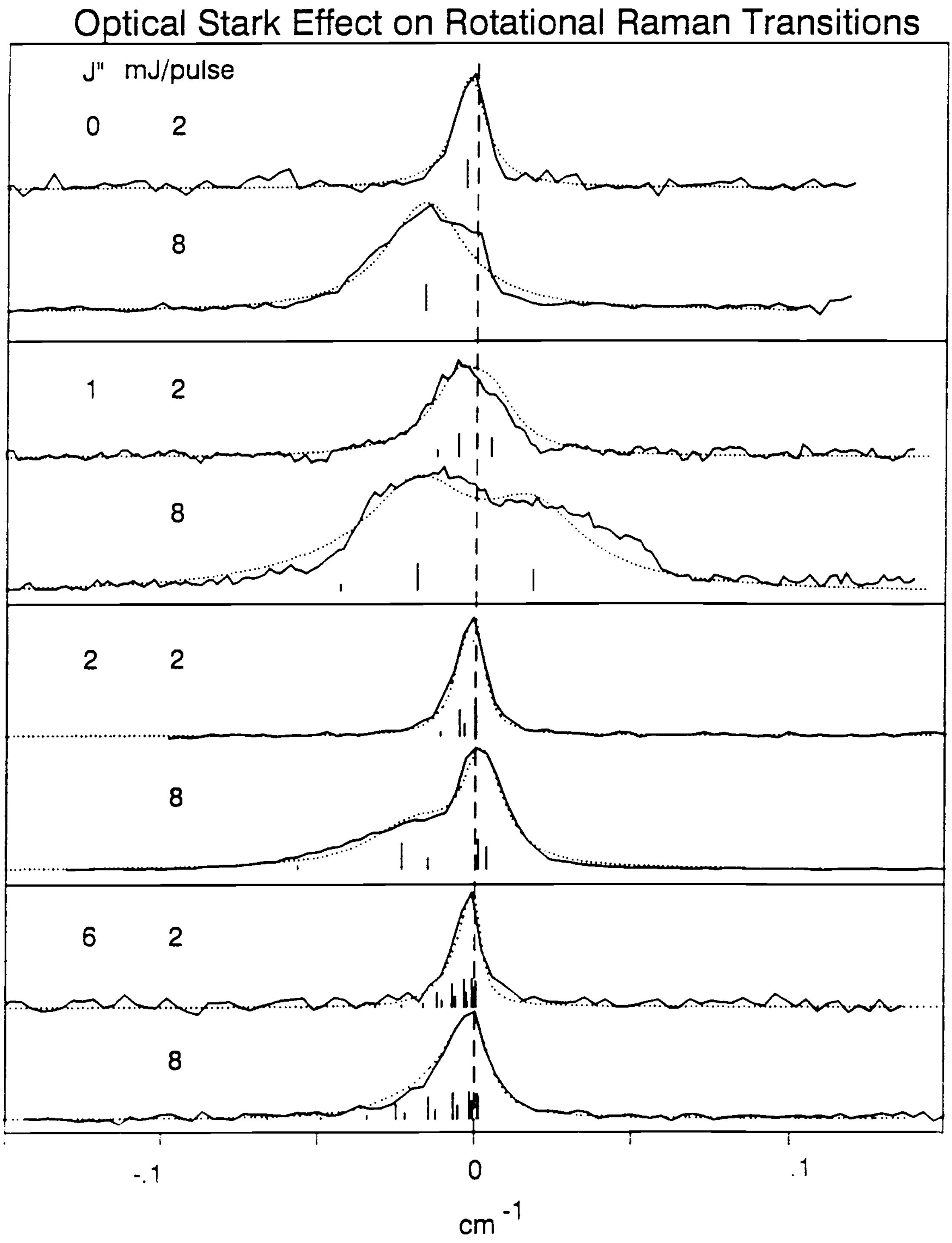

Figure II.2.4: Optical Stark effect on pure rotational Raman transitions of nitrogen. The unshifted position (zero field) is indicated by the vertical dashed line. The vertical bars show the center positions of the rotational sublevels (±M), split by the Stark effect. The dotted line shows a simulation of the Stark effect using eqn. 2.31 and 2.33 and a Lorentzian lineshape for each component.

3. FREE JET EXPANSIONS

Introduction

Free jet expansions are widely used in the spectroscopy of gas phase molecules to achieve conditions of very low temperature and collision rate[53,54]. Under these conditions line broadening due to the Doppler effect and pressure broadening are strongly reduced which makes it possible to resolve closely spaced transitions that would not be resolvable in static samples. In addition to the narrowing of the lines the cooling in the expansion causes a redistribution of the population into the lowest energy levels, which improves detection limits, simplifies the observed spectra, and aids in the assignment of the lines.

Another important feature of a free jet expansion is the formation of clusters[55]. Weakly bound molecular aggregates that are unstable under static conditions can be formed in sufficient concentration in free jets to be studied by spectroscopy. The cluster size can be controlled through the driving pressure, the reservoir temperature and by dilution of the sample with a carrier gas. Since we use free jets to study N_2 condensation by stimulated Raman spectroscopy, the relevant theory of free jet expansions and condensation is summarized in the following sections.

Isentropic Jet Expansion

A free jet expansion is formed when a gas under high pressure expands into a low pressure region through a small orifice. In the expansion thermal energy of the molecules is converted into kinetic energy associated with the mass flow. This process can be visualized by considering the distribution of molecular velocities in both cases shown in Fig. II.3.1. In the reservoir at thermal equilibrium the molecular velocity components along any direction are described by a Maxwell Boltzmann distribution centered at a mean value of zero since there is no net mass flow in this case. In the free jet the velocity distribution along the axis of the jet is centered about the flow speed (typically 500 m/sec). Because of the conservation of enthalpy the width in this case is greatly reduced which is indicative of a lower translational temperature. It should be mentioned that since the different degrees of freedom are not completely in equilibrium one defines temperatures for translational, rotational and vibrational motion which are generally different. Usually $T_{trans.} < T_{rot} << T_{vib}$ since the collision cross section for energy transfer is very different for the three cases.

Quantitatively, a free jet is best described as an isentropic and isenthalpic process i.e. a process in which entropy and enthalpy are conserved[56,57]. The three basic equations that describe the flow field are:

conservation of mass: $$\frac{1}{\rho}\frac{d\rho}{dx} + \frac{1}{v}\frac{dv}{dx} + \frac{1}{A}\frac{dA}{dx} = 0 \qquad (3.1)$$

conservation of momentum: $$\frac{1}{\gamma M^2}\frac{1}{\rho}\frac{d\rho}{dx} + \frac{1}{v}\frac{dv}{dx} = 0 \qquad (3.2)$$

conservation of energy: $$-\frac{1}{\rho}\frac{d\rho}{dx} + \frac{1}{\gamma p}\frac{dp}{dx} = 0 \qquad (3.3)$$

with: ρ density

v flow velocity

A area of stream tube

γ ratio of specific heats = $\frac{C_p}{C_v}$

M Mach number, i.e. ratio of flow speed to local speed of sound

No analytical solution for these equations has been found for the inviscid flow through a circular hole in a thin wall but Ashkenas and Sherman[58] showed that the properties along individual streamlines (stream tube theory) can be calculated numerically and that the results along the centerline of the jet can be described by the following fitting formula:

$$M = A\left(\frac{x - x_0}{D}\right)^{\gamma-1} - \frac{1}{2}\left(\frac{\gamma + 1}{\gamma - 1}\right)\frac{1}{A}\left(\frac{D}{x - x_0}\right)^{\gamma-1} \qquad (3.4)$$

The constants A and x_0 depend on γ and were determined by fitting the numerical data:

	γ	A	x_0/D
monoatomic	1.67	3.26	0.075
diatomic	1.40	3.65	0.40
polyatomic	1.2857	3.96	0.85

x_0 is the hypothetical origin of the streamlines slightly downstream from the nozzle opening (see Fig. II.3.2). Also shown in Fig. II.3.2 are the shock boundaries formed by the collision of the jet with the background gas. The lateral boundary is called the barrel shockwave

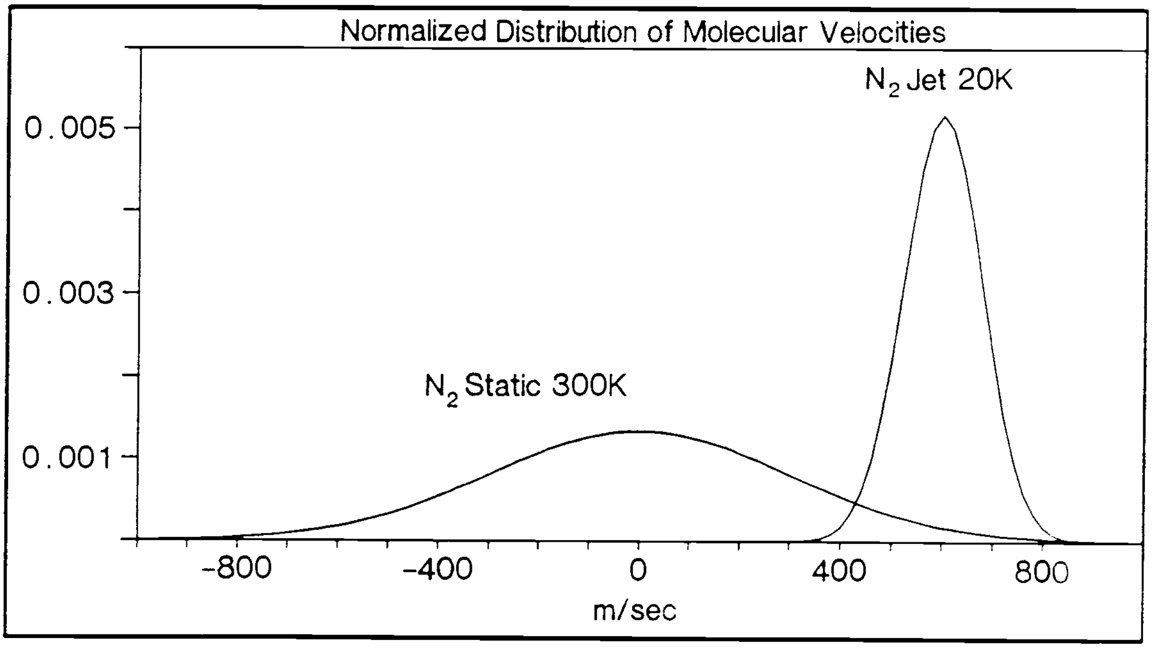

Figure II.3.1: Comparison of molecular velocity distribution in static gas and a free jet. In the jet the distribution is narrowed, indicating the cooling effect, and centered about the flow velocity.

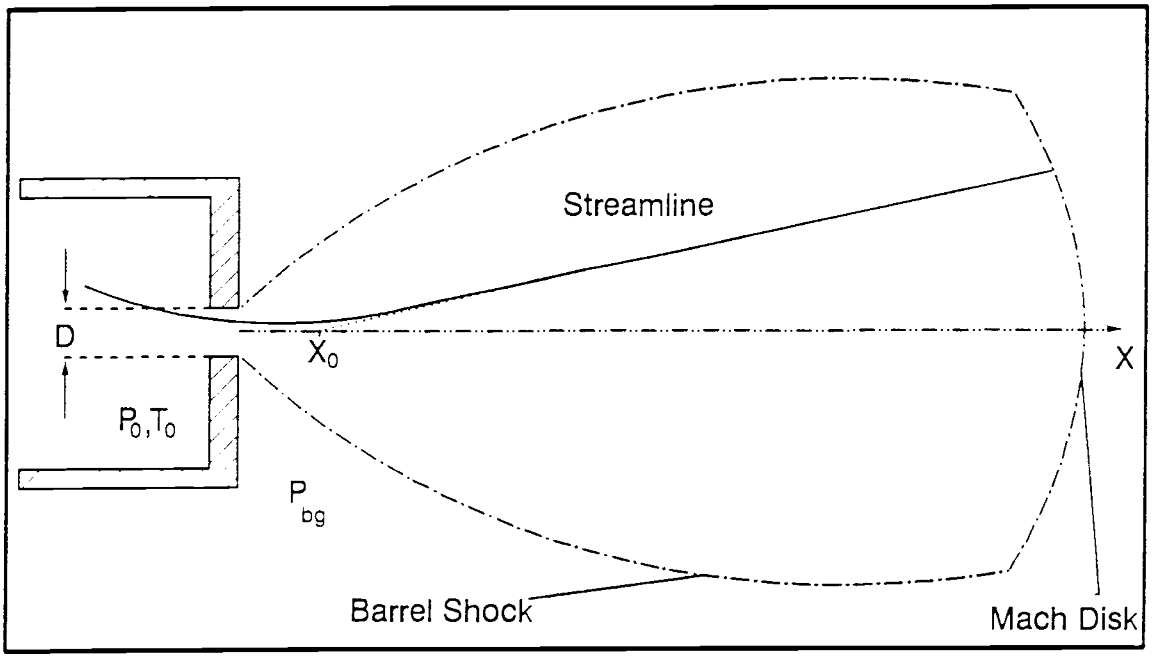

Figure II.3.2: Definition of terms used to describe a free jet expansion.

and the longitudinal boundary is referred to as the Mach disk. The location of the Mach disk depends on the ratio of driving pressure p_0 and background pressure p_{bg}.

$$\left(\frac{X}{D}\right)_{Mach} = 0.67 \left(\frac{p_0}{p_{bg}}\right)^{\frac{1}{2}} \tag{3.5}$$

The region inside the shock boundaries constitutes the free jet expansion and is sometimes called the "zone of silence".

Once the Mach number is known as a function of position in the jet then the translational temperature of the gas can be calculated from the conservation of enthalpy.

If h_0 is the enthalpy per unit mass in the reservoir then

$$h_0 = h + \frac{1}{2} v^2 \tag{3.6}$$

For an ideal gas:

$$h - h_0 = C_p (T_0 - T) = \frac{\gamma}{\gamma-1} r (T_0 - T) \tag{3.7}$$

where r is the gas constant per unit mass = $C_p - C_v$

The relation for an ideal gas between the speed of sound and the temperature T is:

$$a = (\gamma r T)^{1/2} \tag{3.8}$$

Combining (3.6) - (3.8) we get:

$$\frac{T}{T_0} = \left(1 + \left(\frac{\gamma-1}{2}\right) M^2\right)^{-1} \tag{3.9}$$

For an isentropic process in an ideal gas: $P = \text{const}\ \rho^{\gamma}$. With this relationship and the ideal gas law one can also write equations for density and pressure as a function of the Mach number.

$$\frac{P}{P_0} = \left(1 + \left(\frac{\gamma-1}{2}\right) M^2\right)^{\frac{\gamma}{1-\gamma}} \tag{3.10}$$

$$\frac{\rho}{\rho_0} = \left(1 + \left(\frac{\gamma-1}{2}\right) M^2\right)^{\frac{1}{1-\gamma}} \tag{3.11}$$

Fig. II.3.3 shows the variation of the physical quantities with X/D:

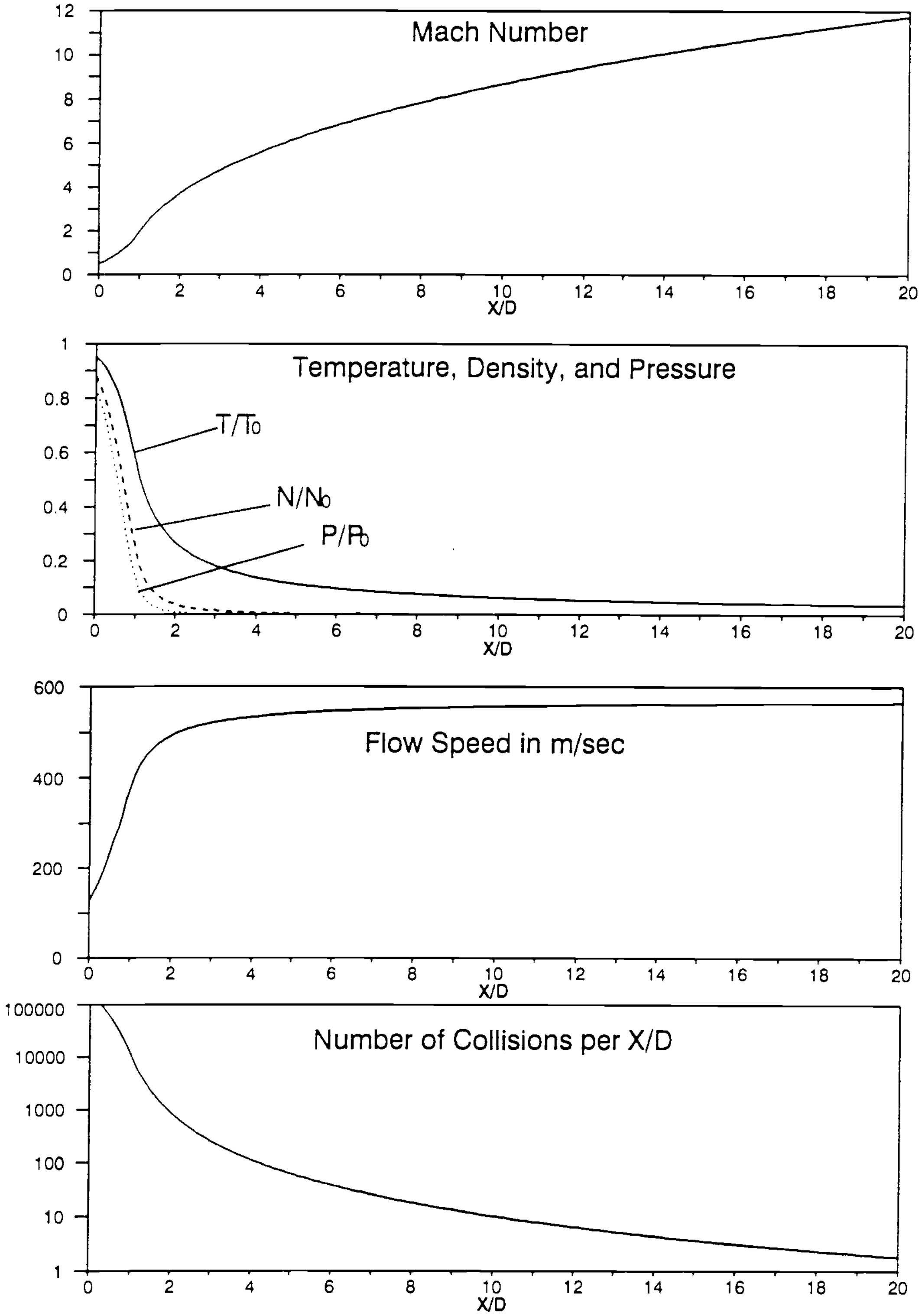

Figure II.3.3: Results of Ashkenas and Sherman theory for free jet expansion of N_2 with $P_0 = 30$ atm, $T_0 = 160$ K.

Condensation in Jet Expansions

The preceding discussion was limited to an isentropic expansion. Koppenwallner et. al[59]. have extended the free jet theory of Ashkenas and Sherman to condensing jets. If condensation occurs in the expansion the continuity equations have to be modified to include the heat input and the mass reduction due to the condensation.

mass conservation: $$\frac{1}{\rho}\frac{d\rho}{dx} + \frac{1}{u}\frac{dv}{dx} + \frac{1}{A}\frac{dA}{dx} = -\frac{1}{m}\frac{dm_{cond}}{dx} \qquad (3.12)$$

momentum conservation: $$\frac{1}{\gamma M^2}\frac{1}{\rho}\frac{d\rho}{dx} + \frac{1}{v}\frac{dv}{dx} = 0 \qquad (3.13)$$

energy conservation: $$c_p\frac{dT}{dx} + v\frac{dv}{dx} = \frac{H_{cond}}{m}\;\frac{dm_{cond}}{dx} \qquad (3.14)$$

The condensation rate input $\frac{dm_{cond}}{dx}$ can be calculated from classical condensation theory[60].

Classical Condensation Theory

The theory is based on: (1) the nucleation process, (2) the growths of individual droplets, and (3) integration of droplet formation and droplet growths along the free jet to obtain the total number density of droplets and the condensed mass fraction.

Nucleation occurs when droplets of the critical size r* are formed. For a given value of supersaturation droplets with r smaller than r* will evaporate and larger ones will grow. The radius r* of the critical droplet and its surface area A* are given by:

$$r^* = \frac{2\,\sigma(T)\,V_m}{kT\,\ln\left(\frac{p}{p(T)_{vap}}\right)} \qquad (3.15); \qquad\qquad A^* = 4\pi r^{*2} \qquad (3.16)$$

where σ and p_{vap} are the surface tension and the vapor pressure of the condensed phase.

The number density n_c^* of critical droplets is:

$$n_c^* = n \exp\left[- \frac{\Delta G^*}{kT}\right] \tag{3.17}$$

where n is the number density of the gas and ΔG^* is the Gibbs free energy of formation of a critical droplet. The nucleation rate (rate of formation of supercritical droplets of radius $r > r^*$, i.e. nuclei) is given by the number of molecules impinging on the surface of the critical droplets at a flux $n\,\bar{v}\,A^*$:

$$J = n_c^*\, n\, \bar{v}\, A^* = n\, n\, \bar{v}\, A^* \exp\left[- \frac{\Delta G^*}{kT}\right] \tag{3.18}$$

with

$$\frac{\Delta G^*}{kT} = \frac{16\pi}{3}\left[\frac{\sigma(T)\ V_m^{2/3}}{kT}\right]^3 \tag{3.19}$$

The subsequent growth of the condensation nuclei is described by the Hertz-Knudsen formula which gives the growth rate $\frac{dm(r)}{dt}$ for a particular droplet size as the difference between condensation and evaporation:

$$\frac{dm(r)}{dt} = \frac{4\pi^2 r}{(2\pi RT)^{1/2}}\ (\ p - p_{vap}(T,r)) \tag{3.20}$$

Düker and Koppenwallner[61] used these relations in computer calculations of nitrogen condensation in free jets. It is instructive to give some of their results here since they provide at least a qualitative description of a condensing free jet of N_2.

Before condensation occurs the system moves along an isentropic line in the p-T diagram shown in Fig. II.3.4. Depending on the starting conditions both liquid and solid are traversed or just solid condensate is formed. The true onset of condensation and freezing does not occur at the points predicted by the equilibrium phase diagram because of supersaturation and supercooling effects. As soon as condensation starts the system leaves the isentrope and follows a path qualitatively indicated by the dashed line in Fig. II.3.4. Condensation proceeds until the vapor is no longer saturated. From there the system continues along a new isentropic line.

Fig. II.3.5 shows the nucleation rate and the condensed mass fraction as a function of X/D. It can be seen that condensation occurs in a narrow X/D range in the early stages of the expansion and that the condensed mass fraction quickly reaches a constant value. Pressure and translational temperature decrease more slowly than in an expansion without condensation because of the heat input.

Growth curves for different nucleus sizes in Fig. II.3.6 predict a relatively narrow size distribution due to the rapid decrease in the nucleation rate with X/D.

It should be noted that the results of these calculations depend strongly on the numerical values for the surface tension of the condensate. Agreement with experimental data was achieved by adjusting the value of the surface tension of solid nitrogen and assuming that it is independent of temperature.

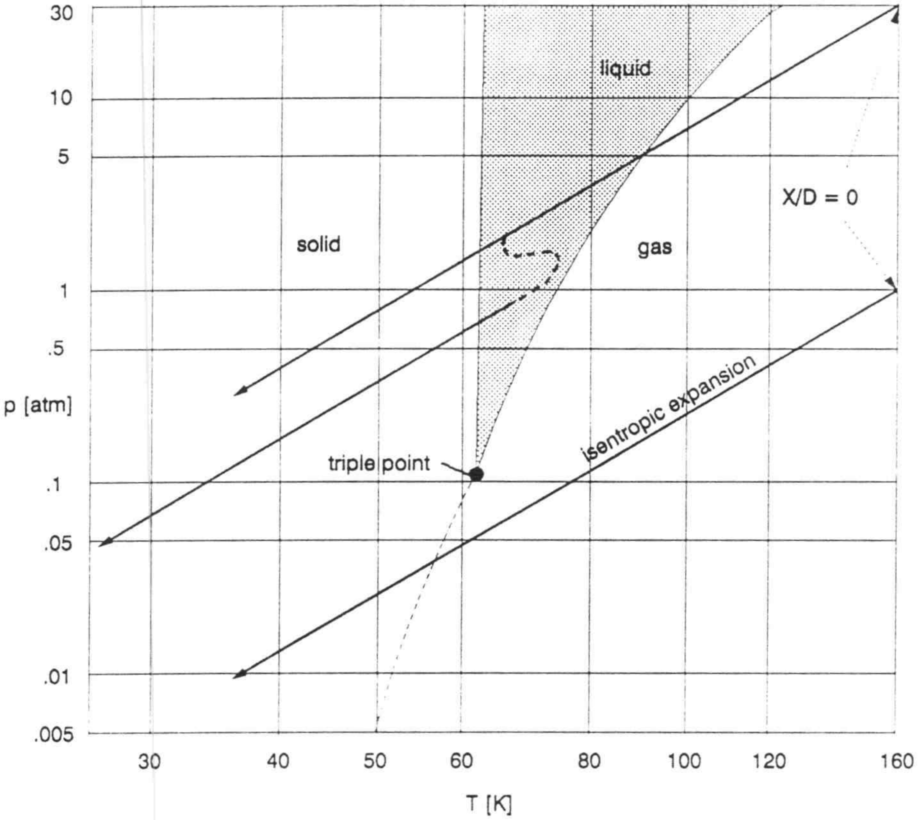

Figure II.3.4 Phase diagram of nitrogen with three isentropes corresponding to different reservoir conditions. Depending on the starting conditions the condensation can occur to the liquid phase followed by freezing or the solid phase can be formed directly. Because of supersaturation the condensation does not occur at the points predicted by the equilibrium phase diagram. After the onset of condensation the expansion is no longer isentropic which is indicated by the dashed curve. When the condensation has stopped, due to the rarefaction in the jet, the expansion continues on a different isentrope.

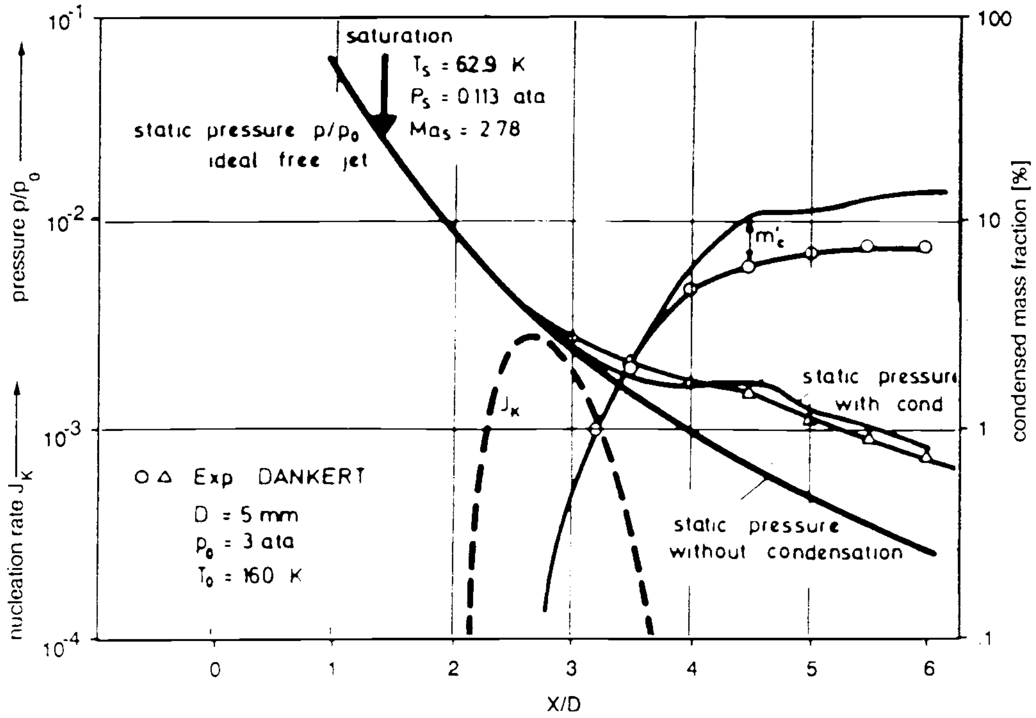

Figure II.3.5: Derived from Fig. 5 of reference 61: Theoretical predictions (solid lines) of static pressure and condensed mass ratio in the free jet. The dashed line is theoretically predicted nucleation rate. Circles and triangles show experimental data from pressure measurements[62].

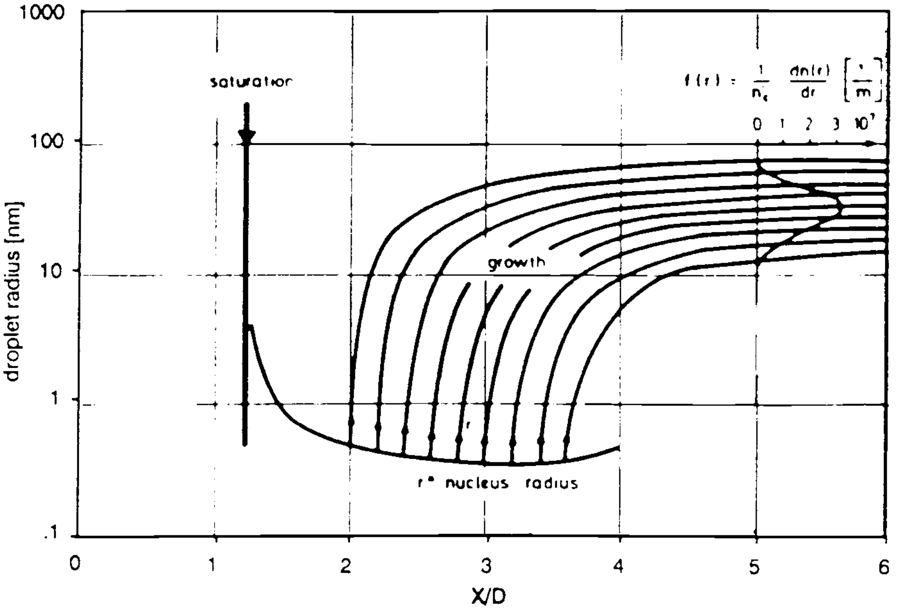

Figure II.3.6: Derived from Fig.4 of ref. 61. Theoretical predictions for droplet radius and growths map for different condensation nuclei. (P_0= 3 atm, T_0= 160 K)

CHAPTER III: THE STIMULATED RAMAN SPECTROMETER

INTRODUCTION

The high resolution stimulated Raman spectrometer is a powerful and versatile, but also complex and expensive research tool. To our knowledge only five other comparable instruments exist worldwide. The initial setup and design was done by Dr. George Pubanz as part of his dissertation[62] in our research group. The present thesis has involved further work on the development of the spectrometer to improve the sensitivity and to widen the range of applications. The tuning range of the spectrometer was expanded to the low-shift region where low frequency vibrational as well as pure rotational Raman spectra can be recorded down to zero wavenumber shift. The first research applications of the spectrometer were to record high resolution gas phase Raman spectra in static samples and more importantly in free jet expansions where the effect of cluster formation and phase transitions on the Raman spectrum for N_2 was observed for the first time with the SRS technique.

It became clear that the high resolution capability of the spectrometer would also prove to be useful for the study of cold molecular condensed phases. Therefore the spectrometer was modified to record spectra of molecules in condensed phases at low temperature by freezing the sample on a cold (15 K) sapphire window or by the use of a specially designed sample cell. For condensed phases a cw mode of operation was implemented that can achieve even higher resolution (≅10 MHz) than the pulsed quasi-cw technique.

In this chapter a general description of the stimulated Raman spectrometer and its components will be given followed by a selection of representative spectra that serve to characterize the capability of the spectrometer at its present stage of development.

Fig III.1 shows a schematic of the SRS spectrometer. Briefly, it consists of a tunable pump laser and a fixed frequency probe laser because in SRS the Raman spectrum is recorded by scanning the frequency difference between two lasers interacting with the sample. The pump laser system produces powerful (up to 20 mJ/pulse) single frequency pulses of 10 nsec duration, by injection seeding a home built three stage pulsed dye amplifier (PDA). The probe light comes from a single frequency argon or krypton ion laser. Raman shifts from 4700 to 0 cm^{-1} can be accessed by using different laser lines of the argon or krypton ion laser. The scan range for any given probe laser frequency is given by the range of the PDA, which is about 300 cm^{-1} for a given dye. Table III.1 shows the tuning range of the SRS spectrometer and the different probe laser frequencies that can be used for a given Raman shift.

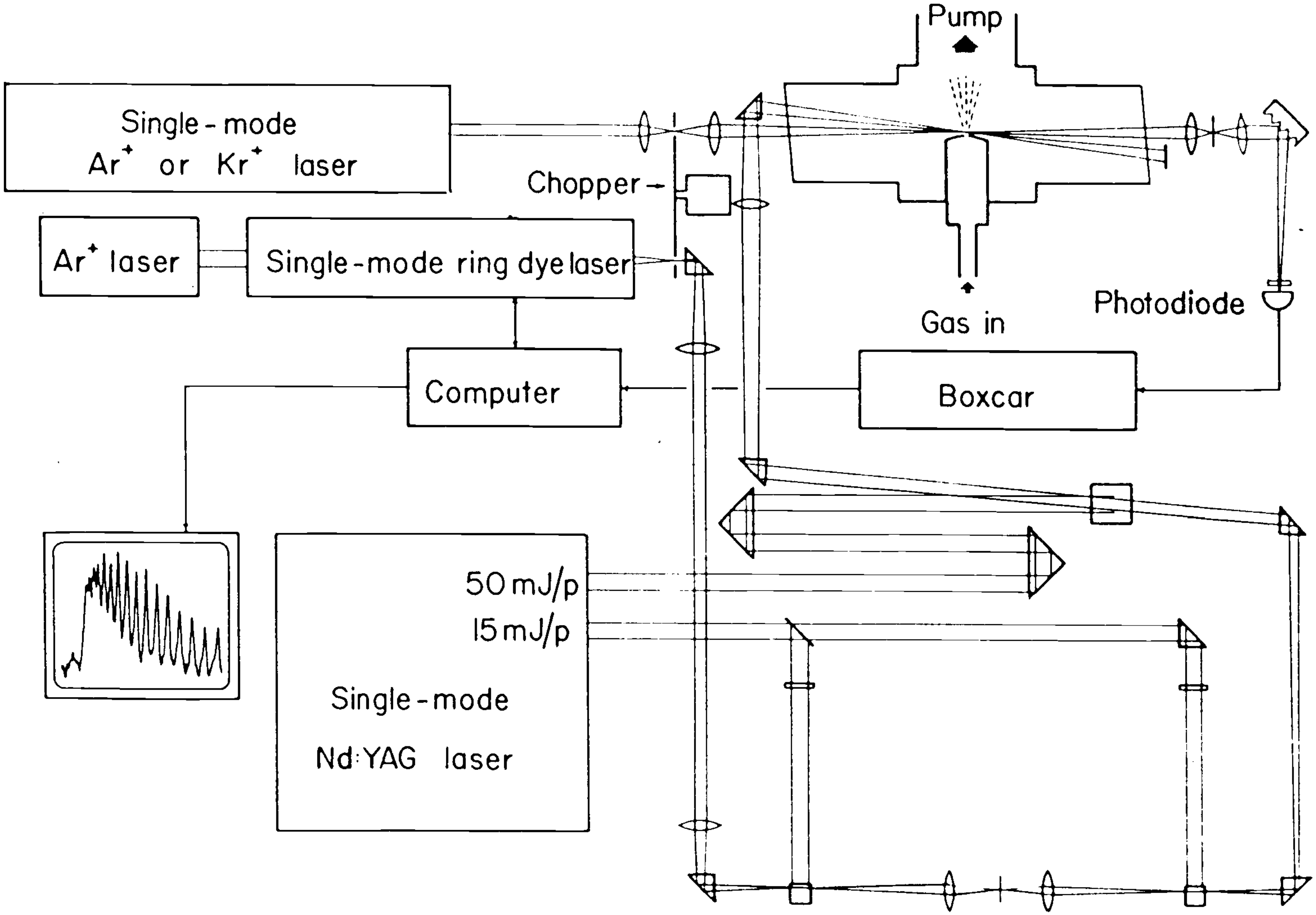

Figure III.1: Schematic of high resolution stimulated Raman spectrometer.

Table III.1 Tuning Range of the SRS Spectrometer

	Probe Laser			Raman Shift		
	λ [Å]	$\bar{\nu}$ [cm^{-1}]	Power [mW]	Max	Center [cm^{-1}]	Min[a]
Ar	4765	20981	300	4781	3881	3381
Ar	4880	20487	750	4287	3387	2887
Ar	4965	20135	300	3935	3035	2535
Ar	5017	19926	200	3729	2829	2329
Ar	5145	19439	1000	3230	2330	1830
Ar	5287	18914	110	2714	1814	1314
Kr	5208	19194	70	2994	2094	1594
Kr	5309	18832	200	2632	1832	1232
Kr	5682	17595	250	1395	495	-5
Kr	6471	15449	800	-751	-1651	-2151
Kr	6764	14779	200	-1421	-2321	-2812

a) Use of a high reflector coated for R 560 (# 453-04) for mirror M-5 will extend this range by 100 cm^{-1}.

To record a SRS spectrum a sample is brought into the focal region of the intersecting pump and probe beams. The sample can be a gas, liquid or solid as long as it is transparent to the laser beams used in the experiment. The probe laser intensity is monitored with a fast photodiode and when the frequency difference $|\omega_{\text{pump}} - \omega_{\text{probe}}|$ matches a Raman active resonance of the sample the Raman signal is detected as a small change in the intensity of the probe laser. Chopping the probe laser beam into 200 μsec pulses reduces the average power that is hitting the detector to avoid saturation. The seeding input to the PDA is also chopped in order to reduce thermal effects in the dye cells. The timing of the YAG laser is adjusted so that the output of the PDA occurs during the 200 μsec probe interval and a small part of the pump light is used to trigger the boxcar integrator. There are two boxcar channels, one of which is integrating the transient gain or loss in probe laser power over 12 nsec while a second channel is delayed by 15 nsec to integrate a 12 nsec window of the baseline. This baseline value is the electronically subtracted in an analog module to cancel out baseline shifts caused by lower frequency noise. The analog output of the boxcar average is then digitized by the interface electronics and can be averaged over many laser shots by the data collection program. More sophisticated data processing such as ratioing by the pump laser power on every shot was made possible by modifying the software to send the collected data after every shot from the Apple computer to a faster and more powerful IBM compatible microcomputer. This approach was necessary because the Apple IIe computer is already used to such an extent for controlling the ringlaser and the wavemeter that there is no time left for real time data processing. In the following sections the main components of the spectrometer will be described in more detail.

RING DYE LASER

Since this laser with its integrated wavemeter and computer control system forms the central part of the data acquisition system in the SRS spectrometer its function and theory of operation are described in some detail in the appendix. The operation and alignment of the ring laser system is fairly complex because of the many components that interact in the system. Therefore it is necessary to have a good understanding of the theory of operation as well as considerable experience with the alignment procedure and a good idea how a well aligned and adjusted system should behave. Much of this experience was gained during a two week user training at Coherent Inc.

in Palo Alto, CA. Since much of the material and information provided in the course is not included in the regular operating instructions the appendix also serves the function of collecting the relevant information in one place. For the purpose of describing the spectrometer the important properties of the ring laser are summarized below.

The Coherent 699-29 is a tunable single frequency laser with a traveling wave ring cavity. It delivers an output power of up to 800 mW with less than 1 MHz linewidth for Rhodamine 590 dye pumped with 5 Watts all-lines from a small frame argon-ion laser (Coherent Innova-90). The dye laser frequency is actively stabilized by locking it to a temperature controlled reference cavity. An integrated wavemeter allows positioning of the laser frequency and provides the frequency calibration for the laser scans. The laser and the wavemeter are interfaced to a Apple IIe microcomputer which scans the laser and controls the intracavity tuning elements throughout the scan. Automatic scans over hundreds of wavenumbers are possible under computer control by adding up 10 GHz scan segments with the help of the wavemeter. The computer can also collects data in three 12 bit A/D channels during the scan.

ND:YAG LASER

The requirements on a laser source to pump a pulsed dye laser amplifier for high resolution spectroscopy are:

- smooth temporal (Gaussian) pulse profile with maximum pulse length to minimize the spectral width of the output pulses. From the uncertainty principle the width (FWHM) for an ideal Gaussian pulse in Hz is given by $\Delta f = \frac{2\ln 2}{\pi \cdot \Delta\tau} \cong \frac{0.44}{\tau}$. If there is a fast amplitude modulation due to mode beating present in the pulse the spectral width will increase drastically.

- Gaussian spatial profile without hot spots to avoid damage to the optical components in the amplifier.
- high output power (> 50 mJ/pulse)
- wavelength suitable for pumping laser dyes in the 560-620 nm range (Rhodamine 590, 610)

The frequency doubled output of the Molectron MY34-10 used in the SRS spectrometer is a good match for these requirements. The Molectron Nd:YAG laser uses a polarization coupled unstable resonator (see Fig. III.2 for optical schematic) which produces a spatial beam profile that is very near Gaussian and does not have the characteristic "donut" profile of the more commonly used diffraction coupled resonators. The polarization coupling also allows the pulse length to be varied between 10 and 30 nsec depending on how quickly the energy is coupled out of the oscillator cavity. A long pulse gives a narrow spectral width but the reduced peak power results in lower doubling efficiency in the SHG crystals and lower efficiency of the pulse amplifier. Since we use the SAM (*single axial mode*) option to pump the PDA the pulse length is fixed at 20 nsec FWHM.

The SAM option[63] uses two additional optical elements, the *SAM etalon* and the *unetalon*, in the oscillator cavity to achieve lasing in

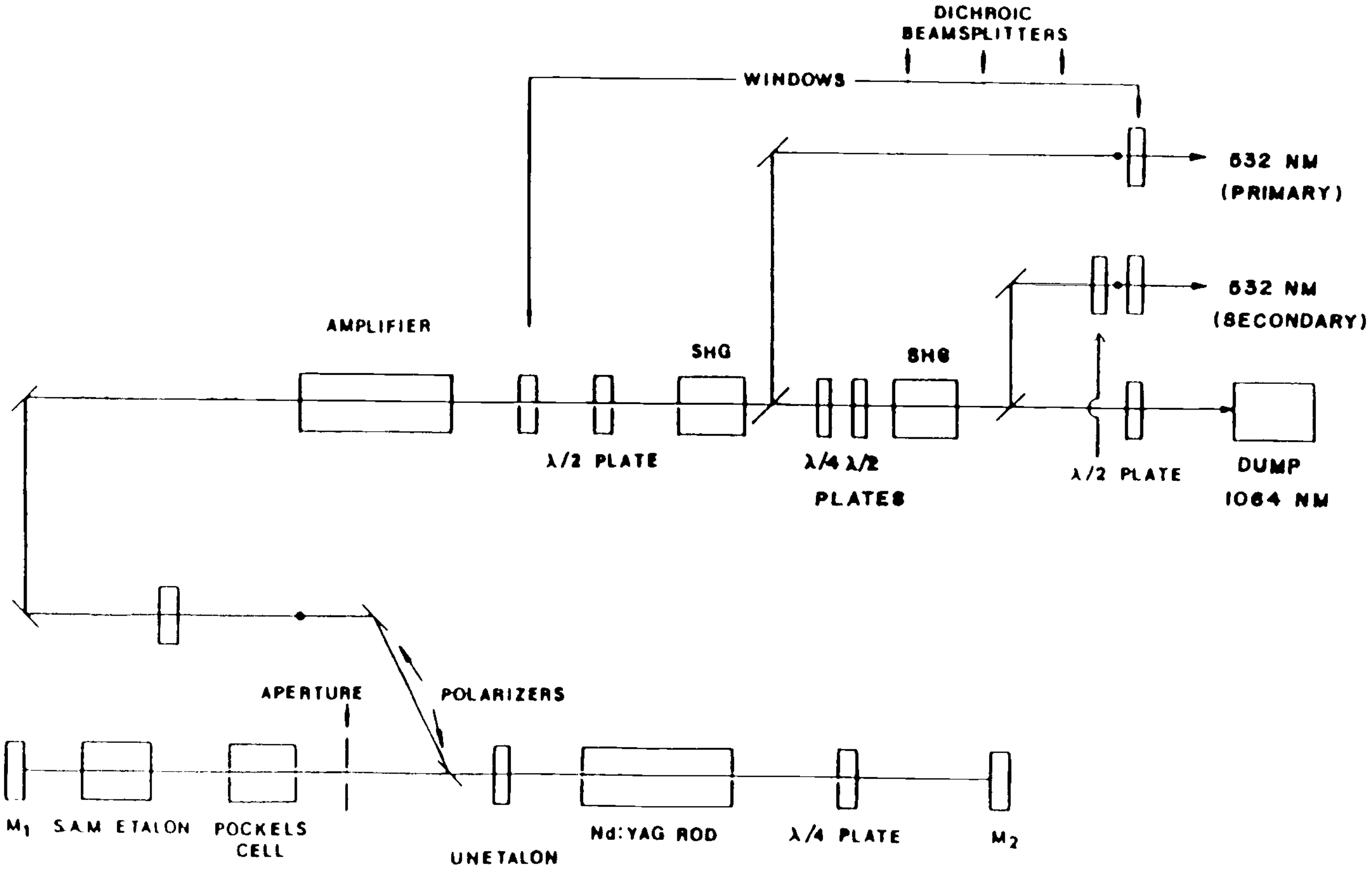

Figure III.2: Optical schematic of Molectron MY 34-10 Nd:YAG laser with single axial mode (SAM) option installed.

a single longitudinal mode. The basic oscillator cavity has a band width of about 15 GHz or 125 longitudinal modes. The SAM etalon (0.25 cm^{-1} FSR) reduces lasing to 2-5 axial modes but it cannot suppress lasing on modes adjacent to the desired cavity mode. Lasing on only two or three modes is particularly troublesome if one wants a smooth temporal pulse because of the strong amplitude modulation produced by the beating of two equally powerful modes. To restrict lasing to a single mode an unetalon[4] is inserted in the cavity to form a shorter subcavity together with the rear mirror M2. Since the length of the subcavity is about half of that of the oscillator cavity length the mode spacing for the subcavity is twice as large and therefore it will not support lasing on the troublesome adjacent oscillator cavity modes. Besides the two additional optical elements there is also a change in the electronic circuit that controls the Q-switch in the SAM option. After the flashlamps have fired, with the Q-switch still closed, lasing will start in the subcavity. A photodiode is used to monitor the light level in the subcavity and causes the Q-switch to slowly open when sufficient "prelasing" is detected. By opening the Q-switch slowly it is ensured that the light has traveled enough roundtrips through the frequency selective elements so that lasing on one longitudinal mode is established before most of the gain is used to amplify the existing mode.

---

[4] the element is called an unetalon to emphasize that it is not another etalon in the cavity, but is used as a partial reflector to establish a subcavity together with the end mirror M2. One side of the unetalon is anti-reflection coated to prevent it from functioning as a normal etalon.

In this way the SAM option delivers single mode pulses with a near Gaussian temporal profile. However, the output pulse is not always from the same longitudinal cavity mode, a feature which is irrelevant for pumping a PDA but becomes important if the Nd-YAG output is used directly for spectroscopic experiments such as SRS or CARS. In this case the resolution is limited by the shot to shot frequency fluctuations which are estimated to be ± 300 MHz (two longitudinal modes). The technique of injection seeding of the pulsed laser with a cw-diode laser is preferred for these applications.

After the light leaves the oscillator an amplifier stage amplifies the output to about 300 mJ/pulse before the IR is frequency doubled in type II KDP crystals and then used to pump the PDA.

PULSED DYE AMPLIFIER

The pulsed dye amplifier (PDA) in the SRS spectrometer is based on published designs by Drell and Chu[64] and Esherick and Owyoung[65]. The optical layout of the amplifier is shown in Fig. III.2. The seeding input is focused into the first transversely pumped amplifier stage. This stage receives about 5 mJ/pulse pump energy focused to a line with a cylindrical lens and provides a gain of 10^3. The dye beam is then sent through a pinhole to filter out unwanted ASE (amplified spontaneous emission). After the pinhole the beam is refocused into the second amplifier stage which is transversely pumped with about 15 mJ/pulse for a gain of 10^2. The final amplifier stage is longitudinally pumped with the unfocused beam of typically 50 mJ/pulse providing another factor of 10 gain. The dye beam is expanding after the second amplifier cell and its beam diameter is matched to the pump beam inside the third stage of amplification. The dye solution is circulated through the amplifier stages to prevent thermal lensing and to avoid triplet absorption by excited dye molecules. The dye concentration is the same for the first two stages and a factor of 10 more dilute for the final stage. Typical output power is 5 to 10 mJ/pulse. With high pump energy as much as 20 mJ/pulse output energy can be obtained. The pulse width and shape was checked with a fast photodiode and a 500 MHz Tektronix 7834 storage oscilloscope and found to have a smooth temporal profile and a FWHM of 10 nsec corresponding to a Fourier transform limit of 44 MHz for an ideal Gaussian time profile. The resolution of the spectrometer was determined to be about twice this value[63] or 100 MHz. The difference is due to a non-Gaussian temporal pulse profile and also due to jitter and short term drift (≅ 10 MHz) of the probe laser.

PROBE LASERS

The most important requirement on the probe laser in a Raman gain/loss experiment is amplitude stability in the frequency range of the Raman signal. For high resolution work a narrow spectral linewidth is also required. An argon or krypton ion laser with an intracavity etalon meets these requirements well. The intracavity etalon forces the laser into single mode operation which results in very narrow linewidth and also high amplitude stability in the frequency region above 100 KHz, since mode beating, the main source of amplitude noise at these frequencies, is eliminated. The instantaneous spectral width of the laser is very small (< 1 Hz) so that the short term line width is determined by the frequency stability of the laser. The frequency stability of an ion laser is directly related to the length stability of the resonator cavity which is affected by two factors: thermal expansion of the resonator structure causing slow frequency drift, and mechanical vibrations which cause microphonic movement of the cavity mirrors responsible for fast frequency jitter.

Thermal frequency drift is minimized by using materials with a low temperature expansion coefficient for the resonator frame or by including a bimetallic temperature compensation, where materials with different thermal expansion coefficient are used in such a way that the expansion is compensated. The argon laser, a Spectra Physics 165 with a model 583 solid etalon, has a quartz rod resonator which is temperature compensated to reduce the frequency drift below 60 MHz/°C. The specification for the short term (< 1 sec) frequency stability is ± 8 MHz for the Spectra Physics laser. The temperature of the etalon is stabilized to 0.01 °C which translates into a maximum frequency drift of ± 20 MHz. For the Coherent Krypton ion laser the frequency stability is specified to be better than 5 MHz for 1 sec and 38 MHz for 1 hour. Since the these frequency changes are smaller than the resolution of the spectrometer the frequency stability of the probe laser is regarded as sufficient. Better frequency stability could be achieved by locking the laser frequency to a molecular resonance such as a hyperfine component of an electronic transition of I_2[66].

DETECTION SYSTEM

The SRS signal is a transient change for about 10 nsec in the probe laser power that occurs instantaneously when the pump laser is fired and the frequency difference matches a Raman resonance of the sample. The two main requirements on the detector are (1), a fast enough time response to follow the SRS signal and (2), the ability to handle as much laser power as possible to reduce the shotnoise limit in the signal detection. Silicon avalanche photodiodes combine the two properties of short response time and large photocurrent capability. The detector that is used in the experiment is a EG&G FND100 avalanche photodiode which has a specified response time of < 1 nsec if biased in reverse at 90 V. The maximum current without saturation is specified at 300 mA for detection of fast pulses as long as the power dissipation limit is not exceeded. Experimentally, we found that the photocurrent had to be kept below 60 mA to avoid severe saturation of the high frequency response even for the short 200 μsec probe laser pulses. This limits the maximum probe laser power at the detector to 200 mW for 514.5 nm. It should be noted that for such high power levels the beam has to spread out evenly over the active area of the detector (5.2 mm^2 for FND100), otherwise saturation will occur at a lower power.

One also has to ensure that the power supply for the reverse bias voltage is able to supply the peak current without significant change in the bias voltage in order to keep the detector response linear. The four 22.5 V batteries used in our experiments could not supply 60 mA of current without significant voltage drop due to their internal resistance. This problem was solved by adding a large capacitor which could supply the photocurrent during the fast 200 μsec light pulse and then would be recharged by the batteries during the 100 msec period before the next pulse.

Good shielding against rf pickup is essential and was the primary reason for using batteries as a power supply. The photodiode is contained in a doubly shielded housing which is connected to the preamplifier by a short BNC cable. The signal is ac-coupled into the preamplifier through a 270 pF capacitor to filter out frequencies below 10 MHz. The preamplifiers were either a pair of cascaded COMLINEAR CLC 100 video amplifiers with a bandwidth from DC to 300 MHz and a total gain of 100 or a three stage AVANTEK amplifier with a bandwidth from 5 to 500 MHz and a gain of 10^3. The latter amplifier was used for very weak signals and had the advantage of better low frequency noise rejection than a simple RC filter, but the disadvantage of a smaller dynamic range. The output of the preamplifier is connected to the input of two STANFORD RESEARCH SYSTEMS BOXCAR INTEGRATORS (MODEL SRS 250) which provide an adjustable gain of up to 200 before integration. The boxcar units are triggered by a photodiode monitoring the YAG output. The gate of the first channel is adjusted to integrate the Raman signal over a 12 nsec time window and the second channel integrates an identical interval of the baseline just after the SRS signal has disappeared. The 0-10 V analog output is connected to an analog signal processor module (model SRS 225) which performs a baseline correction to eliminate baseline fluctuations caused by residual low frequency noise and can provide a gain of 20 if necessary. The data is then digitized (12 bit A/D) on every shot by the laser interface and signal averaging is done digitally by the Apple computer.

To illustrate the sensitivity of the spectrometer, Fig. III.3 shows a vibrational spectrum of a static sample of N_2 at room temperature and a pressure of 2 Torr. Note from the inset of the S_8 line that the observed line profile is well fitted by a Gaussian lineshape with 285 MHz FWHM. The Gaussian shape is expected because the dominant broadening mechanism in this spectrum is Doppler broadening. For a pump probe crossing angle of 2° one calculates a Doppler width of 170 MHz as discussed in chapter II. Thus the difference of 115 MHz is a measure of the optical Stark broadening and the instrumental linewidth. From the data of Fig. III.3 it is possible to estimate how close the sensitivity of the system is to the theoretical limit imposed by the shot noise in the probe laser.

Shot noise is a fundamental noise source associated with the measurement of a rate of statistical events such as the arrival of photons at the detector. Since the laser power measurement is equivalent to a measurement of a number of photons n arriving during the measurement time τ one can use the Poisson statistic to calculate the uncertainty in n. The standard deviation for the Poisson statistic is equal to the square root of the mean value $\tilde{n}$. For a 200 mW probe laser at 514.5 nm and a 12 nsec boxcar window one calculates a maximum theoretical S/N ratio of $7.8 \cdot 10^4$ for a measurement of the laser power or, in other words, the fluctuations in the laser power due to the shot noise are $\cong 1.3 \cdot 10^{-5}$.

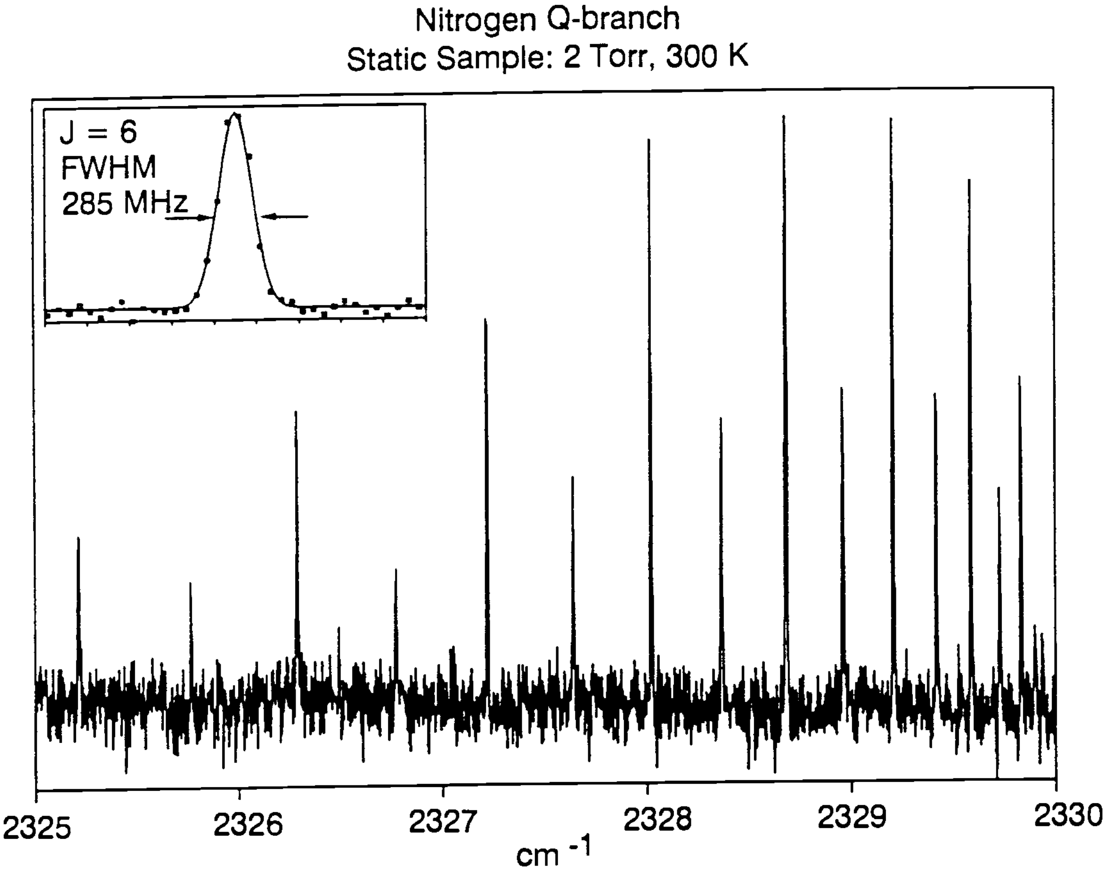

Figure III.3 Spectrum of static N_2 at 2 Torr.

To compare this value with the experiment we need to estimate the smallest intensity change in the probe laser that we can detect with a S/N of one. The peak signal for the J=6 line in Fig. III.3 was 3.65 V after amplification by $3\cdot10^4$. We calculate the relative absorption that produced this peak signal by dividing the unamplified signal voltage by the total DC signal voltage produced by the 200 mW in the photodiode:

$$\frac{\delta P}{P} \cong \frac{3.65\ \mathrm{V}}{30000\ 1.6\ \mathrm{V}} = 7.6\cdot10^{-5}$$

The rms signal to noise ratio in Fig. III.3 is about 30 and the moving exponential averaging used in this experiment resulted in a signal to noise improvement of a factor of $\sqrt{20}$. Converting to a S/N of 1 for a single shot measurement we estimate $1.1\cdot10^{-5}$ for the sensitivity limit, in accord with the theoretical value of $1.3\cdot10^{-5}$.

This result shows that the signal detection is in fact shot noise limited which means that other noise sources such as flicker noise in pump and probe laser and electronic noise are negligible compared to the shot noise. The only way to improve the S/N of the measurement is therefore to increase the probe laser power or the measurement time by averaging many shots. In this case the S/N will increase as $\sqrt{P\cdot\tau}$.

REPRESENTATIVE GAS PHASE SPECTRA

In order to document the performance of the spectrometer and to provide a basis for comparison with other instruments and techniques, several gas phase spectra are included in this chapter.

Fig. III.4 shows a spectrum of the N_2 Q-branch in air at room temperature and atmospheric pressure. The structure is due to vibrational rotational coupling, i.e. the fact that the molecule has a slightly larger average bond length in the first excited vibrational state than in the ground state. Since nitrogen has a nuclear spin of one the relative intensity of transitions originating in rotational levels with even and odd J is 2 and 1 respectively.

The first few transitions are not completely resolved because of pressure broadening. Comparison with Fig. III.5a shows that for a sample pressure of 100 Torr the pressure broadening is low enough that all the rotational transitions in the Q-branch of N_2 are completely resolved.

Fig. III.5b shows the Q-branch of CO at 100 Torr. No intensity alternation is observed because the molecule lacks the inversion symmetry. The pressure broadening coefficient for CO is larger since the nonzero dipole moment causes the molecules in CO to interact more strongly than in N_2.

In the O_2 Q-branch spectrum in Fig. III.5c all the transitions originating in levels with even J are missing because the oxygen atom has nuclear spin zero and the O_2 molecule has an odd electronic ground state.

Fig III.6 a and b show Q-branch spectra for C_2H_2 and HCN respectively. All the spectra were recorded with 3 shot averaging and 100 MHz intervals between datapoints. Typical pump energy is 5 mJ/pulse and the probe laser power is about 500 mW at the sample.

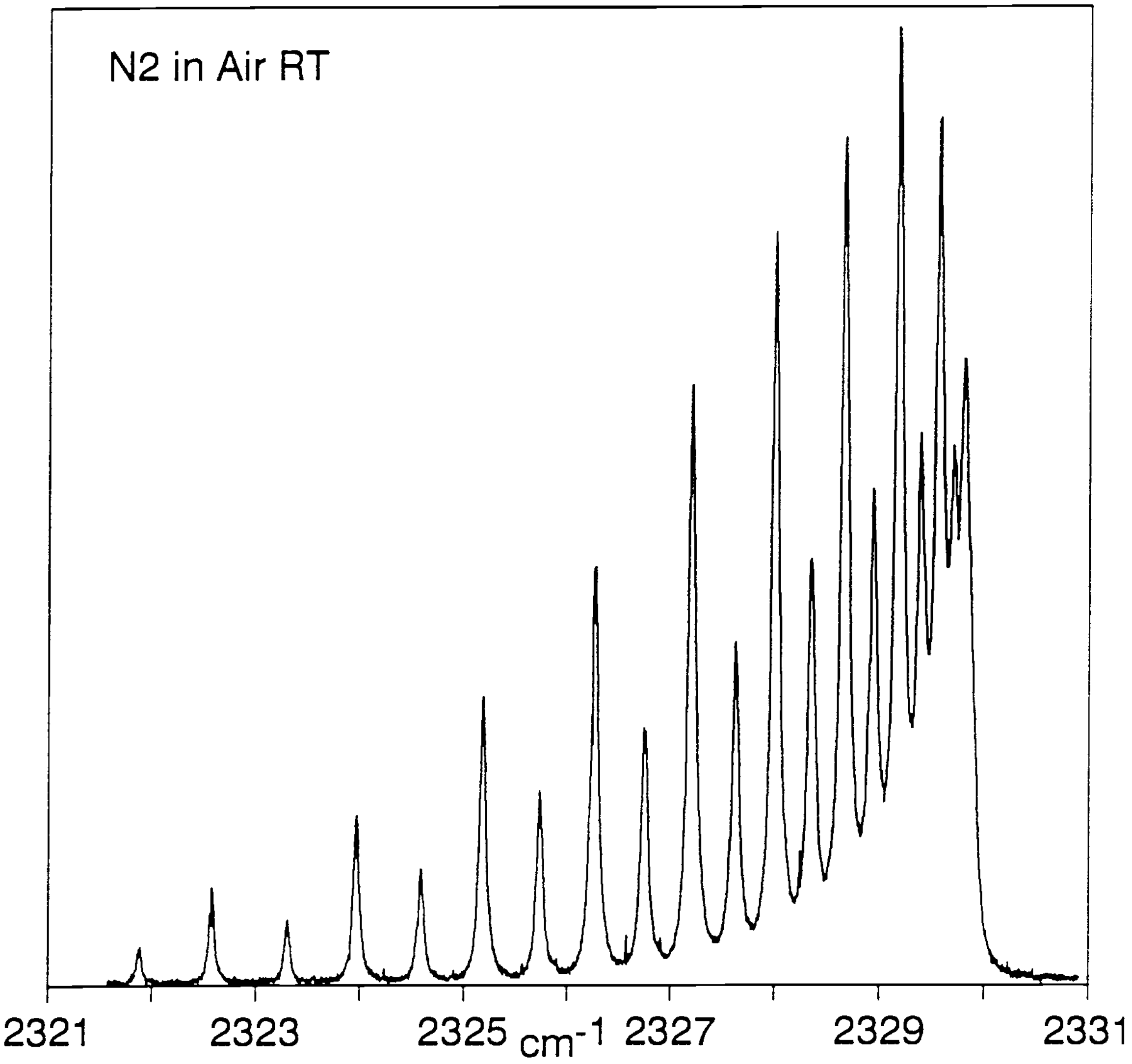

Figure III.4: SRS Q-branch spectrum of nitrogen in air at 1 atm and 295K. Scan conditions: 3 shots averaged, 200 MHz interval, 4 mJ/pulse pump energy.

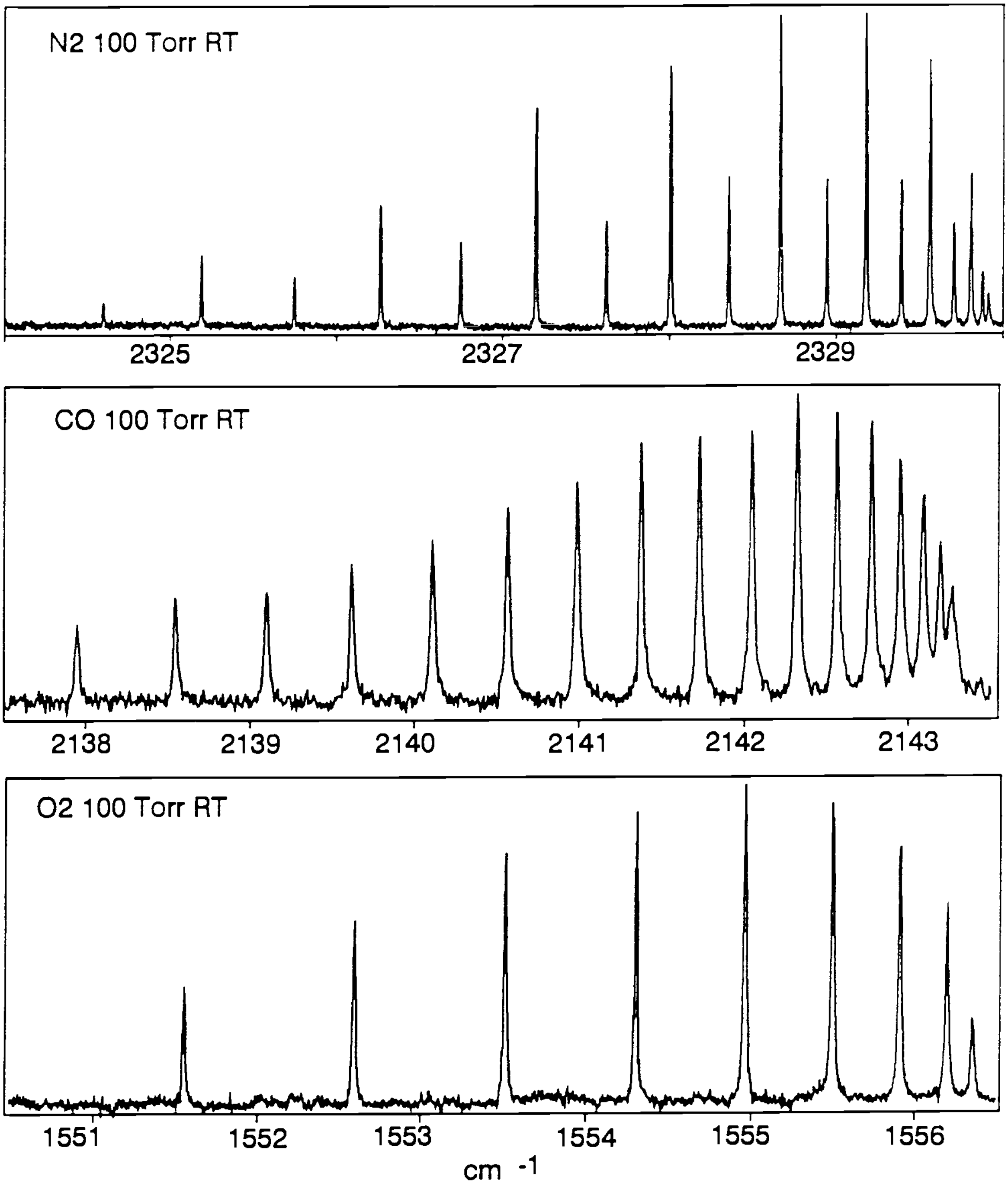

Figure III.5: SRS Q-branch spectra of N_2, CO, and O_2 at 100 Torr and 295K. Scan conditions: 3 shots averaged, 100 MHz interval, 5 mJ/pulse pump energy.

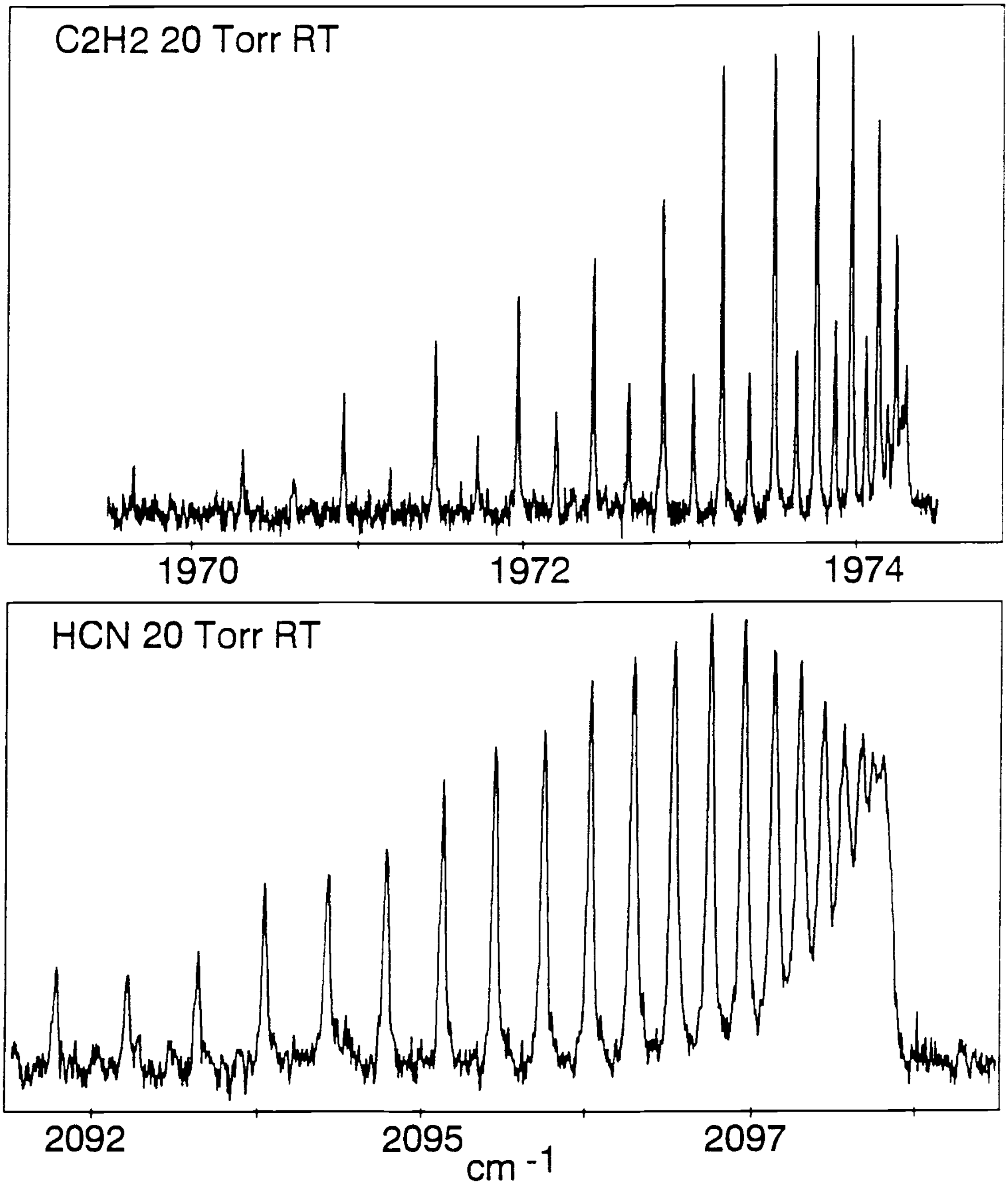

Figure III.6: SRS Q-branch spectra of C_2H_2 and HCN at 20 Torr and 295K. Scan conditions: 3 shots averaged, 100 MHz interval, and 5 mJ/pulse pump energy.

CHAPTER IV: LOW SHIFT STIMULATED RAMAN SPECTROSCOPY

INTRODUCTION

High resolution rotational Raman spectroscopy provides valuable structural information for nonpolar and other molecules not easily examined by microwave techniques. The use of SRS is especially appealing in this regard since the technique combines high resolution with high sensitivity, thus allowing studies at low pressure where collisional broadening is reduced. This makes it possible to obtain resolved rotational Raman spectra even for heavier molecules for which spontaneous Raman spectroscopy could only show the overall band contour. SRS also allows for very good stray light rejection since the signal is contained in a laser beam and can be spatially separated from the pump light. Finally, the use of well defined beams, crossed at a small angle, provides good spatial resolution which is advantageous for point probing in free jet expansion.

For these reasons the SRS spectrometer was modified to cover the region of low frequency shifts (500 - 0 cm^{-1}) as well as the usual range of Raman shifts (4700 - 500 cm^{-1}). A description of the modifications necessary to meet the more stringent stray light rejection requirement is given in the following section.

LOW SHIFT SRS SPECTROMETER

One of the requirements on the spectrometer was that it should be easily converted to cover the widest range of Raman shifts. The scan range of the ring laser with R590 as the laser dye is approximately

568 - 617 nm. This range can be shifted by using different laser dyes, but dye changes and the associated realignment of the ring laser are time consuming and the output power as well as the lifetime are lower for any other dye than R590. Therefore the choice was to use only R590 in the ring laser and to line tune the Raman shifts in large steps by using different ion laser lines for the probe light.

The only ion laser line in the gain region of R590 is the yellow line of the krypton ion laser at 568.2 nm which made it necessary to add a krypton ion laser to the SRS spectrometer. Besides finding a suitable light source, the main problem in rotational Raman spectroscopy is the separation of the Raman signal from the powerful pump light. Since the frequency shifts are very small several methods are combined in the experimental setup to provide the highest possible selectivity. These are:

- Polarization selection: one can make use of the fact that rotational Raman lines are depolarized and cross the polarization of pump and probe laser. A polaroid filter can then be used to reject scattered pump light.
- Spatial filtering: since there is no phase matching requirement for SRS one can cross pump and probe beams to spatially separate them at the detector.
- Spectral filtering: further selectivity is achieved through the use of a concave holographic diffraction grating with high dispersion (2400 groves/mm).

Fig IV.1 through IV.3 show several representative rotational spectra which will be used to characterize the spectrometer and discuss some of the aspects relevant to rotational SRS. Fig. IV.1 shows a rotational spectrum of air at room temperature and atmospheric pressure. The spectrum consists of more than 10^4 datapoints and shows that the SRS spectrometer can take data at very high resolution (100 MHz) over large scan ranges because of the integrated wavemeter. The calculated line position for the N_2 and O_2 lines are also shown.

Due to the low Raman shift Doppler broadening is negligible in rotational spectra compared to pressure broadening and the instrumental lineshape. Fig. IV.2 shows the S8 line of N_2 at different sample pressures together with calculated Lorentzian line profiles determined from a least squares fit to the data. For the higher pressures the linewidth is seen to decrease due to the decrease in collisional broadening, but at low pressure (14 and 3 Torr) a larger linewidth than expected from collisional and Doppler broadening is observed. This is due to the optical Stark broadening which was first observed by Farrow and Rahn[52] and is discussed in the chapter on experimental lineshape effects. The optical Stark effect can be reduced at the expense of sensitivity if the power density at the beam focus is lowered by lowering the pulse energy or by weaker focusing of the beams. It can be seen in Fig. IV.2 that the signal to the noise ratio for a high resolution technique such as SRS does not scale with sample density as long as the instrumental linewidth is small compared to the sample linewidth. Therefore one doesn't sacrifice signal to noise ratio by using low pressure samples to record resolved Raman spectra.

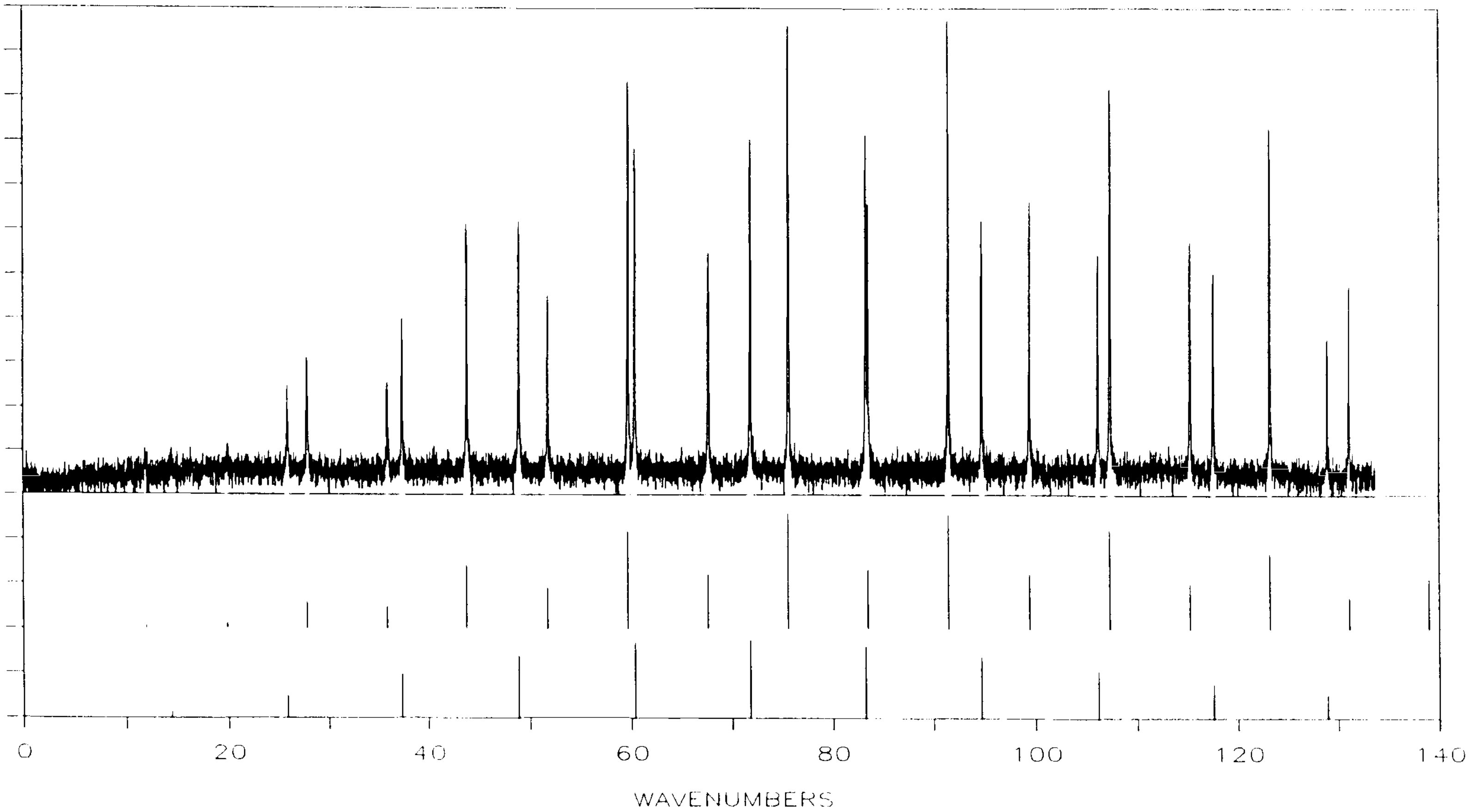

Figure IV.1: Pure rotational SRS spectrum of Air at 1 atm. and 295 K. Line positions for N_2 and O_2 transitions are indicated at the bottom. Scan conditions: 200 MHz interval, 3 shots averaged, 5 mJ pump laser power.

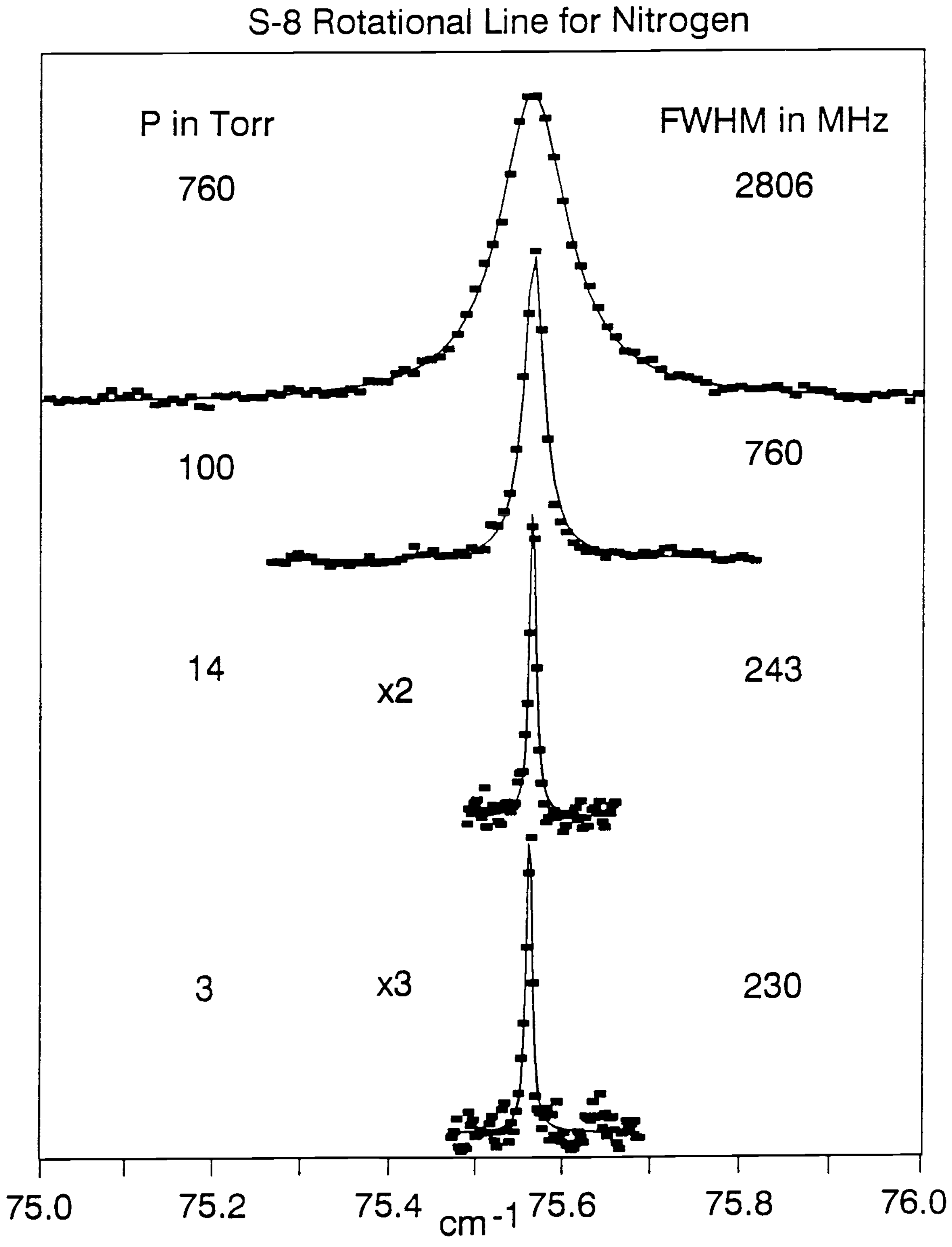

Figure IV.2: S_8 pure rotational Raman transition ($J'' = 8 \rightarrow J' = 10$) in N_2 for different sample pressures. The solid line is a Lorentzian profile fitted to the data by a least squares fit. At low pressure (3 Torr) the linewidth becomes limited due to the optical Stark effect.

ROTATIONAL RAMAN SPECTRUM OF DICYANOACETYLENE

The first research application of the low frequency SRS spectrometer was a study of the rotational spectrum of C_4N_2. This molecule is a photoreactive species that readily undergoes polymerization which complicates optical spectroscopy but makes the molecule interesting as a precursor for polyacetylenes. The vibrational spectrum of C_4N_2 has been reexamined recently[67], stimulated by the detection of similar nitriles in the thermal emission spectrum of the atmosphere of Titan, one of the moons of Saturn[68]. However, no rotational constants for the gas phase have been reported in the literature. This is in part due to the fact that the C_4N_2 has many low frequency vibrational states which are all significantly populated at room temperature leading to a very congested spectrum because of hotband transitions. Other reasons why gas phase spectroscopy is difficult for C_4N_2 are the low vapor pressure (50 Torr at 300K) and its photoreactivity. More details about the preparation and a combined spectroscopy - electron-diffraction study of C_4N_2 can be found in the paper by Kirk Brown et. al[69].

Fig. IV.3 shows the pure rotational spectrum of C_4N_2 which was recorded with the SRS spectrometer. By fitting a calculated spectrum to the observed peak maxima one obtains average B and D values for all populated states:

$$B_{aV} = 0.044867(19)\ \mathrm{cm}^{-1} \quad \text{and} \quad D_{aV} = 9.3(6)\cdot 10^{-9}\ \mathrm{cm}^{-1}$$

An expansion of the Raman loss spectrum shows hints of some regular but poorly resolved structure within each rotational transition. An attempt was made to extract more information from the data by using a simple model to simulate the spectrum. This was done by calculating the frequencies and intensities of the rotational transitions arising from the ground vibrational state and all states below 600 cm^{-1} which involve two bending modes, ν_7 and ν_9, only. A single value for the vibrational rotational coupling constant α was assumed for all excited states. Fig. IV.4 shows the contours calculated for low and high J values for several values of α together with the experimental data. It can be seen that an average α value of about -0.0002(1) gives the best overall fit which in turn gives B-value for the ground vibrational state of B_0 = 0.0445(1) cm^{-1}. These values agree well with values that were calculated from bond distances of C_4N_2 in the solid phase determined by x-ray diffraction. A more complete discussion and comparison with the ED structure results is given by Brown et. al. in reference 69.

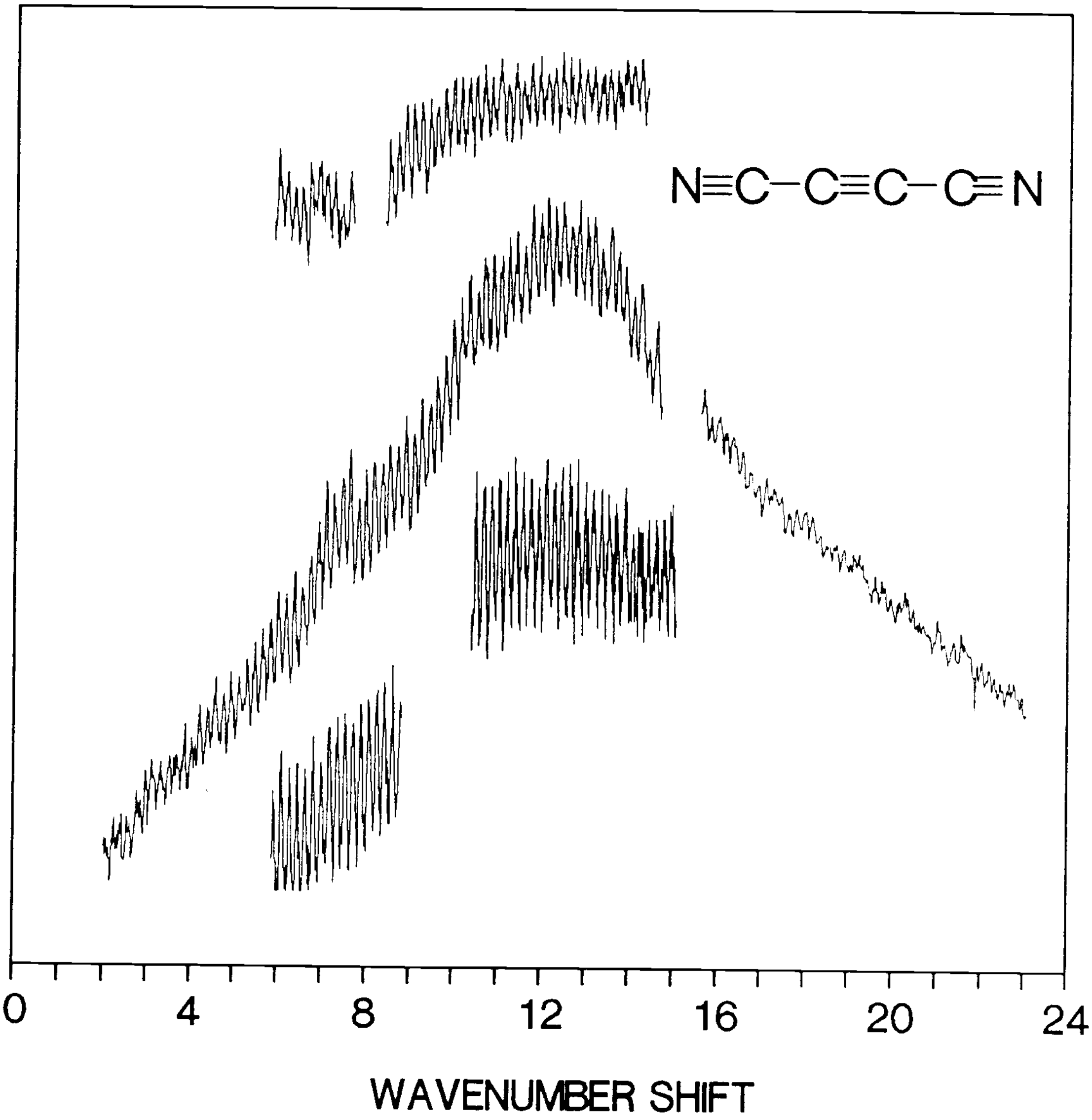

Figure IV.3 : Pure rotational Raman spectrum of C_4N_2.
Because the sample polymerizes in the laser beams the spectrum could not be recorded in one continuous scan. After a few minutes a brown fog would form that strongly attenuated the laser beams. The scan had to be stopped and the sample was purified by a freeze-thaw cycle. Several partial scans that were recorded in this way are shown in the figure. Scan conditions: 2 mJ pump laser power, 300 MHz interval, 10 shots averaged.

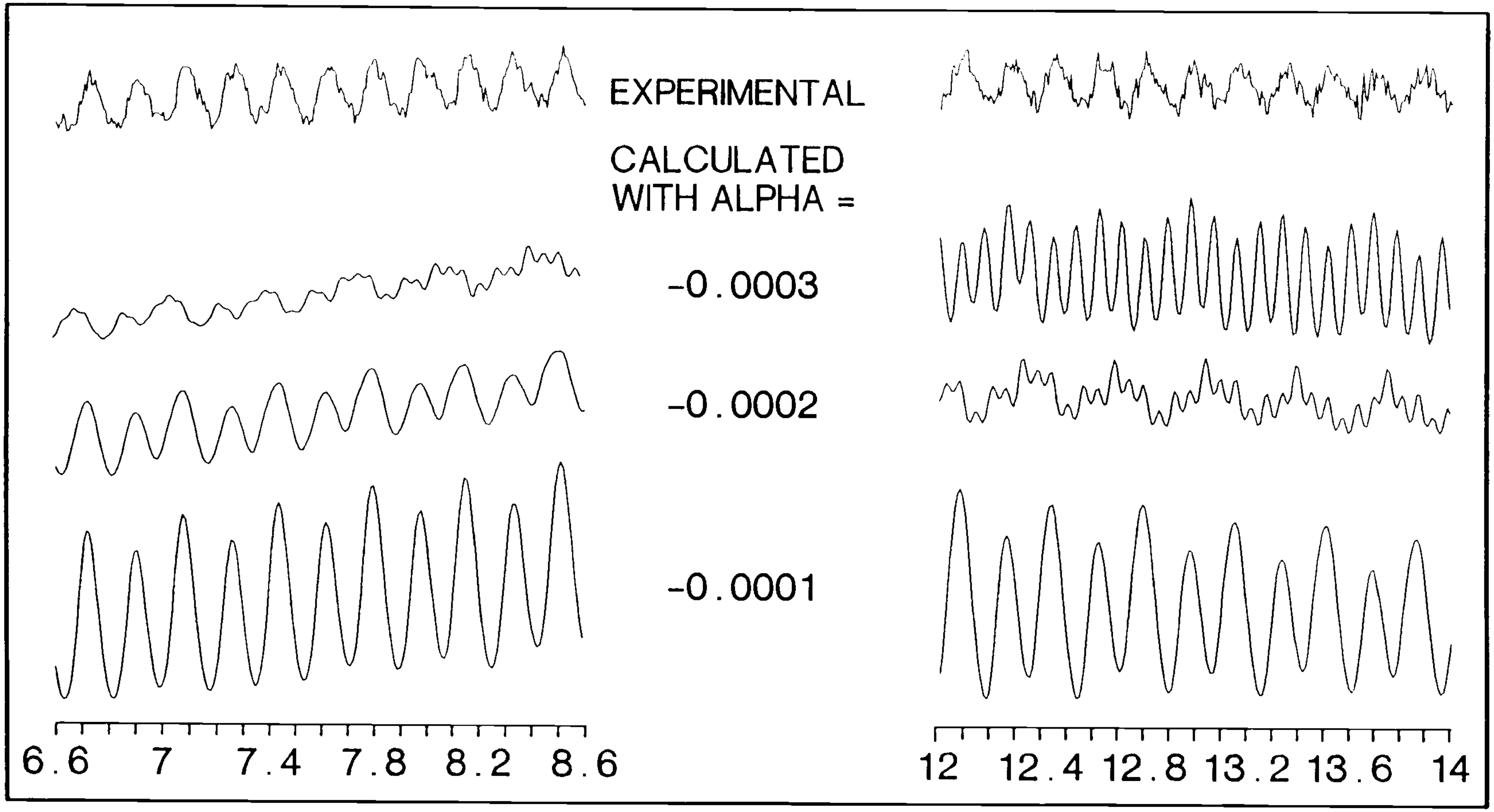

Figure IV.4: Comparison of experimental spectrum of C_4N_2 with simulated spectra for different values of the rotation-vibration coupling constant α. The same value for α was assumed for all low frequency bending modes

CHAPTER V: HIGH RESOLUTION SRS IN CONDENSED PHASES

INTRODUCTION

The vibrational frequency in condensed phases is shifted relative to the gas phase value due to the forces from the surroundings on the molecular bond. For a diatomic the net force is along the molecular axis. Attractive force will cause a decrease in the vibrational frequency whereas repulsive forces will lead to an increase. Raman linewidth in condensed phase samples also contain information on the intermolecular interactions since the "bath" surrounding the oscillator will dephase the coherently excited vibration which causes line broadening. The effects of the intermolecular potential on the vibrational Raman line make Raman spectroscopy a useful probe for the investigations of intermolecular forces and dynamics in condensed phases.

A large number of experimental and theoretical studies that are concerned with the density and temperature dependence of Raman lines in condensed phases have appeared in the recent literature[70-72]. Usually spectroscopy is done at relatively low resolution since the observed lines are broad due to short vibrational lifetimes and thermal broadening. However, the simplest molecular liquids and solids such as N_2, O_2, CO_2, CS_2 show very sharp lines for their intramolecular vibrations since the vibrational lifetimes can be very long and the coupling to phonons is weak. In these cases a high resolution technique is necessary to make accurate lineshape measurements. The Raman spectra of condensed molecular phases have been recorded in many cases using conventional Raman spectroscopy[73]. Narrow widths were noted but in most cases the observed linewidth was still limited by the instrumental resolution[74]. Several groups[75,76] have used a monochromator-interferometer combination to increase the resolution and observe linewidths characteristic of the sample and not the instrument. In the past high resolution SRS has not been used to make accurate measurement of vibrational linewidths probably due to the increased complexity and cost of this nonlinear technique compared to conventional Raman spectroscopy. There are several advantages that SRS can offer over conventional Raman spectroscopy which might well justify the additional effort:

- very high resolution (cw 0.0003 cm^{-1}, quasi-cw 0.003 cm^{-1}) without loss of sensitivity.
- signal is generated in a very small volume; no large single crystals are needed
- good control over polarization of beams allows more accurate measurement of depolarization ratios than with spontaneous Raman methods
- calibration of Raman shift is done by measuring two narrow laser frequencies which can be done more accurately than a frequency measurement in a dispersed conventional Raman spectrum.

Another nonlinear Raman technique (CARS) has already been used to study condensed phases under high spectral resolution[42]. However, SRS can offer some advantages over CARS as well:

- no phase-matching requirement: temperature, pressure and phase transitions do not affect the signal through the phase-matching of the laser beams as in the case of CARS.

- SRS samples only Im($\chi^{(3)}$): no contribution from the (purely real) nonresonant part of $\chi^{(3)}$ of sample and windows and no interference from nearby resonances. For CARS these distort the lineshapes and complicates the analysis.

The following section describes the necessary modifications of the SRS spectrometer and the first applications of high resolution SRS to condensed phases.

EXPERIMENTAL TECHNIQUES

Two different detection techniques were used in the condensed phase SRS experiments. In neat samples the signal is strong enough that it can be detected with the CW-SRS technique which has the advantage of higher resolution (0.0003 cm^{-1}) and is simpler experimentally since the output of the ring laser is used directly without pulse amplification. However, the quasi-cw technique is more sensitive and the small loss in resolution is only critical in the very sharpest lines that were measured. Therefore the latter technique was used in experiments where high sensitivity was needed as, for example, in measurements on matrix isolated samples.

CW-SRS

In the cw setup the output of the ring dye laser was amplitude modulated at 100 KHz with an acousto-optic modulator. The modulation is accomplished by the acousto optic effect, in which the incident light meets a standing ultrasonic wave in a glass block at Braggs angle. This results in the incident light being diffracted in one principal order. The 40 MHz carrier wave that produces the standing sound wave can be modulated by an external signal which in our experiment is a 100 KHz square wave. The diffracted beam is blocked by a knife edge and the undiffracted beam, now modulated at 100 KHz with a 80% modulation depths, is used as the pump light in the SRS experiment. The beams were focused with 200 mm lenses resulting in a measured spot size of 20 μm at the focus.

Signal detection is done with the same photodiode (EG&G FND 100) as in the pulsed experiments but the incident cw power has to be limited to 15 mW to avoid detector damage. The signal is then sent to a lock-in amplifier (ORTEC model 9501 E) where it is amplified, demodulated and filtered before it is digitized by the data collection interface. The sensitivity was sufficient to detect the SRS signal of liquid N_2 using 300 mW pump and 15 mW probe power with a S/N of 200 while scanning with a time constant of 1 sec.

Quasi-CW SRS

Basically the same setup was used for the quasi-cw detection of Raman spectra in condensed phase samples as described previously in the section on gas phase SRS. The pump laser light was the output of the pulse amplifier seeded by the ring dye laser. The laser beams were focused to 200 μm spot size and crossed in the sample at a small angle (≅ 2 degrees) to allow for spatial separation of pump and probe light. The pump energy per pulse was 20 μJ for neat samples which is a factor of 500 lower than in the gas phase spectra. Higher pulse energy was used only in the experiments that detected the isotopic impurity $^{15}N^{14}N$ in N_2 and in the scans of matrix isolated samples (N_2 in Ar, CO in N_2). It was found that pulse energies of up to 1 mJ/pulse could be used without sample damage and still higher pulse can be used if the beams are focused less tightly.

Sample Preparation

Thin Film Samples

Initially samples were prepared as thin films by spraying the gas onto a sapphire window cooled by a closed cycle helium refrigerator (AIR PRODUCTS DISPLEX 202). This allowed the preparation of solid samples at low temperatures where the vapor pressure of the sample is insignificant. If the temperature was raised to the point where the vapor pressure becomes about 10^{-3} Torr conductive heat transfer from the surroundings was larger than the cooling capacity of the Displex causing the temperature to rise quickly and the sample to be pumped off by the vacuum system.

Cryogenic Sample Cell

In order to be able to vary the temperature over the whole liquid and solid range a special, closed sample cell was built which can be cooled by the Displex refrigerator. The body of the cell is machined from high conductivity copper. Indium is used to give a vacuum tight seal between the sapphire windows and the cell body. Sapphire is used as the window material because of its high strength and high heat conductivity even at low temperature which avoids thermal gradients and stress. One disadvantage is the fact that sapphire is optically anisotropic which means that it will partly depolarize a linearly polarized beam unless the direction of propagation is along the optical axis. The sapphire cell windows used in the experiments had arbitrary direction of the optical axis which made measurements of the depolarization ratio uncertain. Therefore measurements of the depolarization ratio were done with thin films deposited on the outside of the window. Windows that are cut perpendicular to the optical axis and therefore will not depolarize the beams are commercially available at a higher price and could be added at a later stage.

The samples were transferred into the cell through a stainless steel capillary tube by condensing the gas in the cell just below the boiling point. After sufficient liquid had formed in the cell the temperature was lowered to the freezing point and the sample was frozen very slowly to avoid cracking as much as possible.

The temperature was monitored by a Au-Fe vs. chromel thermocouple attached to the cell body. The thermocouple voltage is also used by a temperature controller (SCIENTIFIC INSTRUMENTS INC. MODEL 3700) to control the sample temperature through a button heater attached to the last stage of the Displex unit. In this way the temperature can be controlled to 0.2 K and read with an accuracy of 0.5 K. The calibration of the thermocouple was checked by measuring the vapor pressure of the sample as well as by observing the phase transitions in N_2 and O_2 occurring at known temperatures.

VIBRATIONAL RAMAN SPECTRUM OF CONDENSED NITROGEN

We have measured the Raman spectrum of nitrogen in its condensed phases for several reasons. The initial motivation was to obtain accurate data for the vibrational frequency and linewidth as a function of temperature for comparison with SRS studies of N_2 aggregation in free jet expansions. This work will be described in the following chapter. The other reason for the work described in this chapter was to establish the value of the high resolution SRS technique for very accurate Raman spectroscopy in condensed phases. Nitrogen is a good test case because of its narrow linewidth and because of the large amount of data that is available from other Raman techniques which can be used for comparison.

Fig. V.I shows spectra of the Raman Q-branch of N_2 for the liquid phase, the β-phase, and the α-phase. This is the first study, to our knowledge, in which the spectral changes in all three phases, including the phase transitions, were recorded along the coexistence curve between the vapor and the condensed phases.

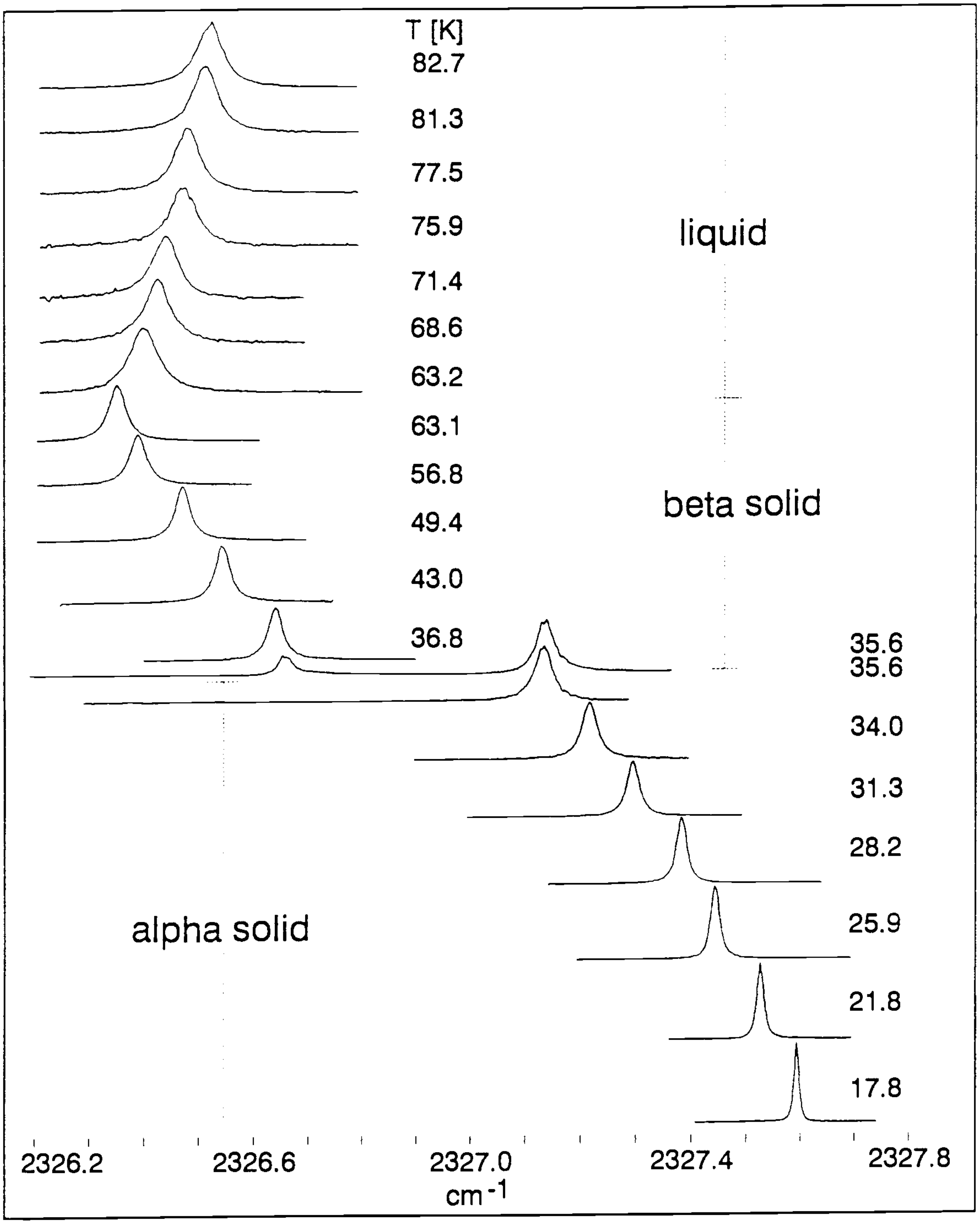

Figure V.1 : CW-SRS spectra of the internal vibration of nitrogen in its condensed phases. The sample was in equilibrium with its vapor at each of the indicated temperatures. Scan conditions: 50 MHz resolution, 300 mW pump laser power, 15 mW probe laser power at the detector, 1 sec time constant.

Liquid Nitrogen

Linewidth

The vibrational Raman line in liquid N_2 is well described by a Lorentzian line profile (see Fig. V.2). It is well known that energy relaxation is exceedingly slow in liquid nitrogen (T_1 about 60 sec) and that the Raman lineshape is due to vibrational dephasing. Time resolved CARS measurements by Lauberau[77] have shown an exponential decay with a decay time T_2 of 75 ± 8 psec in good agreement with a T_2 time calculated from our linewidth data and other results reported in the literature. Table V.I shows a comparison of our results with literature values.

Table V.1: Vibrational Frequency and Linewidth for Liquid Nitrogen

$\tilde{\nu}$	$\Delta\tilde{\nu}_{FWHM}$	T [K]	ref.		technique
2331	0.066(6)	77	Scotto[76]	1968	conv. Raman
-	0.0534(60)	77	Clouter[40]	1977	conv. Raman
-	0.071(6)	77	Lauberau[77]	1977	time res. CARS
2326.5	0.058(2)	78	Akmanov[42]	1980	CARS
-	0.0565(60)	76.2	Van Voorst[41]	1986	conv. Raman
2326.515(2)	0.0561(10)	77.4	this work[80]	1989	cw-SRS

We observe that the linewidth in liquid N_2 decreases with decreasing temperature from 110 K to 85 K, but then remains approximately constant until it rises slightly just before the triple point (see Fig.V.3). This confirms the findings of a recent Raman study[41] but earlier experiments did not detect this rise in linewidth at the triple point presumably because of the lower resolution of these experiments. It was noted in reference 41 that simple theories of vibrational dephasing based on interaction through repulsive forces predict an increase in the linewidth with decreasing temperature. However, a more realistic model[39] shows that the attractive forces and vibration-rotation coupling can cause a decrease in linewidth with decreasing temperature. The observed temperature dependence of the linewidth can therefore be explained by the changes in the relative contributions of the repulsive and attractive forces and the vibration rotation coupling and our data indicates that the balance point occurs at about 85 K for nitrogen.

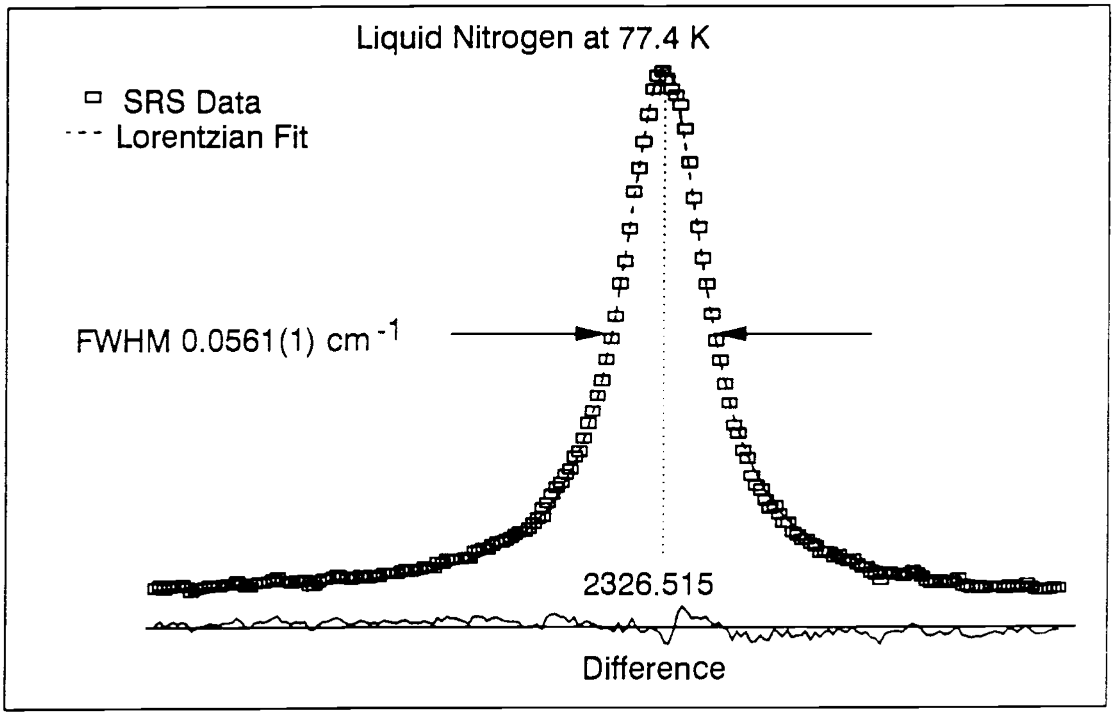

Figure V.2: SRS spectrum of Q-branch line in liquid nitrogen at 77.4 K. Scan conditions: 75 MHz Resolution, 300 mW pump laser power, 15 mW probe laser power, 1 sec time constant. The dashed line is a least squares fit of a Lorentzian line profile.

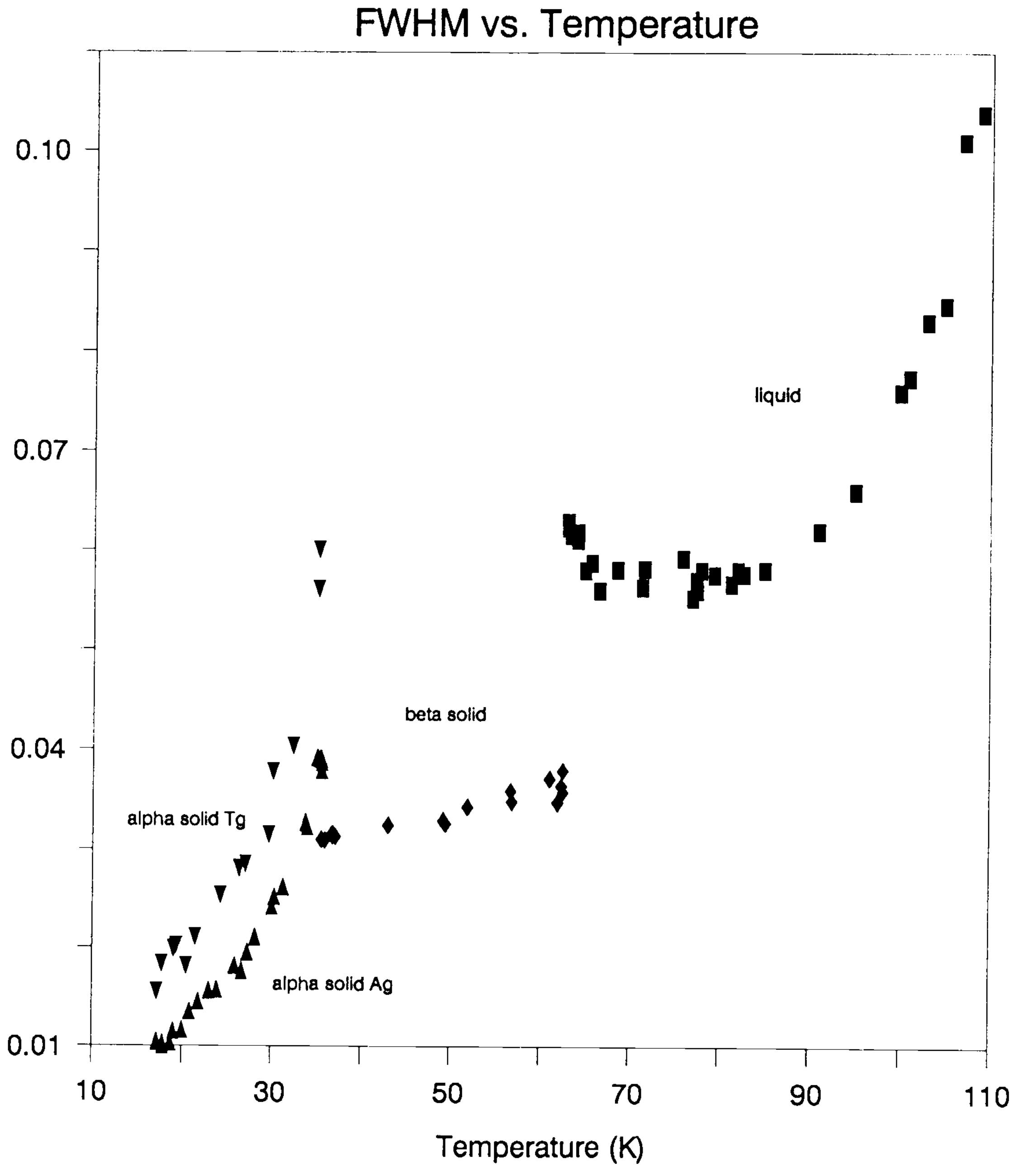

Figure V.3: Temperature dependence of the linewidth (FWHM) of the vibrational Q-branch transition in the condensed phases of nitrogen. The sample was in equilibrium with its vapor at all temperatures.

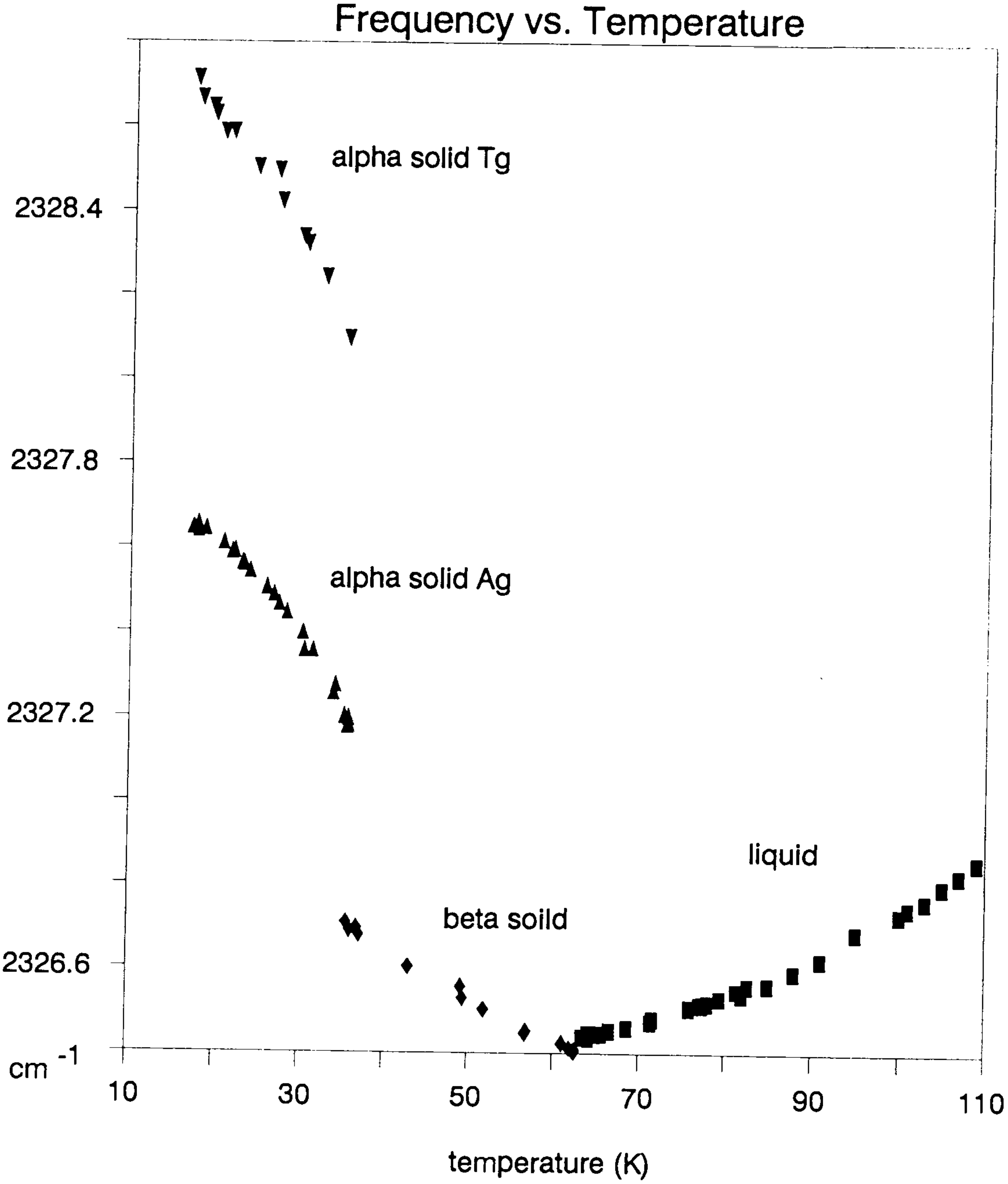

Figure V.4: Temperature dependence of the vibrational Raman frequency in the condensed phases of nitrogen.

Frequency Shifts

The vibrational frequency in liquid nitrogen at 77.4 K is red shifted by 3.55 cm^{-1} compared to the gas phase. This implies that the attractive forces on the molecular bond dominate in the liquid. Our measurements show that the vibrational frequency further decreases with decreasing temperature (see Fig. V.4), but at a rate that decreases as the triple point is approached. This temperature shift of the line is mainly an effect of the density change and it is known[78] that the pure temperature dependence (at constant density) of the Raman frequency is negligible in the case of N_2. High pressure Raman experiments[17] show that at densities higher than at the triple point the vibrational frequency will increase with density and eventually, at very high pressure ($2 \cdot 10^4$ atm), reach values that are several cm^{-1} above the gas phase frequency of 2330 cm^{-1}.

Solid β Nitrogen

Liquid nitrogen in equilibrium with its vapor freezes at the triple point (63.15 K) to form the orientationally disordered β-phase of solid nitrogen. One can see in Fig. V.I that the frequency shifts only slightly to the red by 0.05 cm^{-1} but the linewidth narrows by about a factor of two. This is not surprising since dephasing by elastic collisions should be strongly reduced or absent because the molecules are on fixed positions in the lattice. It is very interesting however that the shift of the vibrational frequency with temperature reverses its direction compared to the liquid. The lineshape in the β-phase is also, just like in the liquid, well represented by a Lorentzian. Clouter and Kiefte[78] have observed this very narrow width and speculated that it is caused by a motional narrowing effect due to the precession motion of the N_2 molecules on their lattice sites. This might be supported by our observation that the linewidth of β-N_2 hardly changes with temperature.

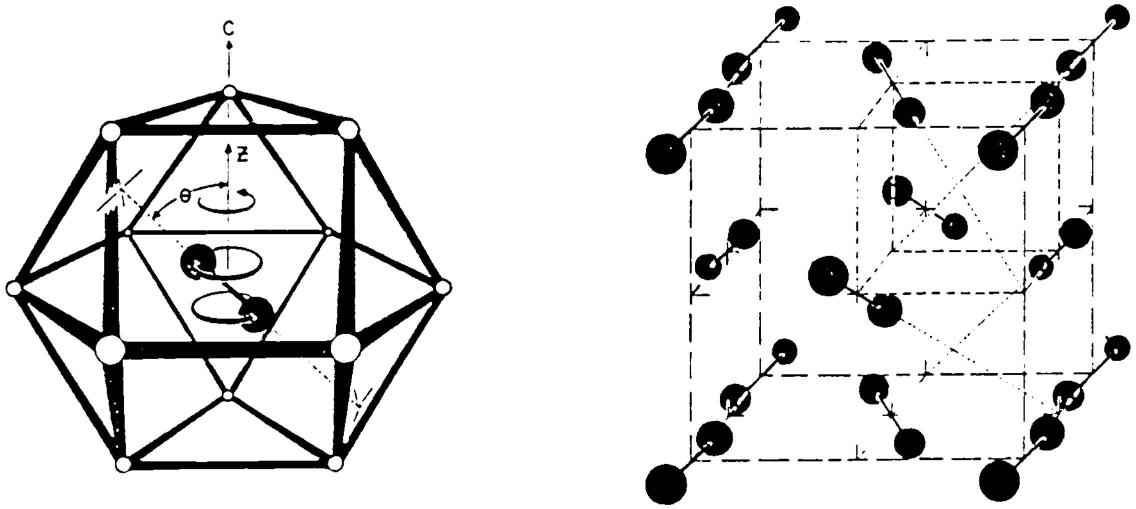

Figure V.5: Crystal structures for solid nitrogen from ref (79a)
Left: orientationally disordered β-phase, hcp structure with 2 molecules per unit cell, stable between 63.1 and 35.6 K.
Right: ordered α-phase with cubic structure and 4 molecules per unit cell. The N_2 units are oriented along the body diagonals of the unit cell. Stable below 35.6 K.

Solid α Nitrogen

The $\beta \rightarrow \alpha$ phase transition causes a 0.6 cm^{-1} shift to higher frequency. The line splits into two Davydov components (A_g and T_g) due to the interaction between the 4 molecules per unit cell. The linewidth increases in the phase transition, presumably because the motional narrowing is lost as quadrupole-quadrupole interactions "lock" the N_2 units into ordered positions in the α-N_2 crystal. The linewidth shows a much stronger temperature dependence than in the β phase as seen in Fig. V.3. In addition to the decrease in linewidth the lineshape becomes increasingly non-Lorentzian and is better described by a Voigt profile at low temperatures.

Davydov Splitting in α Nitrogen

Fig.V.6 shows the vibron band for α nitrogen at 15 K. These are the first Raman spectra reported in the literature[80] in which the two Davydov components (A_g and T_g) are completely resolved and well-separated. The vibrational frequencies that we determined with the SRS spectrometer have an uncertainty of 0.007 cm^{-1} and are considerably more accurate than previous Raman values, summarized in reference 73, which ranged from 2326 to 2329 cm^{-1}. By recording spectra with parallel and crossed polarizations of pump and probe beams, the different symmetry character of the two components is clearly demonstrated. For parallel polarizations, the measured ratio $I(A_g)/I(T_g)$ is 9.2. Theoretical estimates using a simple oriented gas model predict a ratio of $\frac{45}{4}\left(\frac{\gamma}{\alpha}\right)^2$ and thus we deduce a value of 0.90 for $\frac{\gamma}{\alpha}$, the ratio of the anisotropic and isotropic polarizability derivatives. The close agreement with a corresponding value of 0.89 from the gas-phase Q-branch depolarization ratio[81] is consistent with the expectation that the intermolecular interactions in the crystal are weak and unlikely to affect the polarizability constants of N_2.

The accurate A_g, T_g frequency values of N_2 can serve as useful tests of theoretical models of the intermolecular potential of nitrogen. For example, using six different intermolecular potentials, Thiery and Chandrasekharan[82] have reported values for the Davydov splitting and the gas to solid frequency shifts using the "vibron model" developed by Zumhofen and Dressler[82]. As seen in Table V.2, our experimental results clearly favor one of the potentials (designated KE' in (82)), whereas previous experimental data had much larger uncertainty which covered the range of values predicted by several potentials. Variations in the splitting and shifts as temperature and phase changes occur could provide additional constraints on such models.

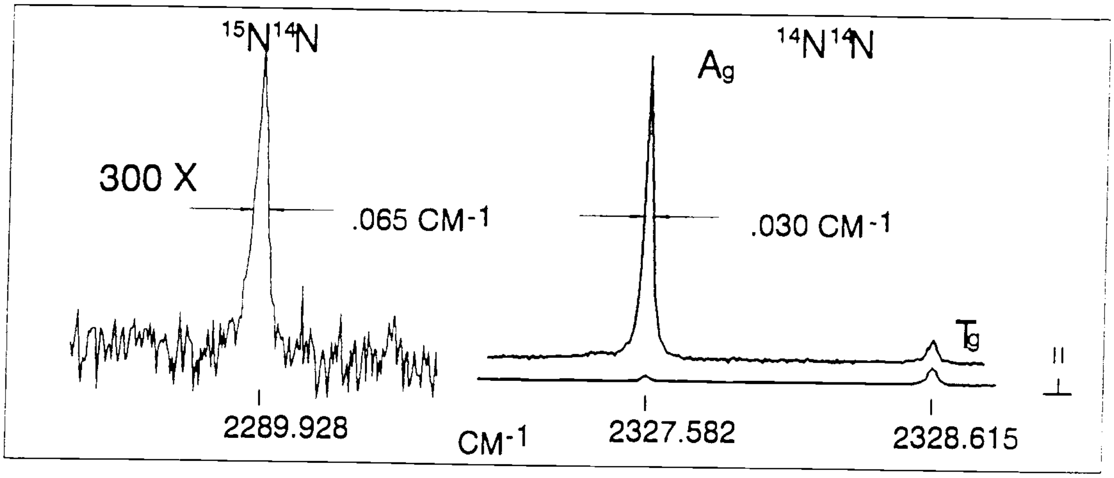

Fig. V.6: Davydov splitting in α-N_2 at 15 K. Also shown is the line due to the $^{15}N^{14}N$ isotopic impurity present at 0.7 % abundance.

Table V.2: Calculated and Observed Vibron Frequencies in α-Nitrogen

Theoretical^a

Potential	$\nu_{gas} - \nu_{Ag}$	$\nu_{Tg} - \nu_{Ag}$
LP	-5.107	1.963
LE	-5.686	1.728
LE'	-5.037	1.614
KP	-2.369	1.456
KE	-2.948	1.221
KE'	-2.298	1.106

Experimental

T (K)	$\nu_{gas} - \nu_{Ag}$	$\nu_{Tg} - \nu_{Ag}$
18^b	-3.9(20)	1.2
4.2^c	-2.1(8)	1.00(5)
15^d	-2.300(7)	1.033(2)

a) ref. (82) A detailed description of each potential is given this reference.
b) ref. (83)
c) ref. (84)
d) this work

Effect of Crystal Quality on the Raman Line

There is significant interest in high resolution lineshape measurements at very low temperature because, in the absence of thermal broadening, disorder in the crystal structure and isotopic impurities can determine the observed lineprofiles. Thermal broadening is expected to produce a Lorentzian lineshape. Such was observed at higher temperatures but at 15 K, which is the lower temperature limit of the cooling arrangement in our experiments, the measured lineshape for α-N_2 clearly starts to deviate from a Lorentzian shape.

In an effort to determine the origin of this inhomogeneous broadening we studied the lineshape of α-N_2 at 15 K and found that the observed linewidth and shape depend on the sample quality. Generally we measured larger widths for the thin film samples, prepared by vapor deposition without annealing, than for the bulk samples. Since the bulk samples were prepared by freezing the liquid at the triple point and slowly cooling through the β-phase the crystal quality in the bulk samples is expected to be better than in the thin film samples. To further investigate how the line depends on the sample quality several spectra were taken at the lowest possible temperature (15 K) at different position in the sample. To obtain a measure for the crystal quality the sample transmission was determined for each position. Since solid nitrogen does not absorb visible light the sample transmission is reduced only by scattering due to microcracks and other crystal imperfections. Fig. V.7 shows four different sample qualities. In the clearest sample (top) the line is very narrow and highly symmetric. A disordered sample gives an asymmetric line where the degree of disorder correlates with the asymmetry but the direction of the asymmetry was different in different samples. The reason for the latter is not known but may be significant, as discussed below.

These measurements are, to our knowledge, the first high resolution measurements on α-nitrogen. It is interesting to compare our results with those of time resolved experiments reported in the literature. For N_2 in the range 1.33 to 4.2 K, Abram et al.[50] have used time-resolved CARS to observe a temperature-independent but strongly nonexponential decay of the vibrational coherence. The decay time increased from less than 1 nsec initially to 14.5 nsec in the first 100 nsec of the decay. To explain this type of decay, they used the lineshape model for disordered crystals developed by Klafter and

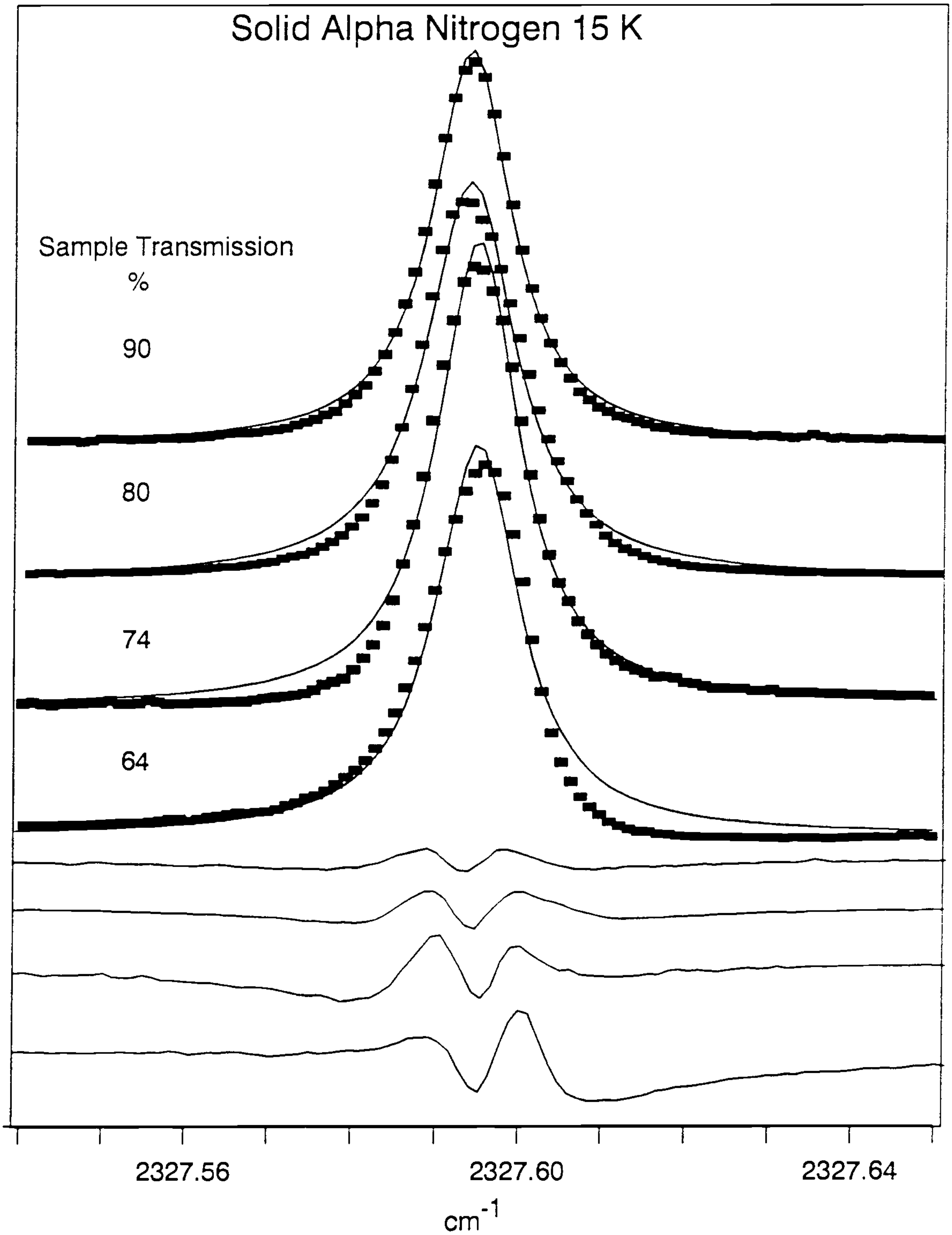

Figure V.7: Effect of crystal quality on the lineshape. The four spectra were taken at different positions in the sample. The sample transmission serves as a measure of crystal quality. Solid lines are a Lorentzian fit to the data. The difference between the calculated Lorentzian profile and the experimental data is shown at the bottom.

Jortner[49], which was briefly described in chapter II. This theory predicts an asymmetric lineshape for the A_g mode of α-N_2 since the vibron bandwidth W ($\cong$ 1 cm^{-1}) is much larger than the width σ ($\cong$ 0.065 cm^{-1}) of the distribution of site energies characterizing the disorder in the crystal and since the A_g mode is located near a singularity of the vibron band[50]. Abram et al.[50] used this predicted asymmetry in the frequency domain to explain the observed nonexponential time decay. This is possible because a Fourier transformation relates the frequency to the time domain.

One could speculate that the asymmetry seen in Fig. V.6 is the first observation of the microscopic disorder effect in the frequency domain which would confirm the assumption that Klafter and Jortner's model applies to α-N_2. However, the fact that the asymmetry reverses in some samples (only in the ones that show very rather poor crystal quality as indicated by the transmission), is not consistent with the theory of microscopic disorder and suggests that the asymmetry is due to macroscopic sample quality. Abram et al. also considered this case and concluded that from their data they cannot decide if the nonexponential decay was caused by microscopic disorder or by a distribution of nearly perfect crystalline regions having different spatial extent and exhibiting finite crystal selection rules. Since the crystal preparation in Abram's and our experiments were very similar it doesn't seem unlikely that the latter effect explains the observations in both experiments. Future high resolution SRS measurements at lower temperature and possibly in single crystals should help to resolve these unanswered questions.

Linewidths of Isotopic Impurities

Irrespective of the puzzle about the observed line asymmetry, high resolution SRS provides an accurate way of measuring the width of the site energy distribution σ. A value for σ cannot be obtained directly from the spectral width of the "host" material because of the motional narrowing effect that is associated with the extended vibronic excitation in the crystal. But σ can be deduced from the linewidth of an isolated isotopic impurity in the crystal. From spontaneous Raman spectra of $^{15}N_2$ doped in nitrogen, an upper limit of 0.25 cm-1 was deduced for σ[50].

We measured the linewidth of the vibrational line of 0.74 % naturally occurring $^{15}N^{14}N$ in nitrogen using high resolution SRS in thin film samples and in bulk crystals (see Fig V.6). Typical linewidths for the thin film samples and the bulk samples are 0.065 cm^{-1} and 0.030 cm^{-1} giving an upper limit for σ in α-N_2 which is about twice the linewidth of the motionally narrowed $^{14}N^{14}N$ line. We also measure the linewidth of the $^{15}N^{14}N$ impurity in the liquid and the beta phase and found that in these cases there is no difference from the linewidth of the "host" material.

MATRIX ISOLATION SAMPLES

The detection of $^{15}N^{14}N$ in nitrogen suggests that SRS may prove useful for matrix isolation experiments. To our knowledge the only report of such an application using nonlinear Raman methods was by Beattie et al.[85]. Beattie et al. also pointed out that SRS would be advantageous in such applications since there is no line distortion due to interferences with nearby resonances or with the nonresonant background of the host material. High resolution SRS would permit the measurement of true linewidths and of small splittings due, for example, to different sites in a host material or to possible rotational structure for small molecules in large host cavities. To explore the potential of SRS for such applications, we have done several matrix isolation experiments. Fig. V.7 (bottom) shows the N_2 stretching region for a sample of 5 % N_2 in Ar at 15 K. We observe a much larger linewidth compared to neat N_2 and a reproducible shoulder on the high frequency side of the band. These results are in good accord with those of Kiefte[86] et al. who did Raman studies using conventional Raman scattering in combination with a Fabry-Perot etalon. Using large single crystals of Ar doped with a few percent of N_2, they resolved more clearly a doublet structure with a splitting of 0.12 cm^{-1} and attributed the high frequency components to N_2 dimers formed in the Ar matrix. The close proximity of the monomer and dimer frequencies may also occur in the gas phase and may account for the absence of distinguishable nitrogen dimer resonances in our jet expansion studies on N_2 described in the next chapter. We speculate that the weak broad feature near 2325 cm^{-1} in our matrix spectra is due to larger clusters. Further experiments to examine the concentration dependence of the band structure would be worthwhile.

There are also suggestions of cluster structure apparent in the CO/N_2 matrix band shown on the left in Fig. V.8. This feature is similar to but more symmetric than the corresponding CARS line reported by Beattie[85]. The effect of the CO impurity on the N_2 host

A_g and T_g lines is shown on the right of Fig. V.8. We note the appearance of several sharp sidebands on the low frequency side of the A_g component when the N_2 sample contained 3 % CO. Similar structure occurred when impurities of O_2 where in the sample. These surprisingly narrow lines have not been seen previously and their widths are suggestive of several well-ordered local crystal sites, or perhaps rotational structure in a primary site. More insight into their origin could be had from studies of the effects of temperature, annealing, and dopant concentration on these bands. Conventional Raman spectroscopy has been used to investigate other features of matrix samples. For example, Jodl and coworkers[73,74] have examined the effect of adding nearest neighbor Ar atoms on the Davydov splitting in nitrogen and have measured temperature and pressure effects on dopant frequencies to study anharmonic guest-host interactions. Diffusion and annealing processes have also been investigated. Ozin has reviewed the many applications to the study of unstable and reactive molecules[87]. Results of our preliminary experiments suggest that SRS may be advantageous in these types of studies. The principal advantages of SRS are the high resolution, the elimination of background fluorescence, and a lower average power on the sample (≅ 10 mW versus 100-1000 mW) which reduces sample heating. Limitations are the need for transparent samples of good optical quality and narrow lines in order to get high sensitivity.

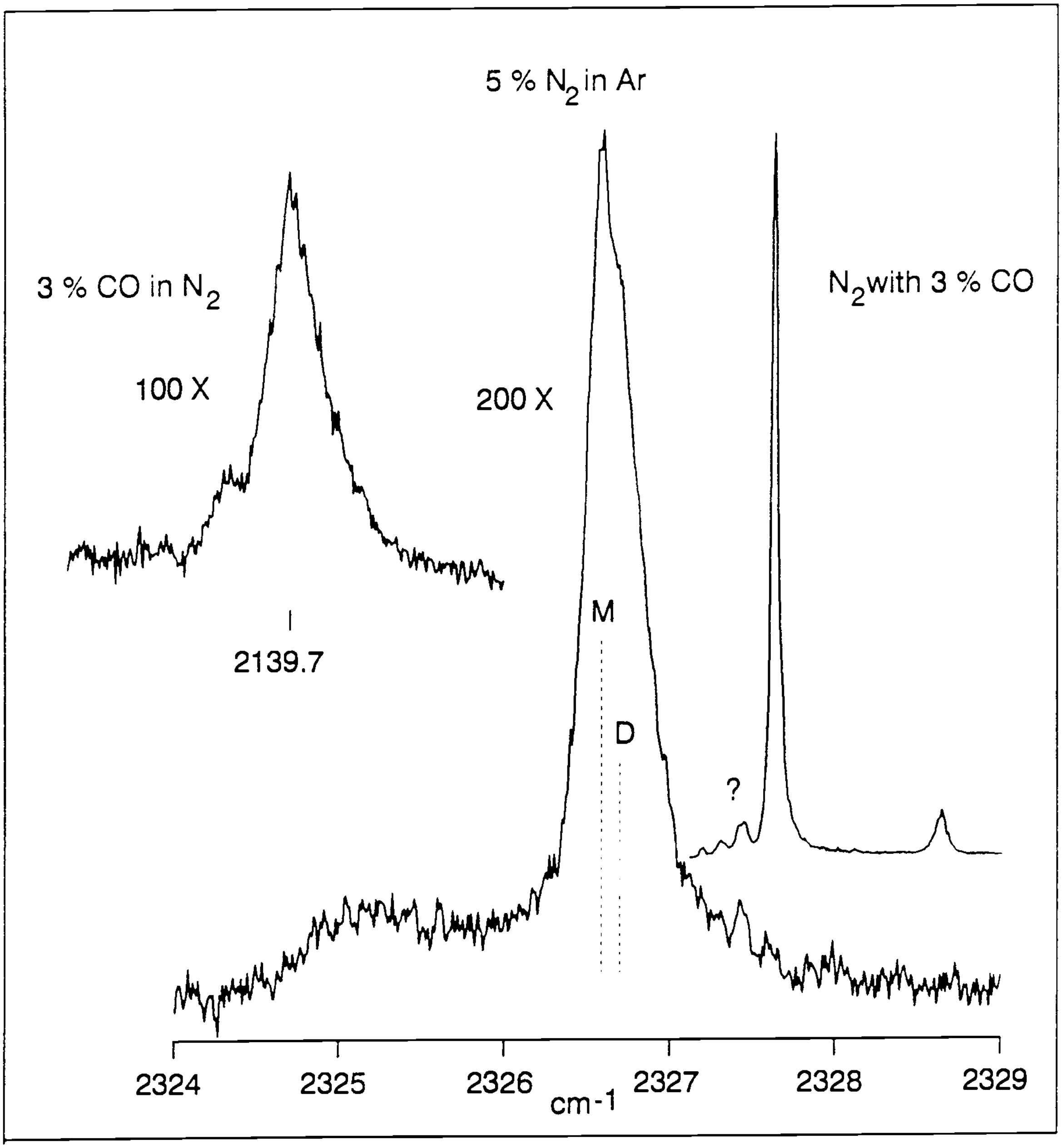

Figure V.7 : SRS matrix isolation spectra of 5 % N_2 in Ar (center) and α-N_2 with 3 % CO added: CO region, left; N_2 region, right. The frequency scale is the same for all features. The symbol M and D stand for monomer and dimer with a splitting of 0.12 cm^{-1} from ref. (86) indicated by dashed lines.

CHAPTER VI: SRS STUDIES OF CONDENSATION IN FREE JET EXPANSIONS

INTRODUCTION

The main application of high resolution SRS has been, so far, the study of gas phase Raman lineshapes. For example, several groups have studied the temperature and pressure dependence of vibrational and rotational Raman transitions of N_2 in order to generate data that can be used for accurate model calculations of gas phase spectra. Such models are used in remote sensing applications of nonlinear Raman spectroscopy, mainly CARS, to extract temperature and density information from experimental Raman spectra. In the work described in this chapter SRS is used to study cluster formation in free jet expansions. This is the first application of SRS to the study of aggregation processes, a topic of much current research interest.

Supersonic jet expansions are widely used to produce conditions under which molecular clusters can be formed. A variety of experimental techniques such as electron diffraction, electron-beam or laser excited fluorescence, photoelectron spectroscopy, infrared absorption, mass spectrometry, and, more recently, coherent Raman spectroscopy[88] have been employed in the studies of cluster properties. Much of this work has focused on the structural and dynamical characteristics of small molecular clusters (dimer, trimer,...), but there is also considerable interest in the study of larger aggregates and how their properties compare to those of the bulk material. Models for the gradual evolution from small-to-large clusters are important in understanding the condensation process in a supersaturated gas. Several groups have used molecular dynamics simulations to study the size dependence of the solid-liquid phase change in argon clusters[89,90]. The role of impurities and charged species in accelerating the nucleation process has also been investigated[91]. Further descriptions of recent work on gas-phase clusters can be found in Ref. (92).

For very large clusters ($>10^3$ units), where the surface-to-volume ratio is small, one expects merger to the physical properties of the bulk liquid or solid. Bartell and co-workers have used electron diffraction to study such clusters and have observed solid-like, liquid-like, and amorphous character, depending on the cluster material and the expansion conditions[93]. In this chapter we report the use of stimulated Raman loss spectroscopy for a similar purpose, in a specific study of the condensation and freezing of large clusters formed efficiently in expansions of N_2 from a long channel nozzle. Well-defined changes in the vibrational Raman spectrum are seen and associated with the possible phase transitions as cooling occurs in the expansion. Comparison with the measurements on static liquid and solid nitrogen described in the previous chapter yields precise frequency-temperature relations which are used to deduce internal temperatures for the molecular clusters as they are formed and cool in a free jet expansion. Such measurements of the internal "thermodynamic" temperature of a cluster have not been achieved before even though they are of critical importance in understanding the condensation process.

EXPERIMENTAL

Frequency Calibration

For the nitrogen measurements the 514.5 nm line of the argon ion laser was used as the probe frequency. The Raman shifts were calibrated using the known frequencies of the N_2 monomer Q-branch transitions[94]. An absorption spectrum of I_2 was recorded simultaneously with the Raman spectrum by sending a small part of the cw dye laser beam through a cell that contained I_2 at its room temperature vapor pressure (0.25 Torr). The frequencies in the visible range of the I_2 absorption spectrum are known very accurately[95] and were used to verify the calibration of the wavemeter.

Pulsed Jet Assembly

The pulsed valve assembly was a modified Bosch fuel injector, mounted in a dewar. The design of the modification was done by Dr. George Pubanz and is described in ref (63). To enhance the cluster formation the valve assembly can be cooled by adding a slush bath in the dewar or by a stream of cold air produced by blowing dried compressed air through a large reservoir of liquid N_2. By adjusting the flow rate the sample temperature could be varied from room temperature down to 110 K and kept constant within a few degrees K for several hours. The temperature of the sample gas was measured with a thermocouple positioned in the sample stream inside the valve housing.

Several round and slit nozzles were tested and it was found that the length of the nozzle channel was an important factor in these condensation experiments. A long channel length (2.5 mm for a hole diameter D = 0.18 mm) allowed observation of the Raman spectrum out to large values of X from the nozzle (X/D 100) and made the observation of the liquid-solid phase transition possible. For nozzles with smaller channel length (0.25 mm) the density along the center line of the jet fell off more quickly and the cluster signals were greatly reduced.

Sampling Volume

In order to probe the expansion with good spatial resolution, the laser beams were tightly focused and crossed at the sample point. From the geometry the sample volume was limited to a cylinder of 50 μm diameter and 1 mm length but, because of the nonlinear power dependence, most of the signal is produced in an even smaller volume.

RESULTS

Fig.VI.1 shows SRS Q-branch spectra of neat N_2 in a static cell (a) and in free jet expansions (b,c). In jet spectrum (b) the sample reservoir was at room temperature and no signs of condensation are seen in the spectrum although the rotational cooling is quite significant at the high driving pressure used. For spectrum (c) the reservoir was cooled to 160 K and a new, polarized feature appears in the spectrum at 2326.45 cm-1 which is attributed to clusters.

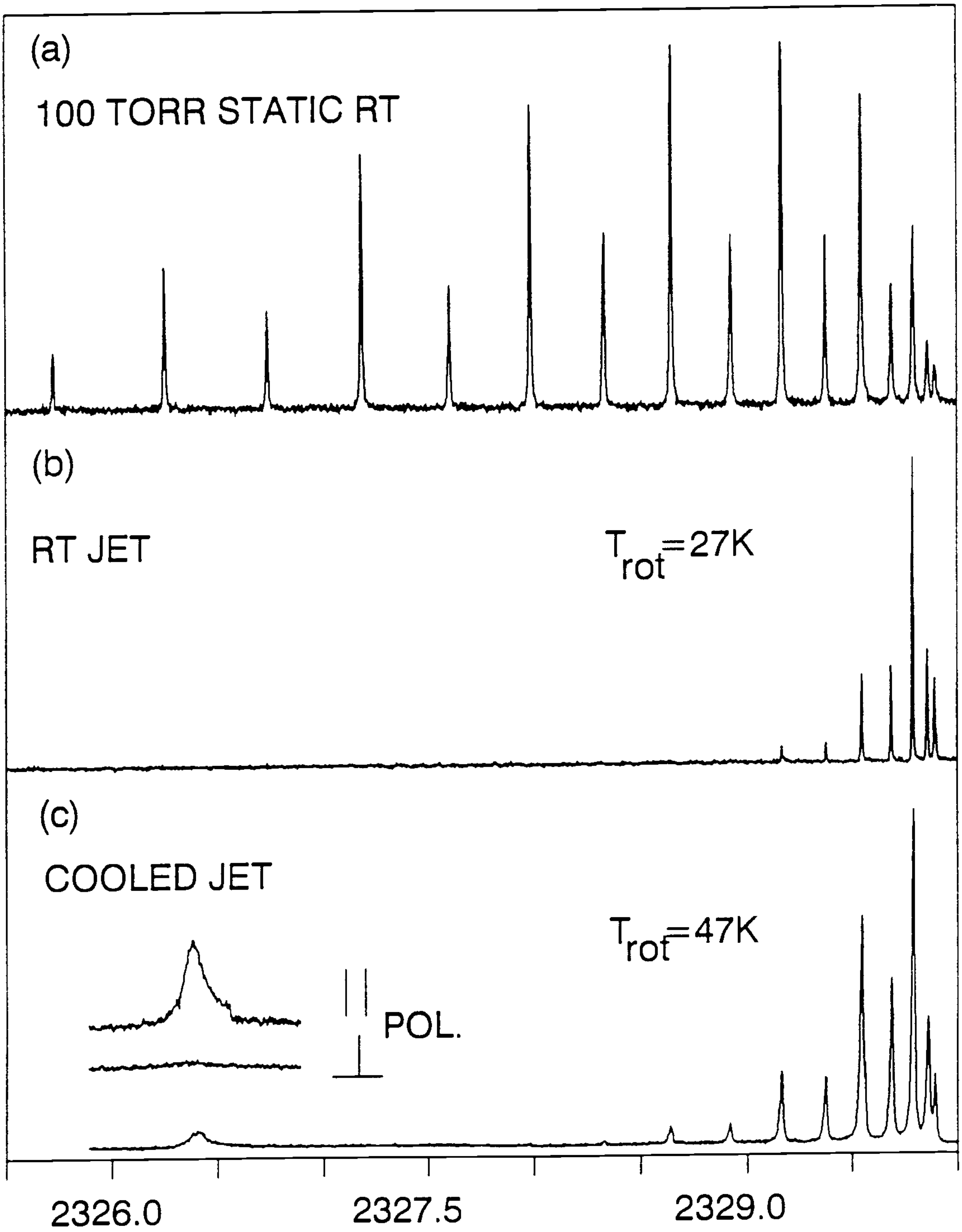

Fig. VI.1: SRS spectra of the vibrational Q-branch of nitrogen.

(a) 50 Torr N_2 in static cell at 290 K

(b) Neat N_2 jet expansion with T_0= 290 K, P_0= 50 atm.

(c) Neat N_2 jet expansion with T_0= 160 K, P_0= 28 atm.

A polarized band due to N_2 aggregates appears at 2326.45 cm-1.

Estimate of the Cluster Size

The size distribution of these aggregates is unknown, but a rough size is estimated from the following observations. In expansion (b), no Rayleigh scattering could be seen by eye but, under the conditions of expansion (c), a weak track of the focused laser beams was visible at 90 degrees. This visual scattering is assumed to be Mie scattering that occurs when the particle radius becomes comparable to the wavelength of the scattered light. The theory of Mie scattering predicts a very large decrease in 90 degree scattering intensity as the particle radius decreases (a factor of 10^{-4} in going from 2000 nm to 50 nm for incident light at 500 nm[96]. In our cell, scattering from particles smaller than 50 nm would probably not have been visible due to background arising from reflections from windows, lenses, etc. It seems likely that these smaller clusters are consumed in the growth of the larger aggregates. That the latter could be as large as 2000 nm can be deduced from the observation that the Mie scattering increased strongly at higher driving pressures or lower reservoir temperatures than those used in (c) and, in particular, the amplitude fluctuations in the probe beam became quite large (1%), making detection of the much weaker Raman loss signal impossible. This implies a particle radius of a few μm if we assume that the noise comes from simple 1% attenuation due to passage of clusters through the probe focal spot (50 μm diameter). Thus we believe that the 2326 cm^{-1} feature seen under the less-condensing conditions of expansion (c) derives mainly from 50-500 nm particles containing 10^6 to 10^9 N_2 units. This number is large enough that we would expect bulk properties to be observed, an assumption clearly supported by the spectral changes described below.

A second independent estimate comes from the theoretical predictions for the condensate size distribution by Koppenwallner and Dankert which was described in chapter II.3. For a free jet expansion with T_0 = 160 K and P_0 = 3 atm they calculated a size range of 20-200nm which is in good agreement with our estimate of slightly larger aggregates produced in our experiments with T_0 = 160 K and P_0 = 28 atm.

Phase Transitions in the Jet Expansion

In experiments with neat nitrogen expansions from a 180 μm nozzle it was found that high driving pressures in combination with cold reservoir temperatures lead to condensation of nitrogen in the jet expansion. The condensation onset can be detected by the weak scattering of the laser beams that becomes visible in the jet region. At the same time when the scattering becomes visible to the eye in a dark room the SRS signal of the aggregates appears.

The Vapor-Liquid Phase Transition

Fig. VI.2 and VI.3 show a series of scans that were taken at different distances from the nozzle (measured in units of the nozzle hole diameter D) under identical expansion conditions (28 atm driving pressure, 160 K reservoir temperature). For $X/D < 1$ only the spectrum of the N_2 monomer is seen in Fig. VI.2 which shows that the condensation does occur in the jet expansion. The monomer lines are broadened significantly due to the high density in the initial stages of the expansion.

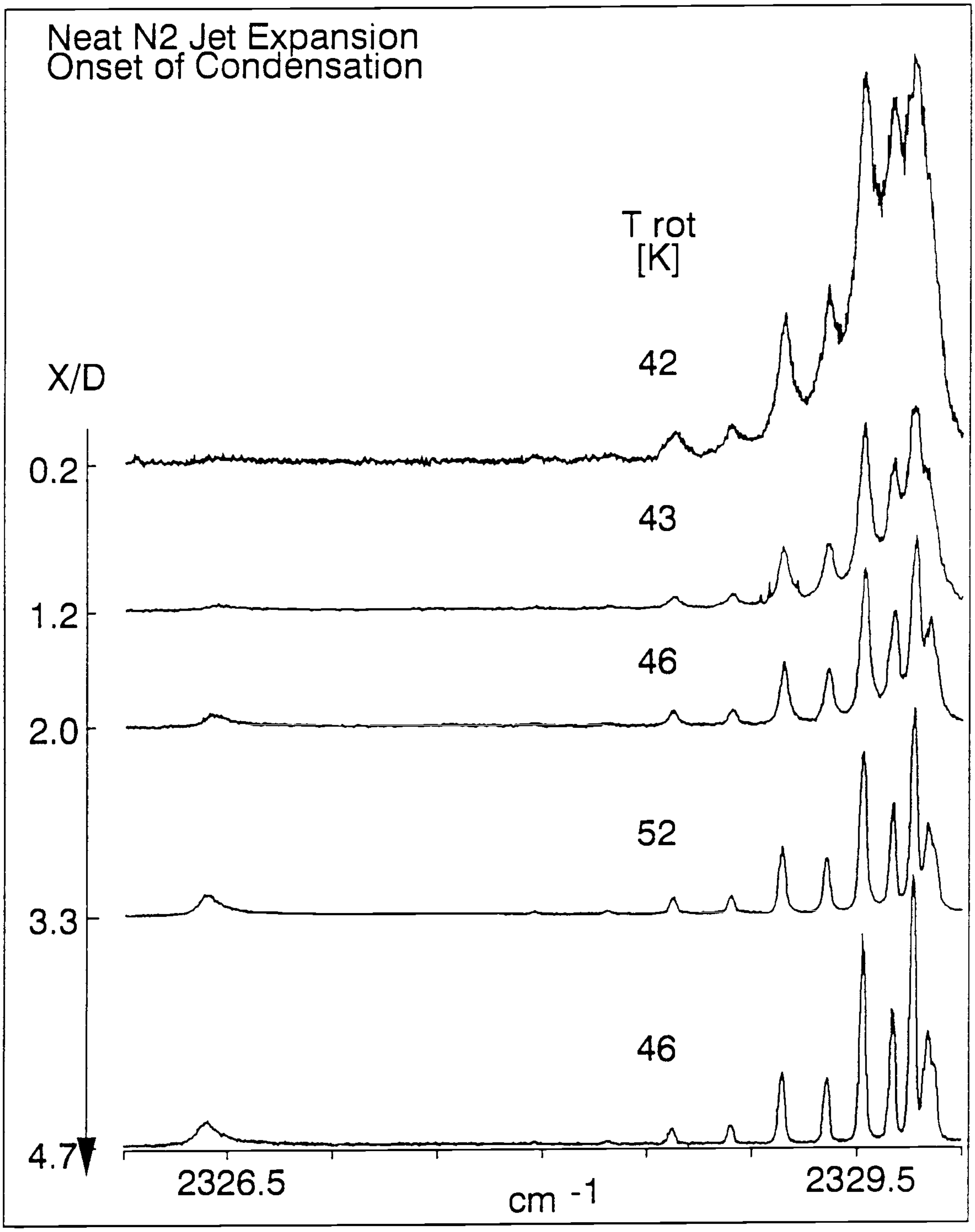

Figure VI.2: SRS spectra at the early stages of the expansion. Each scan covers the monomer Q-branch region as well as the aggregate feature. It can be seen that the aggregates are formed in the expansion for 1 < X/D < 5. From the monomer spectra one can determine the rotational temperature from the intensity of the rotational structure and the effective pressure from the pressure broadening.

The cluster feature at 2326.45 cm-1 appears at X/D ≅ 1 at which point T_{rot} = 41 K for the monomer. The cluster peak gains significantly in intensity relative to the monomer as X/D is further increased. The peak also shifts to lower frequency with increasing X/D. By comparison with our measurements on bulk liquid and solid N_2, described in the previous chapter, this temperature dependence of the Raman shift confirms the assignment of the aggregate feature to the liquid phase.

The Liquid-Solid Phase Transition

At X/D ≅ 21 a shoulder appears on the high frequency side of the liquid line (see Fig. VI.3) and gradually grows into a separate line, whereas the liquid line decreases in intensity until it has disappeared at X/D ≅ 35. The frequency, width, and temperature shift are consistent with the assignment of this peak to the β-phase of solid nitrogen. The β-phase of nitrogen is stable between 35.6 K and 63.1 K for N_2 in equilibrium with its vapor. From X/D ≅ 35 to X/D ≅ 73 the β-solid peak shifts to higher frequency, indicating further cooling of the clusters as they travel downstream in the jet towards the shock boundary (Mach-disk).

For X/D ≅ 110 the sampling point has moved through the Mach-disk. Rotational lines of warm monomer appear on both sides of the solid peak, which itself has shifted significantly to lower frequency, due to the increasing temperature.

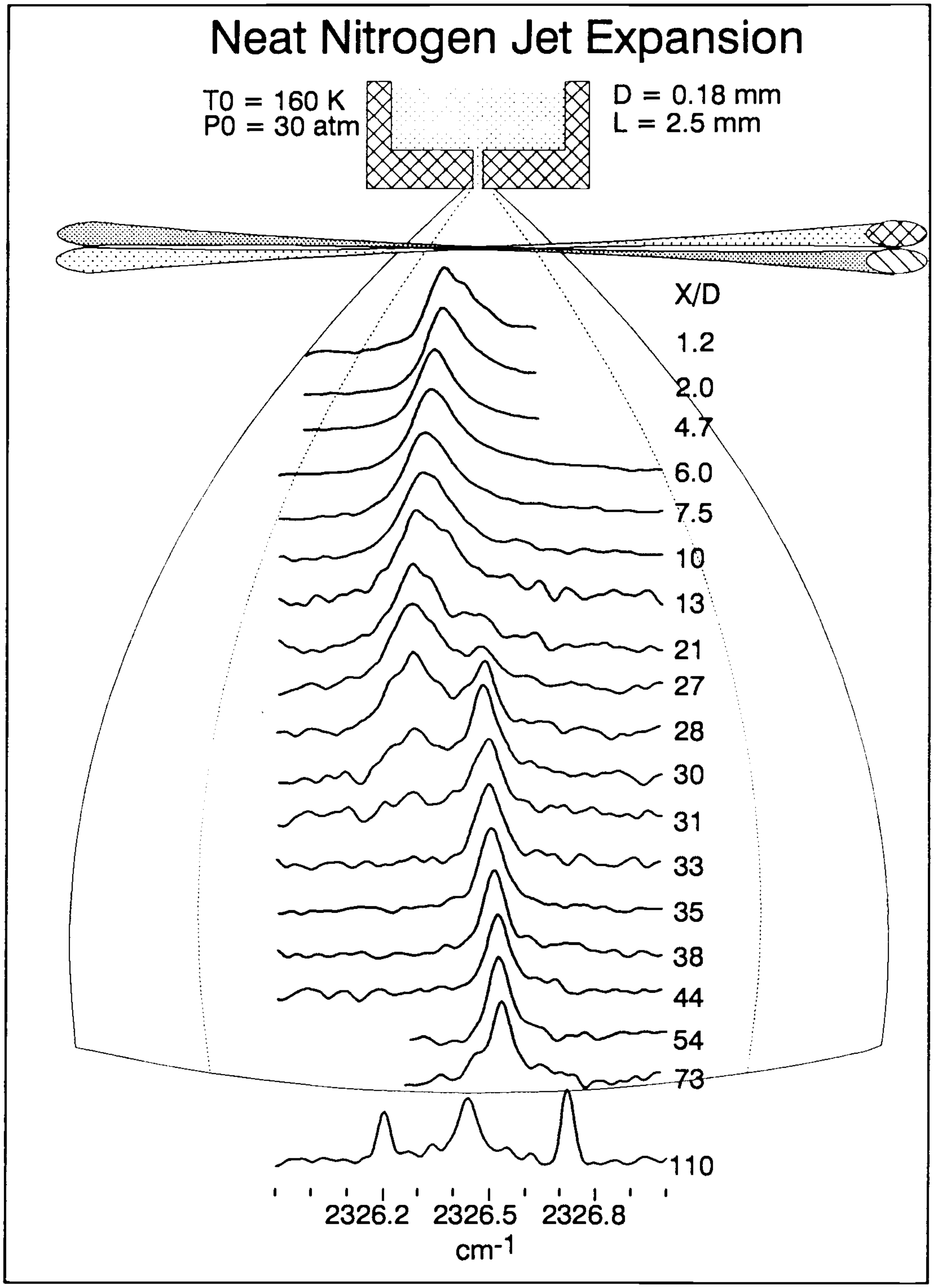

Fig. VI.3: SRS spectra of the aggregate band at different points along the axis of a neat N_2 expansion with P_0= 28 atm, T_0= 160 K.

The α-β Phase transition - Jet Experiments with a Driving Gas

Experiments using He as a driving gas show a more rapid cooling of N_2. The spectra obtained from 10% N_2 in He expansions (see Fig. VI.4) show initially the same development as for neat expansions, but at a much smaller value of X/D. One can see the liquid peak, the liquid to β-solid phase transition and subsequently a further shift to higher frequency, combined with a broadening of the line. Again, comparison with the static samples leads to the interpretation that the β- to α-solid phase transition is observed. This phase transition was not seen in the neat N_2 expansions where the cooling is insufficient to lower the internal temperature of the aggregates below the point of the phase transition at 35.6 K.

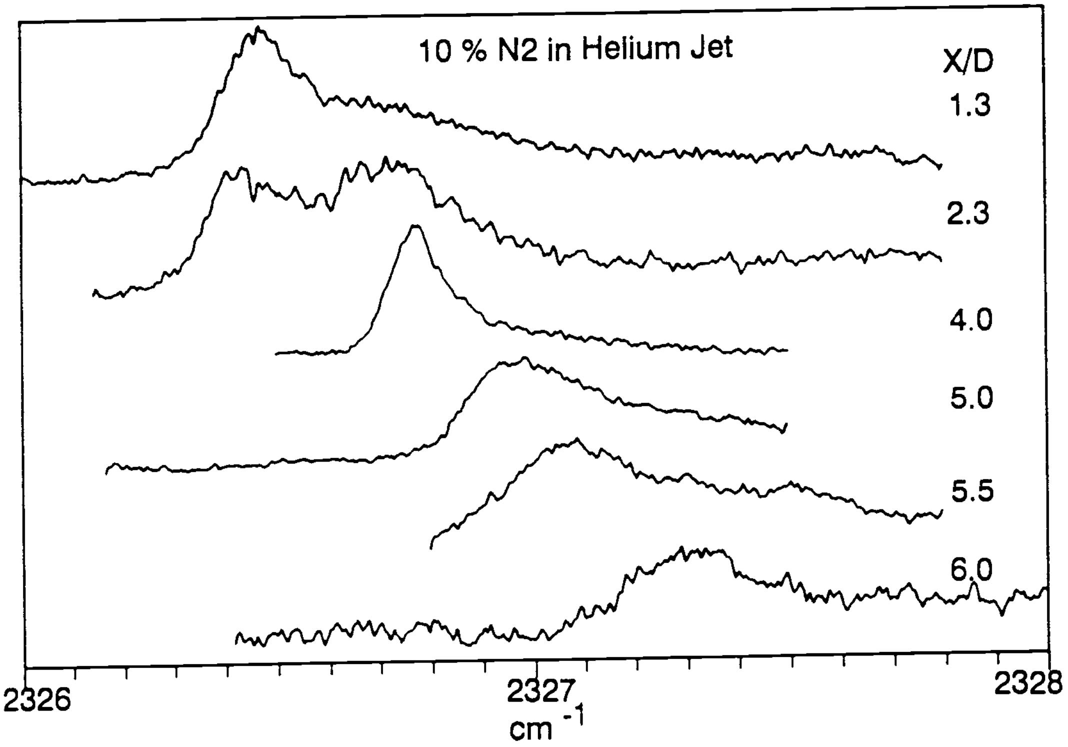

Figure VI.4: Aggregate spectra in a Helium expansion containing 10 % nitrogen. The stronger cooling in He makes it possible to observe the β → α phase transition in the aggregates.

Temperature of the Aggregates

The Raman spectra of the static liquid and solid N_2 not only aided in interpreting the jet spectra, but they also enabled us to estimate the internal temperature of the clusters in the jet as a function of X/D. This was done by comparing the measured vibrational frequency of the cluster with the measured temperature dependence of the vibration in static samples of liquid and solid N_2. Since the spectra for the static samples and the jet spectra were taken with the same SRS setup, it is possible to compare the absolute Raman shift with high accuracy (0.007 cm-1). This comparison shows that the internal temperature of the liquid droplets appearing at $X/D \cong 1$ is 74 K (see Fig. VI.5). The droplets cool subsequently and their temperature reaches the triple point value of 63.15 K at X/D of $\cong 7$. Since the frequency continues to shift to lower values it is concluded that the droplets are being supercooled before they freeze. The droplet temperature for $X/D > 7$ cannot be determined by direct comparison with bulk liquid since the supercooling was not observable in the equilibrium samples.

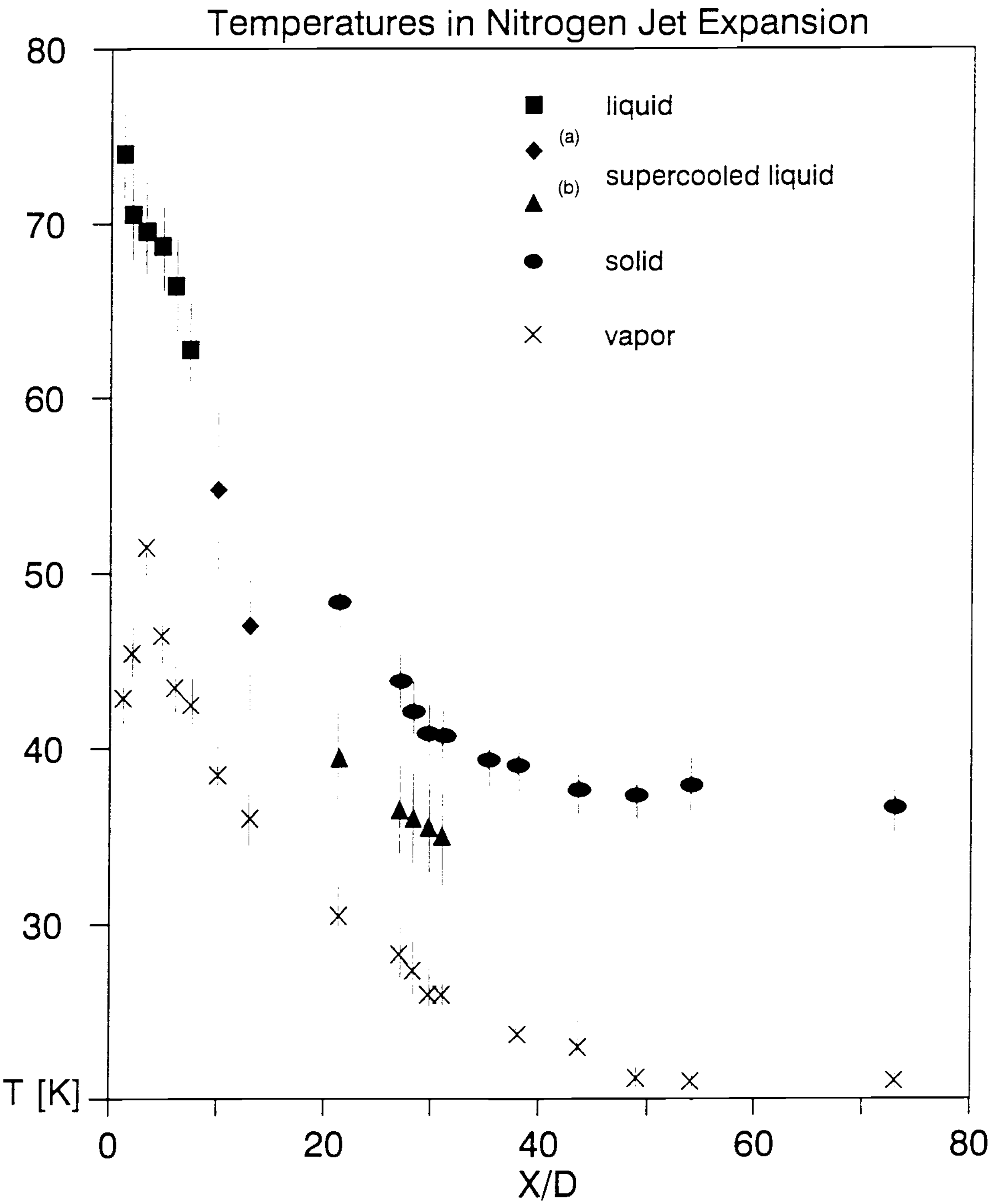

Figure VI.5: Temperatures in the free jet expansion determined by SRS. Internal temperatures for liquid and solid were determined by comparison with the frequency-temperature relations measured on equilibrium sample. For the supercooled liquid the temperatures were calculated from the measured solid temperatures assuming an adiabatic freezing process. The vapor temperature is determined from the intensity distribution of the rotational lines in the monomer Q-branch.

Temperature of the Supercooled Droplets

The absence of experimental data for the Raman shift in a static sample of supercooled liquid N_2 brings up the interesting question: how can one use the measured frequency data to determine the temperature of the supercooled droplets in the jet?

Perhaps the most straight forward approach is an interpolation of the measured liquid frequency temperature data above 63 K (Fig. VI.5) by a straight line or a polynomial. However, the droplet temperature that are calculated in this way for X/D from 21 to 35 are <u>above</u> the measured temperatures for the solid that is formed in this X/D range. Since it is expected that the heat of fusion will cause the solid phase to be <u>warmer</u> than the supercooled liquid, the liquid temperatures obtained from the extrapolation are considered to be incorrect.

This failure can be understood from the results of recent experiments by Baggen[17] who measured the density dependence of the N_2 Raman shift by applying large external pressure in a diamond anvil cell. These experiments showed that an increase in the density of liquid N_2 from 0.93 g/cm^{-3} to 1.42 g/cm^{-3} causes the vibrational frequency to <u>increase</u> by about 7 cm^{-1}. Assuming that the temperature shift of the frequency is mainly a density effect[5] we can convert temperature dependence shown in Fig. VI.6 to a density dependence (Fig. VI.7) and find a <u>decrease</u> in the vibrational frequency with

---

[5] This been shown for liquid nitrogen in several experimental[97] and theoretical studies[98].

increasing density in the range from 0.65 g/cm^{-3} (110 K) to 0.87 g/cm^{-3} (63 K). Therefore $\frac{d\nu}{d\rho}$ has to change sign from negative to positive somewhere between 0.87 g/cm^{-3} and 0.93 g/cm^{-3}. This interesting "turnaround" in the frequency is due to the fact that the short range repulsive forces become dominant at high liquid densities. Since there is no experimental data available in the literature for the relevant density range and since the turnaround is expected to be rather abrupt, a simple extrapolation below the triple point is highly unreliable and therefore not a good method for extracting density (i.e. temperature) information from our spectra of supercooled droplets.

There is however, a different way in which the temperature of the supercooled liquid can be estimated. We know the temperature of the solid β-phase microcrystals in the jet rather accurately (±2 K) since precise data from our CW-SRS experiments is available over the whole temperature range. If one assumes that the freezing of the supercooled droplets occurs adiabatically, one can calculate the temperature of the liquid before it froze from the known heat of fusion and the heat capacities of liquid and solid N_2. One finds that after adiabatic freezing of the liquid at 40 K the solid will be at 48 K. If any heat is released by evaporation or collisions this temperature difference will be smaller. In this way we can calculate a lower limit for the temperatures of the supercooled droplets from the temperature of the solid phase at each X/D position (see Fig. VI.5).

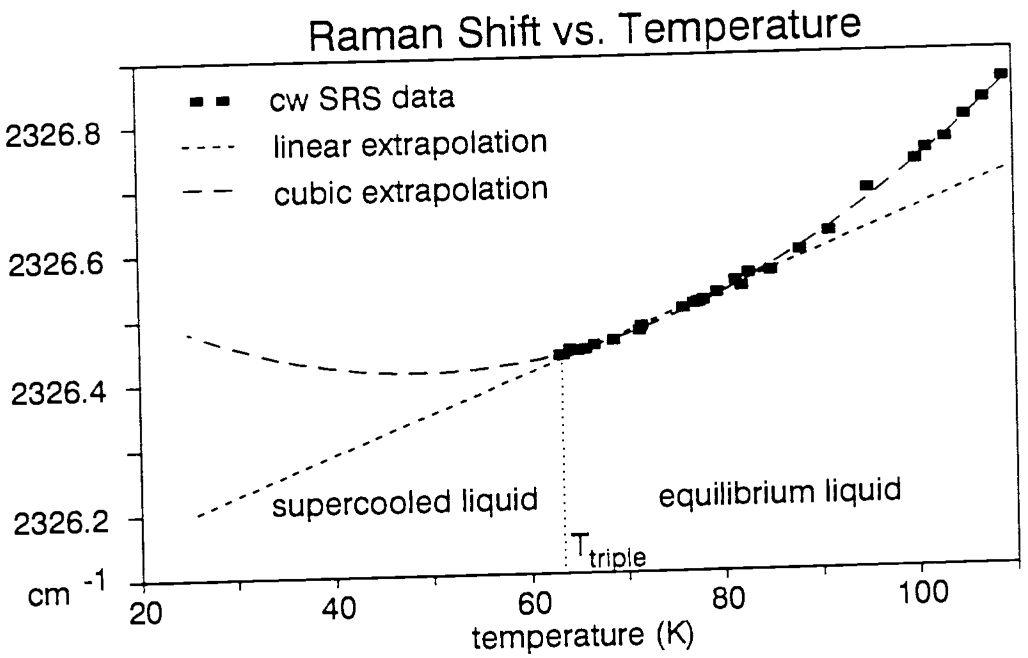

Figure VI.6 Temperature dependence of the vibrational frequency in liquid nitrogen determined from high resolution SRS spectra of equilibrium samples. Supercooling was not observable in equilibrium sample. The dashed lines show linear and cubic extrapolation of the data below the triple point.

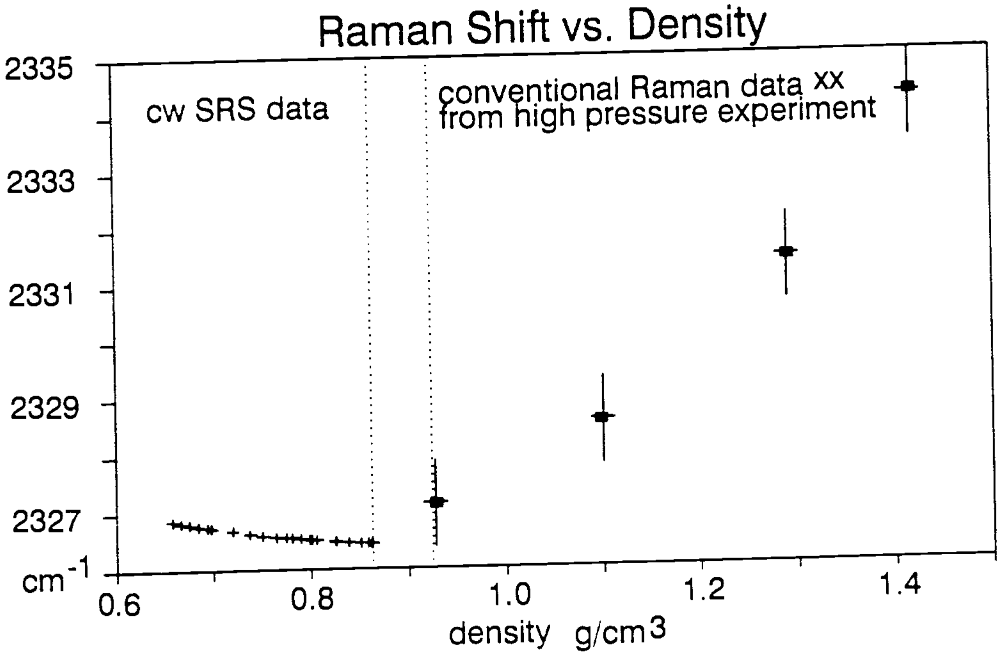

Figure VI.7: Vibrational frequency vs. density in liquid nitrogen. Left: SRS data measured along the liquid-vapor coexistence line. Temperature was converted to density using relation from ref. 100. Right: Data from high pressure Raman measurements of ref. 17.

Rotational Temperature of the Monomer

Fig. VI.5 also shows the rotational temperatures of the N_2 monomers deduced from the Q-branch intensity distributions. The monomer temperatures are consistently lower than those of the aggregates, which is to be expected since the energy released in the condensation process will heat the aggregates. One sees in Fig. VI.5 that part of the heat of condensation is transferred to the monomer gas either by evaporation or by collisions causing the rotational temperature of the monomer to rise in the early stages of the expansion. For $X/D > 5$ the rate of condensation decreases because of the decreasing density in the jet, and cooling due to residual two-body collisions dominates.

Extent of Aggregation

The integrated intensities of the cluster band and the monomer lines provide a measure of the relative extent of clustering, a characteristic which is difficult to determine by most probing methods. To a good approximation, the Raman cross section can be taken to be independent of phase provided that a local field correction L is applied for the liquid and solid phase intensities (11). Taking $L = (n^2 + 2)^4/81$ with $n_{liq} = 1.205$ and $n_\alpha \cong n_\beta = 1.22$ we obtain the cluster percentage shown in of Fig. VI.8.

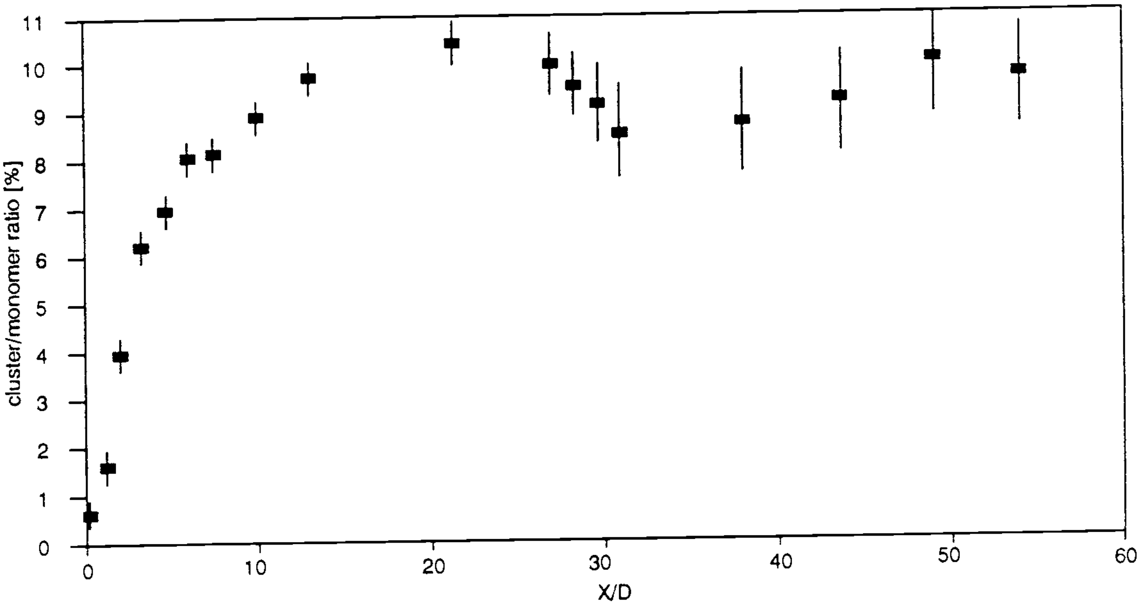

Figure VI.8: Extent of aggregation as function of X/D.

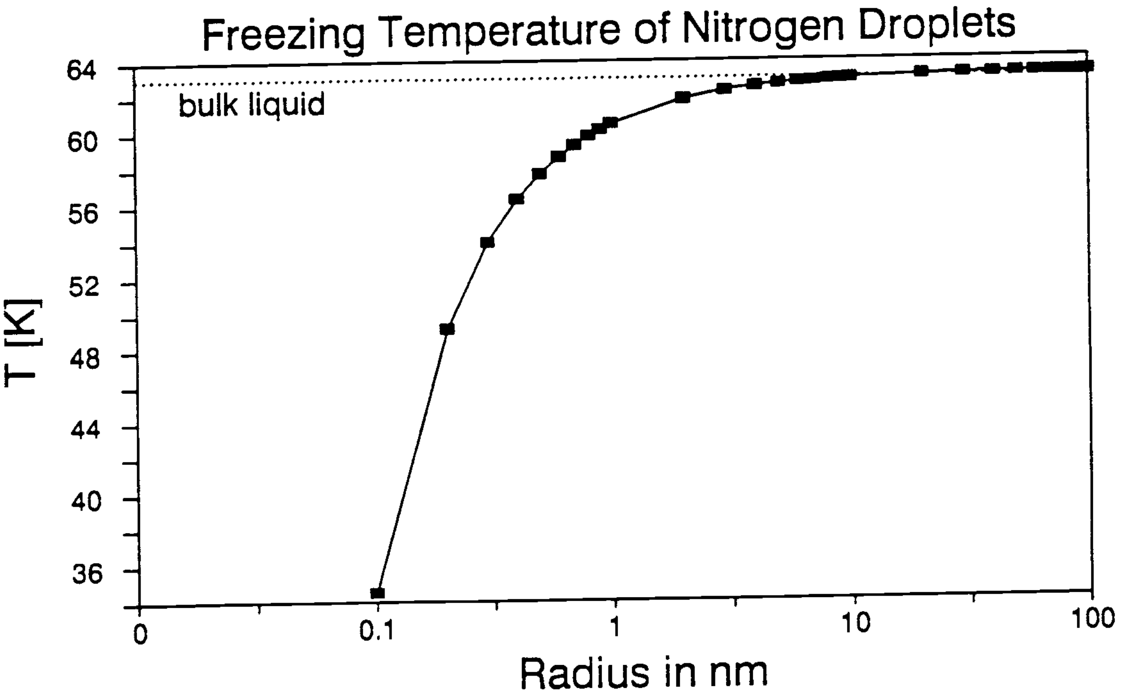

Figure VI.9: Calculated melting temperature as a function of droplet size.

Size Effects on the Freezing Temperature

The measurement of the aggregates temperatures depends critically on the assumption that the observed aggregates can be treated as bulk liquid or solid material. It is well known that thermodynamic properties such as the freezing point and the vapor pressure become size dependent for very small particles. One can estimate the change in the freezing point for nitrogen droplets using the following phenomenological equation that was derived within the framework of thermodynamics by Pavlov[102].

$$\frac{T}{T_0} - 1 = - \frac{2}{\rho_s L\, r} \left[\gamma_s - \gamma_l \left(\frac{\rho_s}{\rho_l} \right)^{\frac{2}{3}} \right] \tag{6.1}$$

with: T_0 = bulk freezing point

L = latent heat of fusion

γ_s, γ_l = surface tension: gas - solid, gas - liquid

ρ_s, ρ_l = density of solid, liquid phase

By substituting the appropriate values for N_2 one finds that for droplets larger than about 5 nm in diameter (10^3 molecules) the size effects become negligible (see fig. VI.9) Since we estimated the size range of the droplets observed in our experiments to be 50 - 500 nm we do not expect that size effects play a major role for the freezing transition.

Linewidth of the Aggregate Spectra

It is interesting to compare the linewidths in the aggregate spectra with those in the spectra of equilibrium samples in order to see what kind of information can be deduced from these widths. Fig VI.10. shows such a comparison for several positions in the jet expansion. The jet spectra consistently show a larger linewidth than those of the bulk samples. The difference in linewidth could be due to several effects:

1) experimental broadening due to saturation or optical Stark shift
2) experimental broadening due to finite sampling volume
3) distribution of cluster temperatures
4) distribution of cluster sizes

In the following section we will assess the influence of these effects on the linewidth to determine the dominating contributions.

1) The results for gas phase Q-branch spectra of N_2 described in chapter II.3 showed that saturation was not observable but the optical Stark effect caused an asymmetric line broadening of 0.02 cm^{-1} for 15 mJ of pump power for the FWHM. This effect, magnified by the local field correction $L \cong 1.83$ should also be seen in the condensed phases. Since the aggregate spectra were taken with a pump power of 8 mJ/pulse a significant part of the broadening of the liquid peak and all of the observed broadening of the solid peak can be accounted for by the optical Stark effect.

2) One expects some broadening due to temperature variation over the finite size of the sample volume. This can be estimated from the known focal diameter (50 micron) and the measured temperature variation of the aggregates with X/D. Fig. VI.11 shows the result of this estimate which indicates that the finite size of the sampling volume is negligible due to the very tight focusing of the beams and the crossed beam geometry.

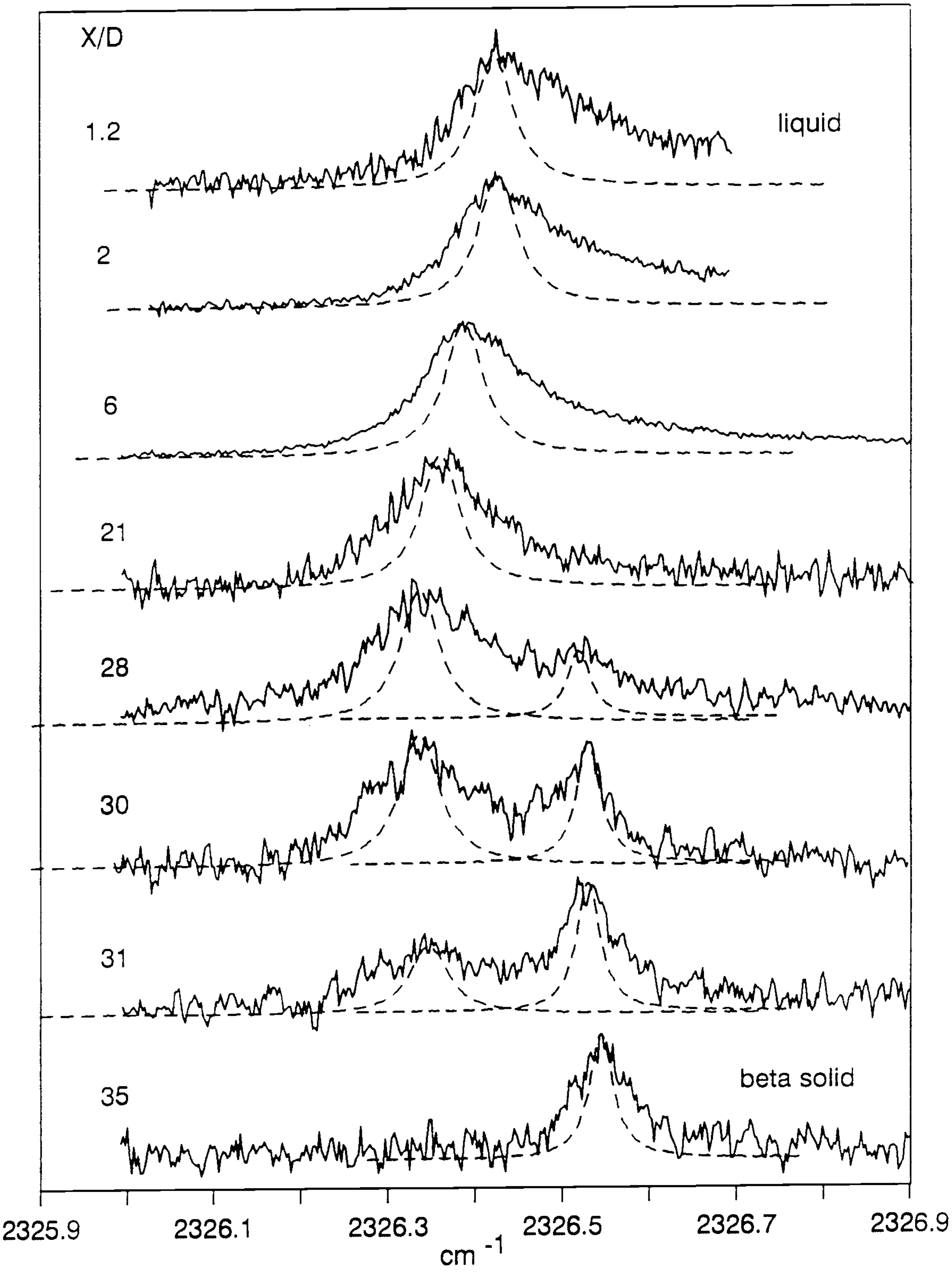

Figure VI.10: Comparison of lineshapes between spectra for N_2 aggregates formed in free jet expansion (solid lines) and spectra of static samples of liquid and β-solid. Note the decrease in asymmetry of the liquid aggregate feature for increasing X/D.

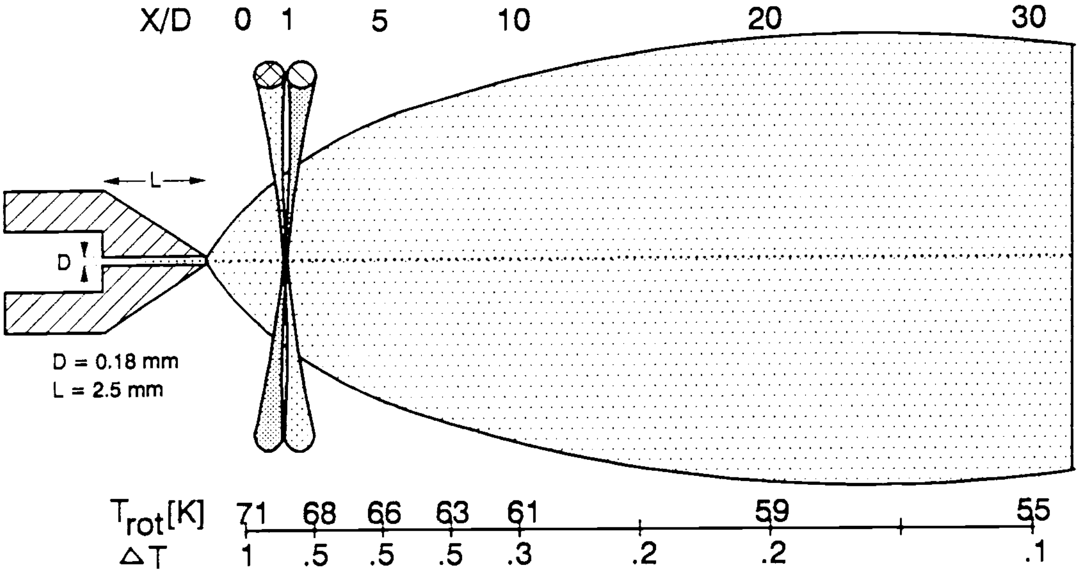

Figure VI.11: Effect of finite sampling volume on measured linewidths. The sample volume, defined by the crossed beams, is a cylinder of 50 μ diameter and 1 mm in lenght.

3) At a given X/D point, a distribution of aggregate temperatures would also cause a broadening of the aggregate line. However, if there were a significant temperature distribution one would expect the solid β-phase line to be broader than the liquid peak since the temperature coefficient for solid β-N_2 is about twice that of liquid N_2. The fact that the solid peak is very narrow indicates that the aggregates all have very similar temperature for a given value of X/D.

4) Finally one must consider the importance of size effects. A distribution of aggregate sizes would not lead to a broadening if all the aggregates are large enough to be treated as bulk material. For very small aggregates, frequency shifts can be expected to be to higher frequency towards the gas phase monomer value. This change in frequency and can be understood if one considers the molecules on the

surface of the droplet. The net force on the intermolecular bond for a molecule on the surface will be smaller because of a smaller number of nearest neighbors. Therefore the molecules in the outermost layer of the droplet will vibrate at slightly higher frequency which will lead to a size dependent asymmetry of the vibrational line for small liquid droplets. For 50 nm and 5 nm diameter droplets about 4 % and 33 % of the molecules will be in the surface respectively. Since the size of theoretically predicted condensation nuclei is of the order of a few nm (see Fig. II.3.5) it is not unlikely that the asymmetry of the line due to liquid aggregates is caused by this size effect. This interpretation is supported by the fact that the observed asymmetry decreases with increasing X/D in the expansion, presumably because the droplets grow to larger sizes where the size effect becomes less pronounced.

In conclusion, this analysis seems to favor the picture that the lineshape in the jet is mainly due to the optical Stark broadening, but that the asymmetry observed for the liquid peak could be due to very small droplets containing a few hundred to a few thousand molecules. This suggests that it is possible to study very interesting effects of the large surface to volume ratio in these small droplets by systematic variation of the expansion conditions.

SUMMARY

The results presented in this chapter show that high resolution SRS can provide useful information on aggregation processes in the jet. The capability to distinguish between different phases of the aggregates is a new and especially useful feature of SRS. Other techniques that were used previously to study condensation in free jets such as elastic light scattering[99] and static pressure measurements[100] do not give information on the phase of the aggregates. Experiments using electron diffraction in free jet expansions[93] allow distinction between solid and liquid phases and make it possible to determine the cluster temperature if the cluster material has crystalline structure and the thermal expansion coefficient of the lattice is known. However, since ED experiments require high vacuum, it is generally necessary to use skimmed molecular beams and probe the aggregates far away from the nozzle. The phase and temperature determined in the ED studies is therefore characteristic of the fully grown cluster which has already cooled by collisions with the cold driving gas and by evaporation and may have undergone several phase transitions before it reached the detection zone. It is therefore very difficult to study the dynamics of the cluster formation and cooling throughout the jet expansion by electron diffraction techniques. High resolution SRS on the other hand makes it possible to probe the aggregates throughout the full range of the expansion, avoiding the complication of skimmer interferences, and to obtain temperatures not only from crystalline but also from liquid and amorphous cluster phases. Tight focusing and the crossing of the laser beams gives SRS high spatial resolution, a desirable feature for beam diagnostic studies that can not be readily achieved with electron beams due to the space charge effects. The high spatial resolution translates into good time resolution for the observation of dynamic processes such as the cluster growth and possible phase transitions that occur during the expansion.

The two methods, electron diffraction and high resolution SRS, therefore complement each other with respect to the information provided by these techniques making further development and application of SRS to the study of large clusters in free jets a desirable and promising goal. It should also be mentioned that the probing is non-intrusive, that is, there is no effect on the condensation process by the Raman probing. In contrast, studies of jet condensations using electron beam fluorescence and other ionization methods to probe temperatures and densities involve the creation of ions which can serve as condensation nuclei and thereby perturb the expansion.

PERSPECTIVE AND FUTURE APPLICATIONS

Obviously, the study of large clusters by SRS should be extended to other molecules. Initial experiments with neat jets of O_2 showed that the condensation product in this case is liquid, as expected, but the freezing of the droplets was not observed in neat expansions. This is not surprising since O_2 has a much larger liquid range (90.1 - 54.4 K) than N_2 (77.4 - 63.2 K). However, solid O_2 is very interesting since it exists in three stable phase in equilibrium with its vapor with phase transitions at 43.8 and 23.7 K. By using a high pressure driving gas such as He or Ne it should be possible to cool the liquid O_2 clusters sufficiently to study clusters of solid O_2

in several solid phases.

CS_2 is another promising molecule for the study of clusters by SRS. Its very large Raman cross section (≅ 20 times larger than for N_2) combined with its narrow vibrational linewidth makes it possible to detect even very small concentrations of CS_2 clusters formed in dilute expansions and under weakly supersatured conditions. It may be possible to study the effect of the increasing surface to volume ratio on the Raman lineshape in more detail than it was done in this thesis for the case of N_2 clusters and gain information on the variation of the vibrational frequency between molecules inside and on the surface of small aggregates.

Finally, H_2 might be an interesting cluster material since the possibility of formation of a superfluid cluster exists in this case which would be very interesting from a theoretical point of view.

It should be noted that the highly supercooled droplets formed in free jet expansions provided access to a region of phase space that can not be studied with equilibrium samples. Vibrational Raman spectroscopy, particularly SRS because of its high resolution, provided valuable probes for studying the dynamics of these systems.

In addition to providing information about the dynamics of condensation processes and phase changes in micro-aggregates, these Raman experiments suggest a number of other potential applications for condensing jets. For example, the production of new, metastable phases may be feasible and the role of impurities in stabilizing these investigated. Novel liquid solute-solvent systems can be formed which would not be stable under equilibrium conditions where the solute would freeze on the walls of a cold solvent container. The use of expansions to obtain Raman matrix isolation spectra is also appealing since the small matrix cluster formed in jets can withstand the high laser powers necessary to take advantage of nonlinear Raman probing techniques such as SRLS and CARS. Such probing is difficult for static samples due to sample heating and optical damage of the matrix films. It may be possible to trap radicals, formed by photolysis in the early stages of the expansion, in large matrix clusters for Raman investigations.

REFERENCES

1. C.V. Raman and K.S. Krishnan, Nature **121**, 501 (1928).

2. E.J. Woodbury and W.K. Ng, Proc. IRE **50**, 2367 (1962).

3. W.J. Jones and B.P Stoicheff, Phys. Rev. Lett. **13**, 657 (1964).

4. P. Lallemand, P. Simova, and G. Bret, Phys. Rev. Lett. **17**, 1239 (1966).

5. I. Reinhold and M.Maier, Opt. Commun. **5**, 31 (1972).

6. B.E. Kincaid and J.R. Fontana, Appl. Phys. Lett **28**, 12 (1976).

7. A. Owyoung and E.D. Jones, Opt. Lett. **1**, 152 (1977).

8. A. Owyoung and P. Esherick, Opt. Lett. **5**, 421 (1980).

9. P. Esherick and A. Owyoung, J. Mol. Spectrosc. **92**, 162 (1982).

10. A. Owyoung, P. Esherick and A.G. Robiette, and R.S McDowell, J. Mol. Spectrosc. **86**, 209 (1981).

11. P.Esherick and A. Owyoung, and C.W. Patterson, J. Phys. Chem. **87**, 602 (1983).

12. B. Lavorel, G. Millot, R. Saint-Loup, C. Wenger, H. Berger, J.P. Sala, J. Bonamy, and D. Robert, J. Phys. **47**, 417 (1986).

13. L.A. Rahn and R.E. Palmer, J. Opt. Soc. Am. B **3**, 1164 (1986).

14. M.D. Morris, in: *Advances in Laser Spectroscopy*, **3**, edited by B.A. Garetz and J.R. Lombardi, (Wiley, New York , 1986).

15. J.P. Heritage, and D.L. Allara, Chem. Phys. Lett. **74**, 507 (1980).

16. C. Sierens, A. Bouwen, E. Goovaerts, M. De Maziere, and D. Schoemaker, Phys. Rev. A **37**, 4769 (1987).

17. R. Kron, M. Baggen, and Ad Lagendijk, J. Chem. Phys. **91**, 74 (1989).

18. P. Esherick and A. Owyoung, Chem. Phys. Lett. **103**, 235 (1983).

19. P. Esherick, A. Owyoung, and J. Pliva, J. Chem. Phys. **83**, 3311 (1985).

20. D.A. King, R.Haines, N.R. Isenor, and B.J. Orr, Optics Lett. **8**, 629 (1983).

21. W. Bronner, P. Oesterlin, and M.Schellhorn, Appl. Phys. B **34**, 11 (1984).

22. N. Bloembergen, Nonlinear Optics (Benjamin, New York, 1965)

23. W.J. Jones, in: *Non-linear Raman Spectroscopy and Its Chemical Applications*, W. Kiefer and D.A. Long, eds. Series C, Vol 93 (Reidel, London, 1982) p. 473.

24. W.J. Jones, in: *Advances in Non-linear Spectroscopy*, Vol. 15 R.J.H. Clark and R.E. Hester, eds. (Wiley, New York, 1988) ch.2.

25. J.W Nibler and G.A.Pubanz, ibid, ch.1.

26. J.W. Nibler, *Quantum Mechanical Derivation of* $\chi^{(3)}$, paper presented at Nato Advanced Study Institute on Nonlinear Raman Spectrocopy, Bad Winsheim, West Germany 1982, unpublished.

27. M.D. Levenson and S.S. Kano, *Introduction to Nonlinear Laser Spectroscopy* (Academic Press New York 1988).

28. J.A Gordmaine and W.Kaiser, Phys. Rev. **144**, 676 (1966).

29. D.W Oxtoby, Adv. Chem. Phys. **40**, 1 (1979); Adv. Chem. Phys. **48**, 487 (1981).

30. R. Kubo, in: *Fluctuations, Relaxation, and Resonance in magnetic systems*, D. ter Haar, ed. (Plenum, New York, 1962).

31. J.O. Barnason, B. Hudson, and H.C. Andersen, J. Chem. Phys. **70**, 4130 (1979).

32. E. Fermi, Rev. mod. Phys. **4**, 105 (1932).

33. D. Cope, R. Khoury, and R.J. Lovett, J.Quant. Spectrosc. Radiat. Transfer, **39**, 163 (1988).

34. R.H. Dicke, Phys. Rev. **89**, 472 (1953).

35. L. Galatry, Phys. Rev. **122**, 1218 (1961).

36. S.G. Rautian and I.I. Sobelman, Sov. Phys. Usp. **9**, 701 (1967).

37. G. Millot, B. Lavorel, R. Saint-Loup, and H. Berger, J. Phys. **11**, 1936 (1985).

38. P.W. Anderson, J. Phys. Soc. of Japan **9**, 316 (1954).

39. K.S. Schweitzer and D. Chandler, C. Chem.Phys. **76**, 2296 (1982).

40. M.J. Clouter and H. Kiefte, J. Chem. Phys. **66**, 1736 (1977).

41. H.J. Van Elburg and J.D.W. Van Voorst, Chem. Phys. **113**, 462 (1987).

42. S.A. Akhmanov, F.N. Gadjiev, N.I. Koroteev, R.Yu. Orlov, and I.L. Shumay, Appl. Optics **19**, 859 (1980).

43. W.G. Rotshild, J. Chem. Phys. **65**, 455, 2958 (1976).

44. J.C. Decius and R.M. Hexter, *Molecular Vibrations in Crystals* (McGraw-Hill, New York, 1977).

45. S. Califano, V. Schettino, and N. Neto, *Lattice Dynamics of Molecular Crystals*, G. Berthier ed. (Springer, Berlin, 1981).

46. S. Califano and V. Schettino, Int. Rev. in Phys. Chem. **7**, 19 (1988).

47. R.J. Elliott, in: *Lattice Dynamicsand Intermolecular Forces*, Proceedings of the LV International School in Physics (Academic Press, New York 1975).

48. R.M Hochstrasser and S. Velsko, J. Phys. Chem. **89**, 2240 (1985).

49. J. Klafter and J. Jortner, J. Chem. Phys. **68**, 1513 (1978).

50. I.I. Abram, R.M. Hochstrasser, J.E. Kohl, M.G. Semack, and D. White, J. Chem. Phys. **71**, 153 (1979).

51. L.A. Rahn, R.L. Farrow, M.L. Koszykowski, and P.L.Mattern, Phys. Rev. Lett. **45**, 620 (1980).

52. R.L. Farrow and L.A. Rahn, Phys. Rev. Lett. **48**, 395, (1982).

53. P. Huber-Wälchli and J.W. Nibler, J. Chem. Phys. **76**, 273, (1982).

54. J.J. Valentini, P. Esherick, and A. Owyoung, Proc. SPIE-Int. Soc. Opt. Eng., **288**, 288 (1981).

55. *Structure and Dynamics of Weakly Bound Complexes,* NATO ASI Series Vol. C212, Alfons Weber ed. (Reidel, Dordrecht, 1986).

56. D.H. Levy, Ann. Rev. Chem. **31**, 197 (1980).

57. H.W. Liepmann and A. Roshko, *Elements of Gas Dynamics* (Wiley, New York, 1957).

58. H. Ashkenas and F.S. Sherman,: in Rarefied Gas Dynamics, Fourth Symposium, Vol. 2, J.H de Leeuw ed. (Academic Press, New York, 1965).

59. G. Koppenwallner and C. Dankert, J. Chem. Phys. **91**, 2482, (1987).

60. P.P. Wegener *Naturwissenschaft* **74**, 111 (1987).

61. C. Düker and G. Koppenwallner in Rarefied Gas Dynamics Pt.2, p.1190 Twelfth Symposium (Academic Press, New York, 1980).

62. C. Dankert DFVLR-IB 252-77 H10, 1977.

63. G.A. Pubanz, Ph.D. Thesis Oregon State University (1987).

64. W.D. Fountain, IEEE J. of Quant. Electronics **18**, 432 (1982).

65. P. Drell and S. Chu, Opt. Commun. **28**, 343 (1979).

66. P. Esherick and A. Owyoung, in: *Advances in Infrared and Raman Spectroscopy*, R.J.H. Clark and R.E. Hester eds. Vol.9 (Heyden, New York, 1982).

67. R.K. Khanna, M.A. Perera-Jarner, and M.J. Ospina, Spectrochimica Acta **3**, 421 (1987).

68. V.G. Kunde, A.C. Aikin, R.A. Hanel, D.E. Jennings, W.E. Maguire, and R.E. Samelson, Nature **292**, 683 (1981).

69. K.W. Brown, J.W. Nibler, K.Hedberg, and L.Hedberg, J. Phys. Chem. **93**, 5679 (1989).

70. J. Chesnoy, Chem. Phys. Lett. **125**, 267 (1986).

71. J. Chesnoy and J.J Weis, J. Chem. Phys. **84**, 5378 (1986).

72. A.S. Zinn, D. Schiferl, and M.F. Nicol, **87**, 1267 (1987).

73. H.J. Jodl and F. Bolduan, J. Chem. Phys. **76**, 3352 (1982).

74. H.W. Loewen, H.J. Jodl, A. Loewenschuss, and H. Däufer, Can. J. Phys. **66**, 308 (1987).

75. W. May, H. Kiefte, M.J. Clouter, and G.I Stegeman, Appl. Optics **17**, 3352 (1978).

76a. M. Scotto, J. Chem. Phys. **49**, 5362 (1968).

76. R. Ouillon, P. Ranson, and S. Califano, Chem. Phys. **73**, 673 (1984).

77. A. Lauberau, Chem. Phys. Lett. **27**, 600 (1974).

78. M.J. Clouter and H. Kiefte, J. Chem. Phys. **73**, 673 (1980).

79. M.J. Clouter and H. Kiefte, Chem. Phys. Lett. **70**, 425 (1980).

79a. T.A. Scott, Physics Reports **27**, 89 (1976).

80. R. Beck and J.W. Nibler, Chem. Phys. Lett. **159**, 79 (1989).

81. C.H. Wang and R.B. Wright, J. Chem. Phys. **59**, 1706 (1973).

82. G. Zumhofen and K.Dressler, J. Chem. Phys. **67**, 3659 (1977).

83. M.M. Thiery and D. Fabre, Mol. Phys. **32**, 257 (1976).

84. A. Anderson, T.S. Sun, and M.C.A. Donkerslot, Can. J. Phys. **48**, 2265 (1970).

85. I.R. Beattie, T.R. Gilson, S.N. Jenny, and S.J.Williams, Nature **297**, 212 (1982).

86. H. Kiefte, M.J. Clouter, N.H. Rich, and S.F Ahmad, Can. J. Phys. **60**, 1204 (1982).

87. G.A. Ozin, in: Vibrational spectroscopy of trapped species, H.E. Hallam, ed. (Wiley, New York, 1973) ch. 9.

88. G.A Pubanz, M. Maroncelli, and J.W. Nibler, Chem. Phys. Lett. **120**, 313 (1985).

89. C.L. Briant, and J.J Burton, J. Chem. Phys. 63, **2045** (1975).

90. T.L. Beck, J.Jellinek and R.S. Berry, J. Chem. Phys. **87**, 545 (1985).

91. A.W. Castleman Jr. and R.G. Keese, Chem. Rev. **86**, 589 (1986).

92. A collection of review articles on gas phase clusters can be found in Chem. Rev. **86** (1986) .

93. L.S Bartell, ibid. p.491

94. B.Lavorel, R.Chaux, R. Saint-Loup, and H. Berger, Opt. Commun. **62**, 25 (1987).

95. S. Gerstenkorn and P. Luc Atlas du Spectre d'Absorption de la Molecule D'Iode (Editions du C.N.R.S., Paris 1978) and S.Gerstenkorn and P. Luc, Rev. Phys. Appl. **14**, 791 (1979).

96. M. Born and E. Wolf, Principles of Optics (Pergamon Press, Oxford, 1975) p.656.

97. M.J. Clouter, H. Kiefte, and R.K. Jain, J. Chem. Phys. **73**, 673 (1980).

98. A.D. May, G. Varghese, J.C Stryland, and H.L Welsh, Can. J. Phys.

42, 1058 (1964).

99. S.S Kim, D.C. Shi, G.D. Stein, Rarefied Gas Dyn. **2**, 1211 (1980).

100. W.D. Williams, J.W.L. Lewis, AIAA J. **13**, 709 (1975).

101. J.P Borel and A. Chatelain, Helvetica Physica Acta **58**, 443 (1985).

102. P.Pavlov, Z. Phys. Chem. **65**, 1 (1909); **65**, 545 (1909).

APPENDICES

APPENDIX A: THE RING DYE LASER

The tunable laser in the SRS spectrometer is a Coherent 699-29 ring dye laser pumped by a multi-line Argon ion laser. The unidirectional ring cavity allows efficient conversion of high pump power since *spatial hole burning* does not occur in a traveling wave cavity. This hole burning effect is a serious problem in linear cavity designs where the standing wave which builds between the end mirrors depletes the gain in the active medium only in regions of high electric field. At the nodes of the standing light wave a large population inversion can build up and support cavity modes at frequencies different from the initial mode. Since the different modes are not competing directly for the same gain single mode operation becomes problematic and even impossible at high pump power.

In the ring cavity design (see Fig. A.1) traveling wave operation is achieved by including an *optical diode* in the cavity. This element uses two effects - Faraday rotation and optical activity. *Faraday rotation* is a polarization rotation in a medium with nonzero Verdet constant when placed in a dc magnetic field. The direction of the rotation depends only on the direction of the magnetic field but not on the direction of travel of the wave. *Optical activity* is a polarization rotation in an optically anisotropic crystal for which the rotation direction does depend on the direction of the light. The two effects cancel each other for a wave traveling through it in one direction but cause a rotation of a linearly polarized wave in the

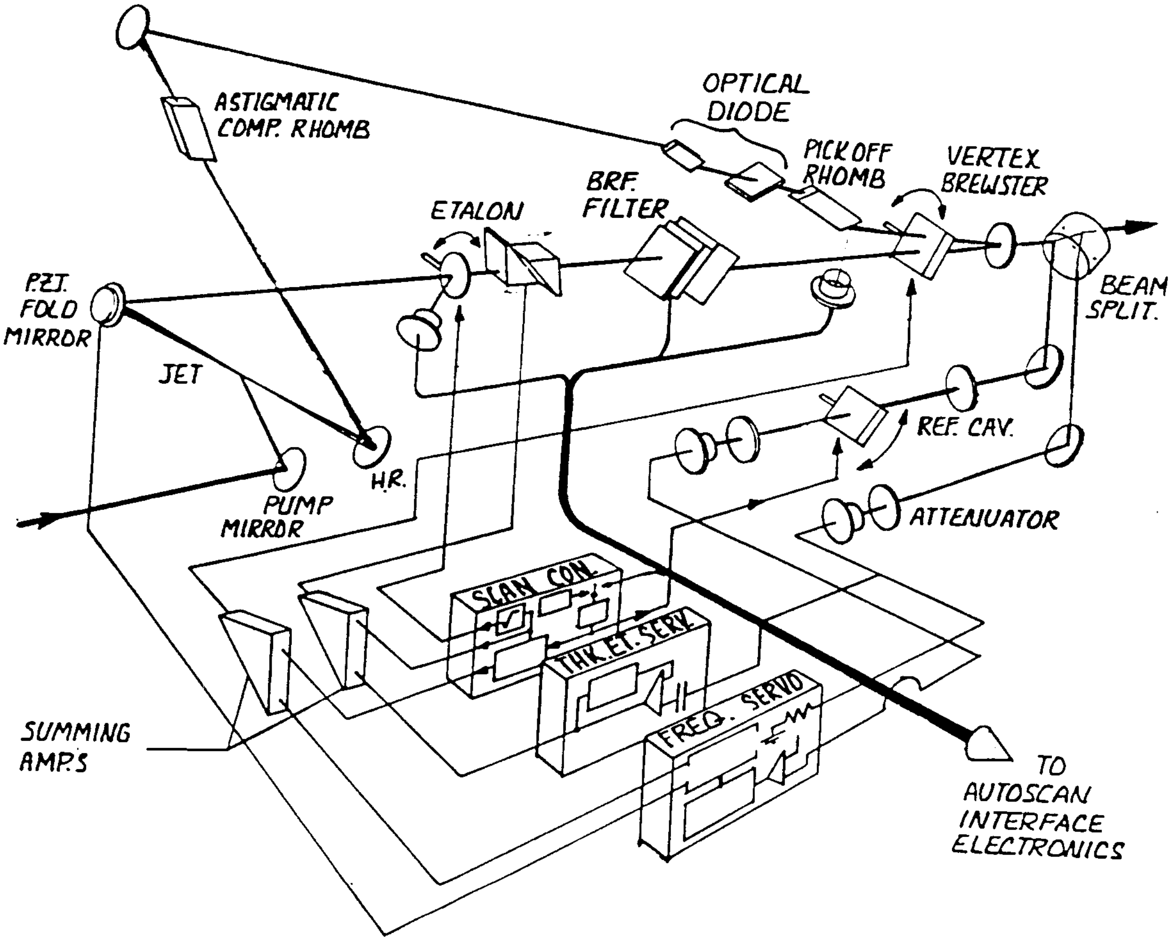

Figure A.1: Schematic of optical and electronic layout of the ring laser (Coherent). The optical elements of the laser and the sensors with the connections to the controlling electronics are shown.

opposite direction. The rotated wave experiences higher reflection losses at the Brewster surfaces in the cavity and does not reach the lasing threshold.

The three filter elements which force the laser to lase on a single longitudinal cavity mode are: (1) a three plate birefringent filter with a free spectral range (FSR) 380 GHz, (2) a solid thin etalon with 225 GHz FSR, and (3) a solid thick etalon with 10 GHz FSR. Fig. A.2 shows how single frequency operation is achieved through the combined bandpass of these elements. The instantaneous linewidth of the laser is only a few Hertz but because of cavity length fluctuations caused by mechanical and acoustic perturbations and fluctuations in the dye jet the frequency of the unstabilized laser would jitter within an effective linewidth for about 20 MHz. To reduce this jitter the laser frequency is locked to a resonance of a temperature stabilized confocal Fabry Perot reference cavity (1 GHz FSR). The length of the ring cavity can be adjusted with a folding mirror mounted on a piezoelectric crystal and also, over a wider range, with a vertex mounted rotating Brewster plate. Two feedback loops, one with good high frequency response (< 10 KHz) adjusting the piezo mirror and a low frequency circuit (< 120 Hz) with large dynamic range, tilting the Brewster plate, keep the laser frequency always at the inflection point of the reference cavity transmission pattern.

If a perturbation is strong enough to saturate the feedback loops the laser could mode-hop to a different cavity mode. To ensure that the laser will recover to the same locking point on the repetitive reference cavity transmission pattern, the FSR of the thick etalon, of

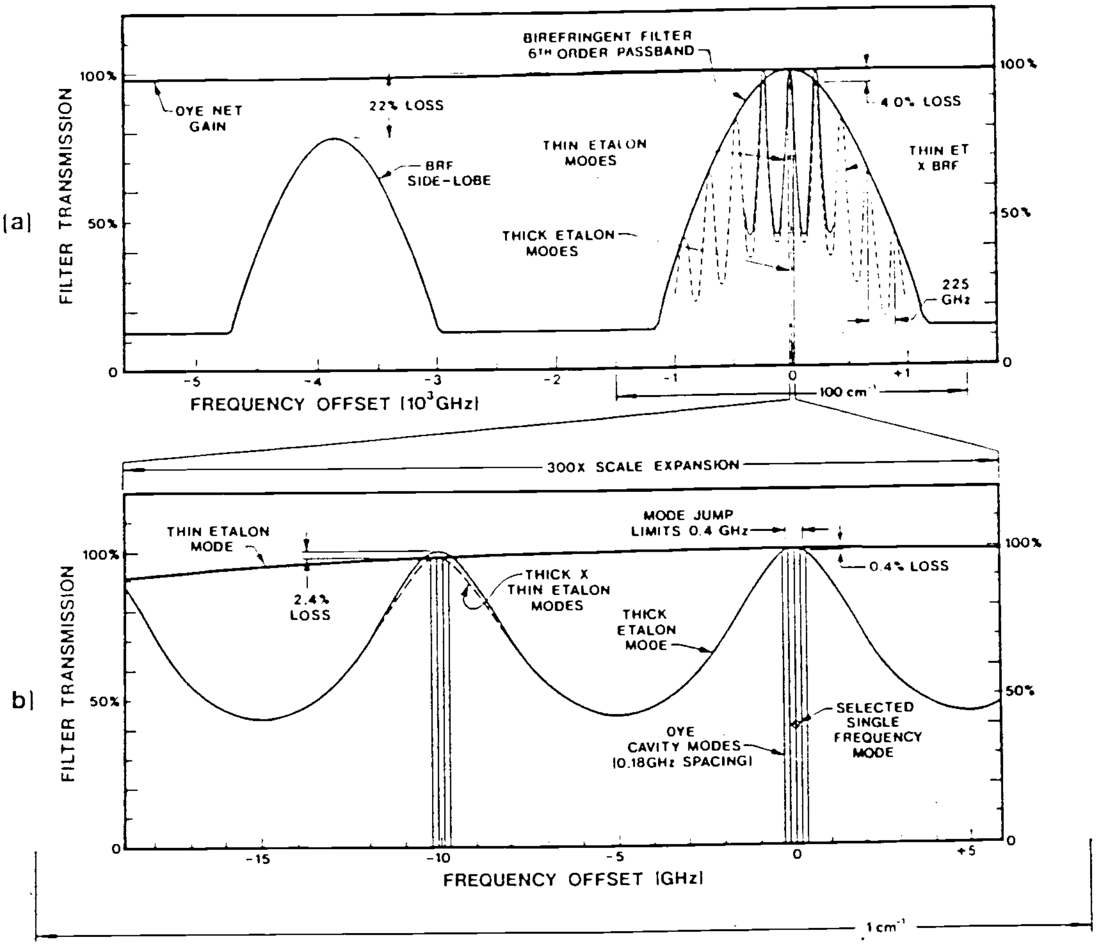

Figure A.2: Transmission of the filter elements in ring cavity.

a) Dye gain curve, birefringent filter BRF, thin etalon

b) Thin etalon, thick etalon, cavity modes the reference cavity, and the cavity mode spacing are chosen so that there is only one locking point within the mode jump limits imposed by these filter elements (see Fig. A.3). This Autolock^{TM} is an important feature if one uses the dye laser output to seed a pulsed amplifier where feedback from the amplifier can disturbed the seed laser. We found that, because of the re-locking feature, it was not necessary to use a Faraday isolator between the seed laser and the amplifier since the 100 msec between the perturbations caused by the 10 Hz pulsed amplifier are sufficient time for the seed laser to recover lock.

The scanning of the ring laser is done by tilting a Brewster plate inside the reference cavity and thereby moving the lock point in frequency. The servo loops controlling the Brewster plate in the ring cavity and the piezo mounted "tweeter" mirror will cause the laser to follow the lock point. In order to avoid mode hops the etalons need to be adjusted as well so that their transmission pattern moves with the laser frequency. The thick air spaced etalon contains piezo elements which are used to shift its transmission peaks. Supplying a 2 KHz sinusoidal voltage to the PZT elements causes a low level amplitude modulation of the laser light. This signal is monitored with a phase sensitive detector which yields an error signal that is used to keep the etalon transmission maximum peaked on the laser frequency. The thin etalon is not moved during a scan but the computer adjusts its angle at the beginning of each scan segment to maximize the transmission of the etalon.

The laser can be scanned continuously in this way for up to 40

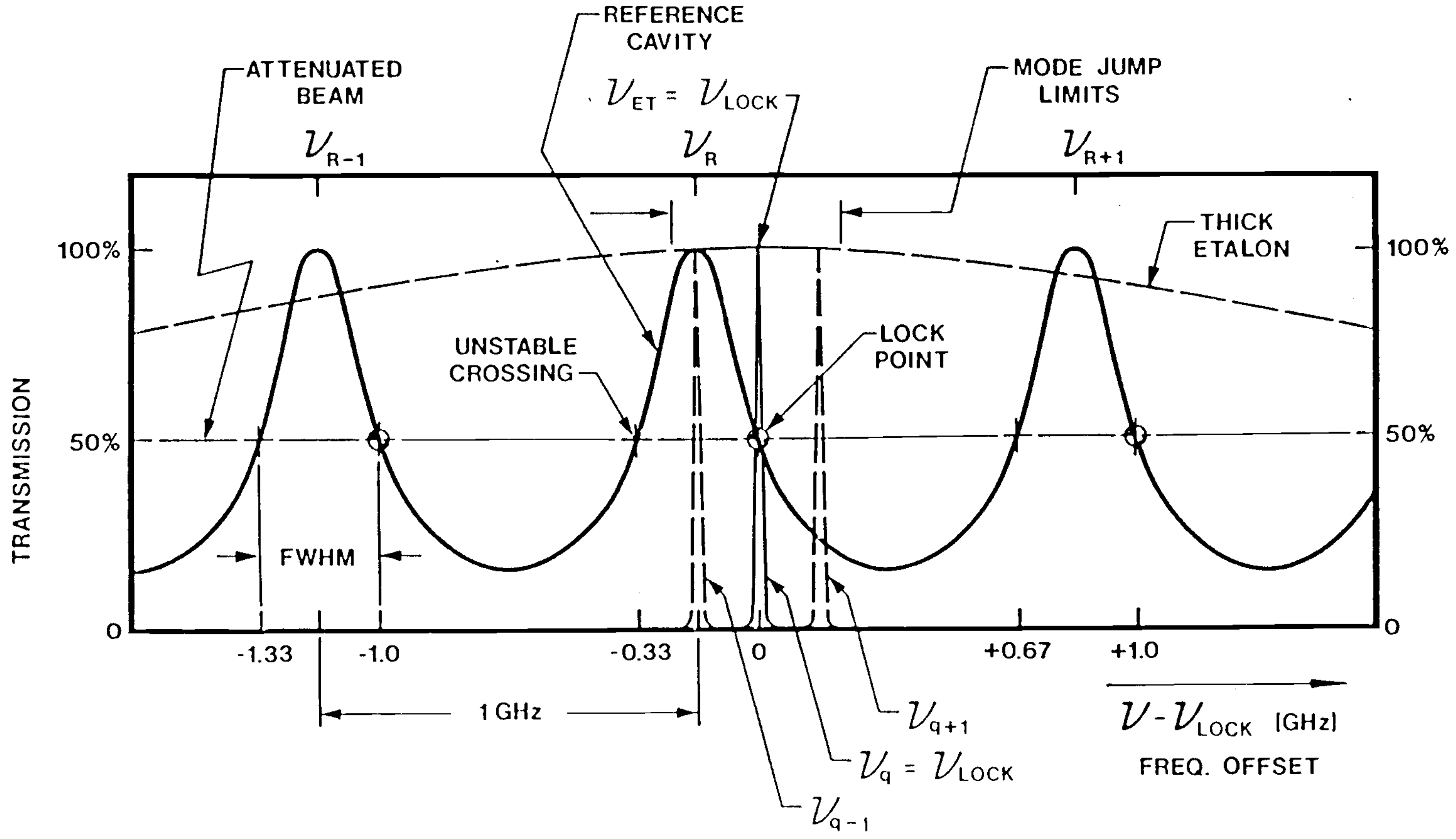

Figure A.3: Autolock^{TM} design of the Coherent ring laser. Only one stable lockpoint to the reference cavity transmission exists within the modejump limits determined by the cavity mode spacing and the thick etalon.

Hz limited only by the tilt range of the Brewster plate. Longer scans are done in 10 GHz pieces under computer control where the Apple micro computer uses the wavemeter to position the starting points of each 10 GHz interval and also controls the thin etalon with a galvo tilt mechanism and the birefringent filter through a stepper motor. Fig. VII.4 shows the sequence of events during the scanning operation.

APPENDIX B: THE WAVEMETER

The wavemeter is an integral part of the Coherent ring laser and provides the frequency calibration. Fig VII.5 shows a schematic of the optical layout of the wavemeter. Because the precision of the Raman data acquired with the stimulated Raman spectrometer crucially depends on the wavemeter, its function and limitations will be explained in some detail in the following paragraph.

In order to determine the absolute frequency of the ring laser within the dye tuning range with an accuracy of $4\cdot10^{-7}$ or 200 MHz the wavemeter consists of two separate parts - the OAM and the VET.

The VET (*vernier etalon*) consists of two vacuum spaced low finesse etalons, made of Zerodur and held in a temperature stabilized housing, which have a FSR of 6.5 GHz and 6.8 GHz. Because of this difference in the FSR the transmission peaks of the two etalon will coincide about every 150 GHz or the repeat range of the "vernier". Within this repeat range, that is within one "VET order", the frequency is uniquely determined by the spacing between two adjacent VET peaks - one peak from the longer etalon and one from the shorter one.

The OAM (*optical activity monochromator*) is used to determine the VET order. The known wavelength dependence of the polarization rotation for linearly polarized light in a quartz crystal is used to measure the wavelength of the light. The rotated light passes through a spinning polaroid wheel and is detected with a photodiode. The computer measures the rotation angle from the phase shift between the photodiode signal and a reference signal produced by the spinning

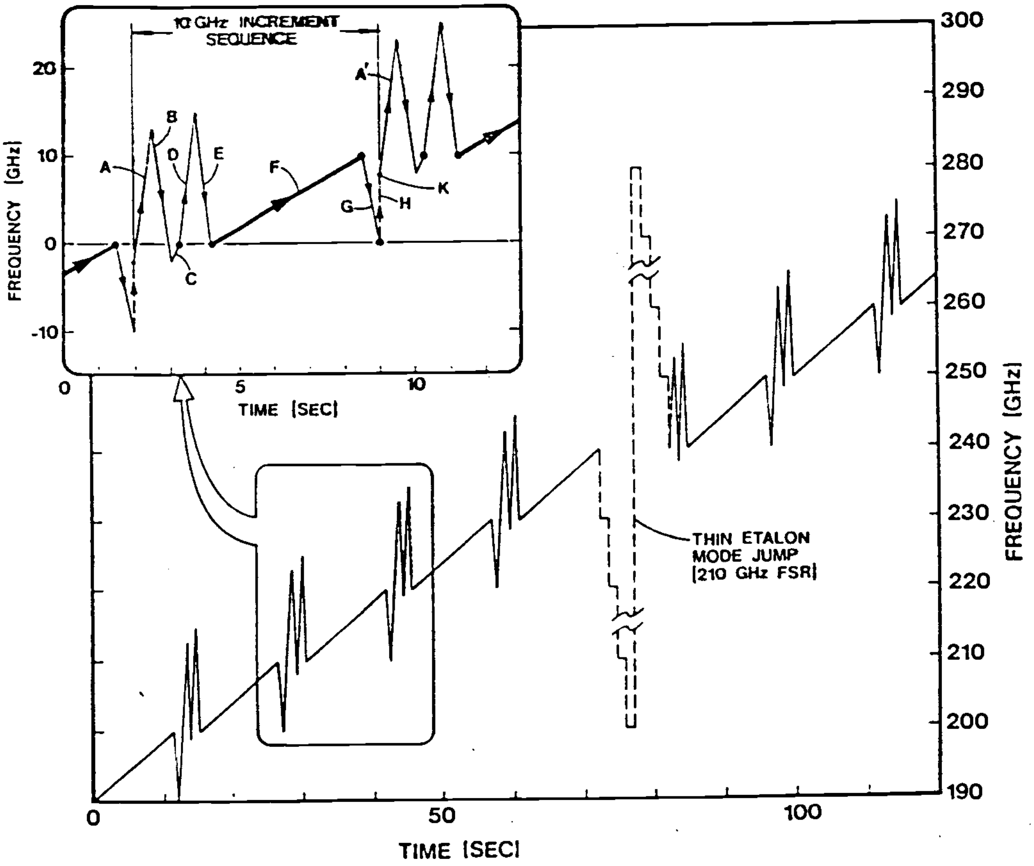

A - Scan to find starting position
B - Retrace
C - Compute and set start of scan
D - Scan to check start position
E - Retrace
F - 10 GHz data scan
G - Retrace
H - Thick etalon mode jump (≅ 10 GHz)
K - Move thin etalon and BRF to maximize transmission
A'- Next scan to find starting position, etc.

Figure B.1: Sequence of events during a computer controlled scan.

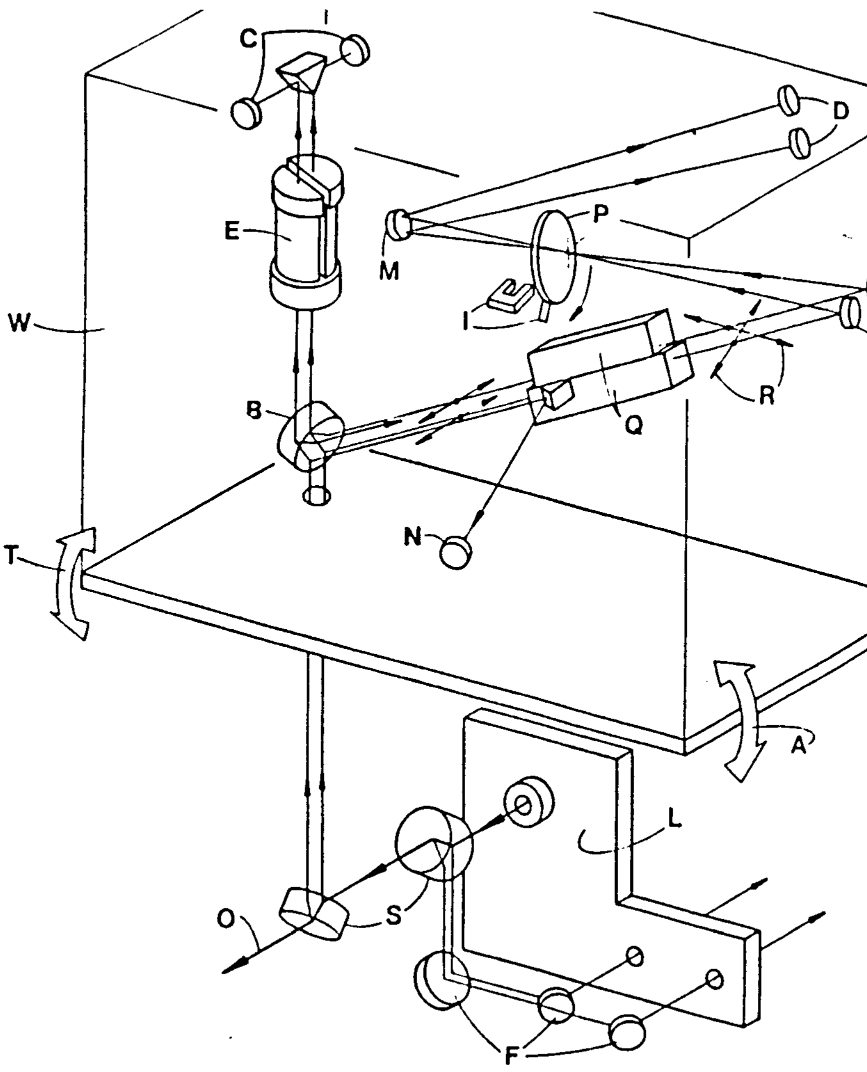

A - Wavemeter tilt adjust (longitudinal)
B - Brewster-angle polarization beamsplitter
C - Detectors for channels 1,2 of the VET
D - Detectors for channels 1,2 of the OAM
E - Vernier etalon assembly (VET)
F - Fold mirrors delivering beams to the frequency servo
I - Flag locating the orientation of polarizer wheel
L - Output endplate of CR-699-21 dye laser
M - Fold mirrors delivering beams to OAM
N - Detector for intensity normalization in the wavemeter
O - Laser output beam
P - Spinning polaroid wheel
Q - Crystalline Quartz bars cut with z-axis along the beam
R - Arrows indicating rotated polarization vectors
S - 45° incident beamsplitter (2 places 0.7% each beam)
T - Wavemeter tilt adjust about transverse axis
W - Wavemeter package mounted on the tilt plate

Figure B.2: Optical layout of the wavemeter (Coherent) wheel. In this way and with signal averaging the rotation angle can be determined to ±0.05. Here the vernier principle is used again. In order to achieve sufficient precision a long (10 cm) piece of quartz is needed. The polarization rotates by about 2000 degrees and the "order" of the rotation in units of 180 degrees is determined from a second piece of quartz which is longer by 4 mm. The additional rotation caused by these 4 mm is always less then $180^\circ$and unambiguously determines the OAM order.

The wavemeter is read by scanning the laser over more than one FSR of the shorter etalons (6.8 GHz) and the transmission fringes are recorded in computer memory. A digital filter program is then used to find the extrema in the fringe pattern and to compute the spacing of the peaks for the two VET channels (and thus the location of the laser frequency within the vernier order) and the fractional order of one of them (giving the exact frequency to 1 % of a free spectral range).

The computer determines the VET order with the OAM by comparing the measured polarization rotation with a "look-up" table stored in computer memory. This table contains, labeled by the OAM order, the constants of a polynomial relating the specific rotation ρ (degrees per mm quartz) to $1/\lambda$. These constants are determined during the calibration of the wavemeter with known spectral lines of I_2 and U.

In conclusion, the wavemeter allows the dye laser frequency to be determined with 200 MHz absolute accuracy and provides a frequency axis for the scans with a maximum error of 60 MHz due to nonlinearity within each 10 GHz segment. Therefore the maximum cumulative error in even the longest scan is less than 260 MHz or 0.009 cm^{-1}.

APPENDIX C: RING DYE LASER ALIGNMENT PROCEDURE

The following alignment procedure is based on the instruction given in the laser manual. Some changes and additions are made based on the experience gained from the Coherent user training and the operation of the laser during the research described in this thesis.

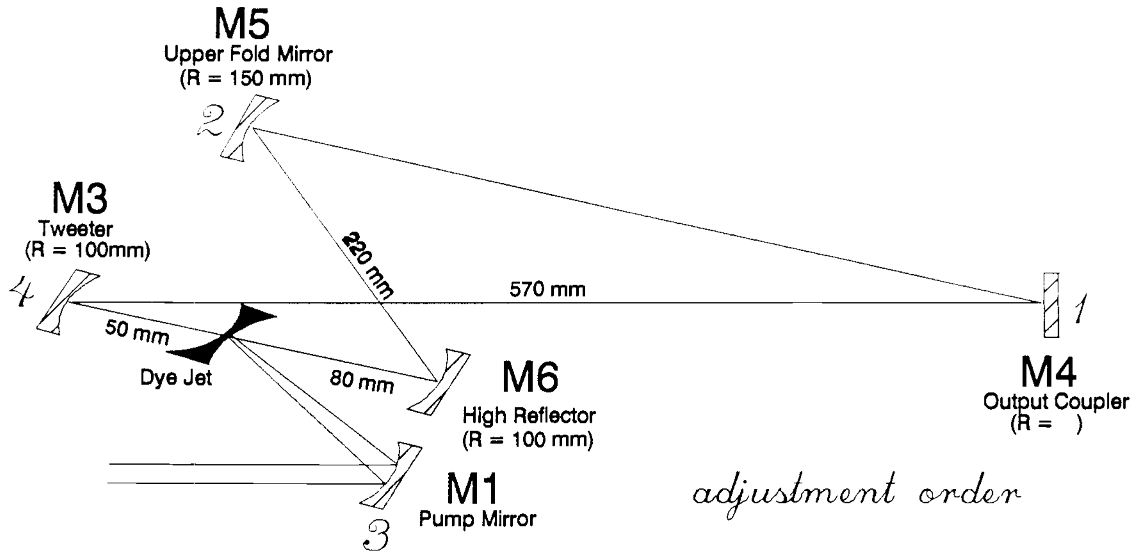

Fig. C.1: Beam path diagram of optical cavity (Coherent)

Broadband Alignment

- Dye concentration: adjust for 80 % absorption of pump beam. This can be measured by inserting a small mirror into the cavity to reflect the pump beam into a power meter after it passes through the dye jet. Measure power with jet on and off and calculate absorption.

- Dye recipe for R590: all lines pumping requires more concentrated dye than 514.5 nm pumping. 1.2 g of R590 dissolved in 50 ml MeOH. Fill pump reservoir to 6 mm below return hose inlet.

- Align pump beam; take out pump fold mirror, lower fold mirror, ICA, BRF, Brewster plate and align pump laser so that the beam is centered in the entrance aperture and the alignment hole below the output coupler.

- Check dye jet alignment (see jet alignment procedure) skip this step if you know that the jet alignment hasn't been disturbed.

- Position high reflector (M6) so that it is 80 mm from the pump focus in the dye jet by moving M6 with all 3 hex screws.

- Move pump mirror (M1) with its vertical and horizontal translation controls so that pump beam hits the pump mirror slightly high and in the center of the U-shaped aperture. (see Fig. C.2) Rotate the mirror mount so that the pump beam hits the aperture plate one spot diameter above the tweeter aperture and pump focus is centered in the dye jet. (see Fig. C.3)

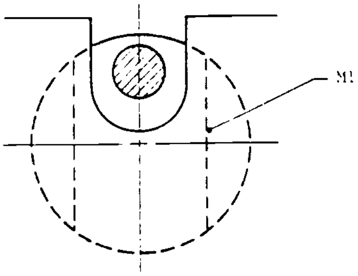

Fig. C.2 Position of pump beam on pump mirror.

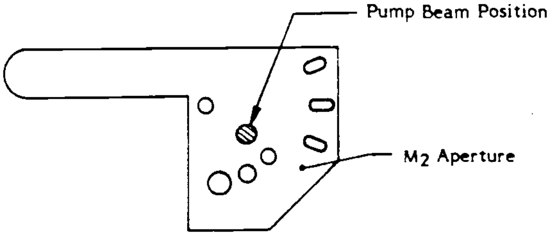

Fig. C.3 Position of pump beam on aperture plate.

- Move lower fold mirror (M6) so that fluorescence spot on upper fold mirror (M5)is slightly above center. (see Fig. C.4)

(Move M5 on its invar finger so that the spot size at the magnet assembly is about 4-5 mm diameter and the tweeter mirror so that the spotsize is about 1.5-2 mm at the magnet assembly.

- Move M5 so that the spot on the output coupler is centered in the aperture defined by the image through the magnet assembly (see Fig. C.5)

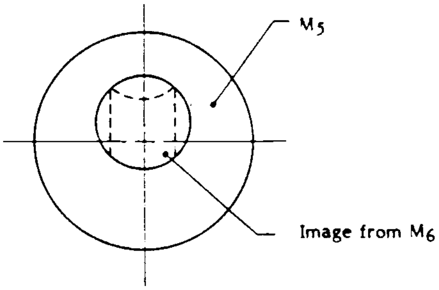

Fig.C.4 Image on upper fold mirror.

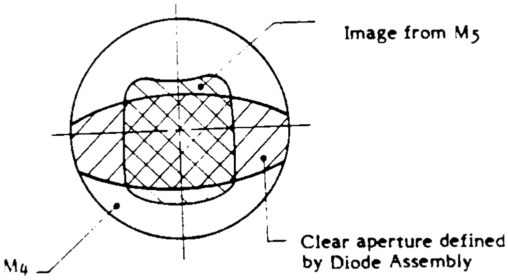

Fig. C.5 Image on output coupler.

- Move tweeter mirror M3 so that the small spot is centered in the larger spot from M5. (see Fig. C.6 "cateye")

- Move output coupler M4 so that the small spot is above the larger fluorescence spot on M5. (see Fig. C.7)

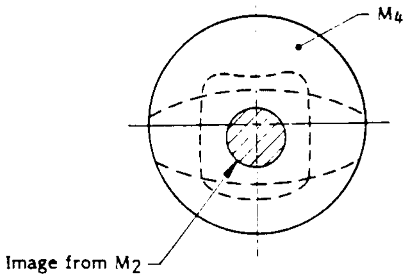

Fig. C.6 "Cateye" image on output coupler.

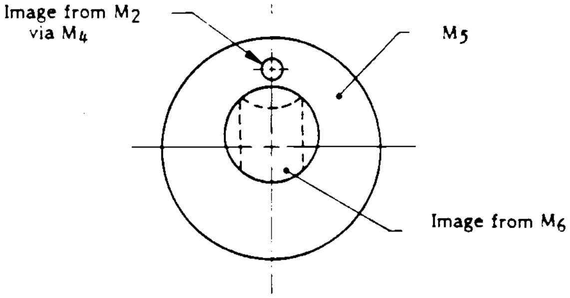

Fig. C.7 Image on upper fold mirror.

- Rock M4 vertically and watch for lasing on a card outside the cavity.

- If no lasing is observed look at the transmitted spot (through M4) while rocking M4 vertically and adjust M4 horizontal control until the moving spot is in a vertical line with the stationary one and the two spots are superimposed at one particular position of M4.

- If still no lasing is seen scan M5 vertical adjustment while rocking M4 vertically.

- If still not lasing scan M5 vertical control slowly while rocking M4 vertical. As the fluorescence spot that moves with M4 passes through the upper stationary spot, watch for the appearance of a third dim spot in the same area. Using M4 horizontal control to align the stronger moving spot and the M5 horizontal control to align the weaker moving spot bring both spots into one vertical line with the stationary spot. Rock M4 vertically and scan M5 vertically until the laser flashes. Establish continuous lasing with M4 vertical control.

- If the laser does not lase check that nothing is obstructing the beam path in the cavity, check focal points, pump laser power and dye mixture.

- Tweak all mirror positions for power. Cycle through the vertical adjustments in the order: M4, M5, M3, M6. Then adjust the horizontal controls in the same order. Repeat this cycle until no further increase in power can be gained. Using a photo diode instead of a power meter speeds up this process, but insure that the beam does not get steered off the diode.

- Install the BRF. To get lasing, adjust only the vertical control of the tweeter mirror while rocking the output coupler.

- If power or mode quality are unsatisfactory the following adjustment might help:
    translate pump focus
    translate tweeter mirror M3
    translate upper fold mirror M5
- Moving M1 towards the jet increases power and flattens the mode
- Moving M1 away from the jet decreases power and vertically elongates the mode.
- Moving M3 and M5 towards the jet horizontally elongates the mode and

increases the beam diameter.

- Moving M3 and M5 away from the jet vertically elongates the mode and increases the beam diameter.

These adjustments are listed in order of decreasing effect on power and mode. After each adjustment is made it is necessary to go through the "tweaking cycle".

- Reference value for output power in broad band operation: 1100 mW at $\cong$ 17100 cm^{-1} with 6 W pump power.

Jet Alignment Procedure

- Insure that pump beam is properly aligned.

- With the dye laser lasing take the magnet assembly off its holder and observe the reflections off the jet on the ceiling. If there are two separate spots move the jet vertically to overlap the two spots completely. An interference pattern will appear when the two spots are overlapped.

- Move the overlapped spots onto the axis of the dye laser by pointing the jet up or down. compensate with vertical movement to keep the pump focus in the center of the jet.

- Adjust the Brewster angle by rotating the nozzle assembly with a wrench until the reflected spot has minimum intensity. It may be necessary to slightly loosen one of the pointing screws in order to rotate the nozzle.

- Check that the dye jet is perpendicular to the lasing axis and move it if necessary with the pointing screws.

- To move the jet up loosen the two screws at the top and tighten the two bottom screws. (see Fig. C.8)

- To point the jet down loosen the top pointing screw (at about 1 o'clock position (Brewster angle orientation) and tighten the bottom screw. (at about 7 o'clock position)

- To point the jet horizontally use the other two screws

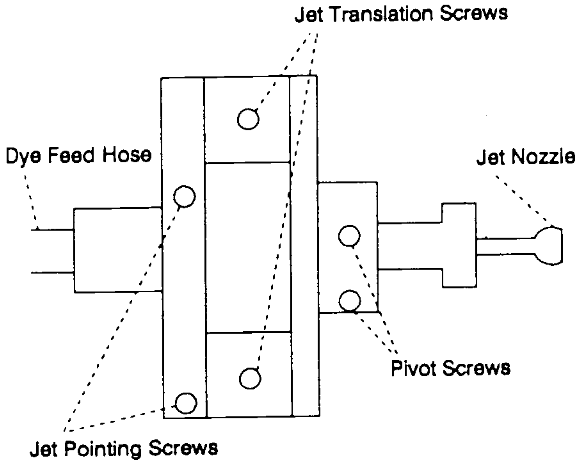

Figure C.8: Jet alignment controls

Single Frequency Alignment

Inserting the ICA:

- Put ICA in cradle and overlap the thick etalon spots using horizontal and vertical adjustments. (see Fig.C.9)
- If it lases - great, if not proceed until lasing is observed:
- Flash thin etalon (to locate reflected spots rock thin etalon by hand, the spots might be way off). Remember that laser has to be in zero servo mode during these steps)
- Scan thick etalon spots again while watching for lasing
- Scan vertical tweeter control while rocking output coupler vertically (back it off first)
- After lasing is established walk thick etalon spots horizontally about 3 spot diameters.
- Plug in thin etalon drive and adjust thin etalon flash in zero servo with the thin etalon control knob all the way counter clockwise but not in detend position. Then switch to detend position.
- Install scanning Brewster plate. Reestablish lasing, if necessary, by adjusting the vertical tweeter control while rocking the output coupler vertically.

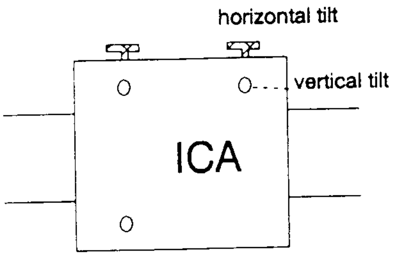

Figure C.9: Intracavity etalon assembly controls.

Reference Cavity Alignment

The reference cavity alignment is well described in the Autoscan manual in section 5.3.3.4. However, there is one neat trick to get the cavity axis aligned precisely along the laser beam which is not given in the manual:

With the laser beams properly centered in the apertures of the reference cavity holder, insert the reference cavity into its cradle. Observe the reflections from the cavity mirrors on the 1/2 inch fold mirror. There should be two reflection one from each end mirror of the reference cavity. If there is only one spot they might be overlapped. Tilt the cavity slightly by lifting at one end and see if the two spots separate. If there is only one spot it is likely that on of the reflections doesn't get through the opening in the reference cavity housing. In this case align the tilt of the cavity, or the beams so that one can see two spots that are superimposed and from a striped interference pattern on the fold mirror. Adjust the four hex screws to maximize the spacing between the interference pattern until you see only one dark line. Now connect the detector block and switch the laser to internal scan and zero servo. Observe the transmission pattern on the monitor screen. If the alignment is close to perfect, every other mode in the transmission pattern should be smaller. Adjust the hex screws in order to minimize these smaller peaks. once this position is reached use one of the steering screws in the mount of the 1/2 inch fold mirror to tilt the beam very slightly off to one side. The transmission peaks should be symmetric again.

The physics behind this procedure is the following: A confocal Fabry Perot interferometer has a cavity mode spacing of c/2L for the longitudinal modes. Since all even transverse modes coincide in frequency and all odd transverse modes also coincide but with a separation between even and odd modes of c/4L the observed mode spacing is c/4L. If the laser beam enters the F.P. exactly on axis it will only excite symmetric (even) modes. In this alignment there is very little energy in the asymmetric cavity modes. Therefore minimizing every other mode in the transmission pattern of the confocal F.P. is a sensitive way to align the F.P axis with the laser axis. This alignment is important because during the scan the laser beams move very slightly. In the "on-axis" alignment the transmission pattern of the F.P. is the least sensitive to this steering of the beam, which results in the most stable locking to the reference cavity. The slight misalignment introduced at the end of the procedure avoids feedback into the ring cavity through back reflections.

APPENDIX D: MODIFICATIONS OF THE AUTOSCAN PROGRAM

The original Autoscan program (version 2.0) was modified by Chris Walker to allow digital data averaging by the Apple computer. During a scan in the original program the laser frequency is changed continuously at a rate determined by the speed command. The slowest scan speed possible is 1000 sec/10 GHz. During the scan the computer takes data by digitizing the input present at the three data channels at certain time intervals. The timing of this data taking is not at equal time intervals, but adjusted in a way to compensate for nonlinearities in the Brewster galvo drive. In order to average several shots in a pulsed experiment the laser has to scan slowly enough that the laser frequency doesn't change significantly compared to the 100 MHz resolution during the averaging time. This mode of operation is less than ideal if a large number of datapoints should be averaged. The modified program (Autoscan2) stops the scan at each data position and digitizes the signal from n lasershots (n must be a power of 2). The data taking is triggered by a signal input through the game port of the Apple computer. After n measurements are taken the arithmetic average is calculated and stored in memory. The laser frequency is then moved to the next datapoint and the process is repeated. The time required is no longer determined by the speed command but only by the number of shots averaged for each datapoint.

The key to the Autoscan2 program is the way in which the laser scan is stopped and later restarted without losing the calibration of the scan:

In the Autoscan program the laser frequency is scanned by counting down the 16 bit counter connected to a 16 bit D/A converter which in turn provides the voltage for the reference cavity Brewster plate galvo drive. The scan counter is decreased at a constant rate. To adjust the timing of the datataking a second counter (the data counter) is loaded with sightly different starting values for each datapoint. Each time the data counter counts to zero the A/D conversion is done on each of the three data channels and results are stored in memory.

In order to stop the scan at each data taking position the scan counter and the datacounter have to be stopped. Since it is not possible to physically stop these counters their values are read and stored in memory and then the output to the D/A converter is disabled to stop the scanning of the laser. Before the output is enabled again, the counters are reloaded with new values, which have to be corrected for delays in the reading process.

The modified parts of the Autoscan program are shown in the following section.

AUTOSCAN2 PROGRAM

by Chris Walker

```
]LIST 13000-13005

 13000  REM

SCANK


 13001 WW = W:W = 18: GOSUB 25000
     :W = WW
 13002  VTAB 23
 13003  INPUT "NUMBER OF SHOTS (P
     OWER OF TWO) ";NN: PRINT
 13004 LL =  INT ( LOG (NN) /  LOG
     (2) + .5): IF LL > 7 THEN 13
     003
 13005  POKE 37483,LL:NN =  INT (
     2 ^ LL): POKE 37482,NN


]

 LIST 33000-33005

 33000  REM

CONT


 33001 WW = W:W = 18: GOSUB 25000
     :W = WW
 33002  VTAB 23
 33003  INPUT "NUMBER OF SHOTS (P
     OWER OF TWO) ";NN: PRINT : PRINT

 33004 LL =  INT ( LOG (NN) /  LOG
     (2) + .5): IF LL > 7 THEN 13
     003
 33005  POKE 37483,LL:NN =  INT (
     2 ^ LL): POKE 37482,NN

]PR#0
```

src.time2 Page 01

```
                              @LST     =1
                              @OBJ     =1000
                              @ORG     =9000
                              ;************************************
                              ;*                                  *
                              ;*  THIS ROUTINE IS A MODIFICATION TO *
                              ;* THE &SCAN PROCEDURE SUPPLIED WITH  *
                              ;* THE AUTOSCAN SYSTEM.  THIS NEW     *
                              ;* CODE ALLOWS THE SCAN TO BE HALTED  *
                              ;* AT EACH DATA COLLECTION POSITION   *
                              ;* SO THAT AS MANY DATA POINTS AS IS  *
                              ;* DESIRED MAY BE TAKEN.              *
                              ;*                                  *
                              ;*  THE MAJOR POINTS OF THIS ROUTINE  *
                              ;* ARE AS FOLLOWS:                    *
                              ;*     1. USER T1 AND DED T1 TIMERS   *
                              ;*        ARE EFFECTIVELY STOPPED.    *
                              ;*        THESE TIMERS CONTROL THE    *
                              ;*        ADVANCE OF THE SCAN AND THE *
                              ;*        DATA TAKING INTERVALS.      *
                              ;*     2. VALUES ARE ADJUSTED AND     *
                              ;*        SAVED SO THAT THE TIMERS CAN *
                              ;*        BE RESTARTED.               *
                              ;*     3. THE DESIRED DATA COLLECTION *
                              ;*        IS THEN PERFORMED.          *
                              ;*     4. THE TWO TIMERS ARE RESTARTED *
                              ;*        AT THE PRECISE POSITION AT  *
                              ;*        WHICH THEY WERE STOPPED, AND *
                              ;*        THE SCAN PROCEEDS TO THE    *
                              ;*        NEXT DATA POINT.            *
                              ;*                                  *
                              ;************************************
                              ;
                              ;    IMPORTANT MEMORY LOCATIONS USED:
                              ;
                              ;       C504,C505 = DED T1 COUNT
                              ;       C506,C507 = DED T1 LATCH
                              ;       C50B      = TIMER CNTR REGISTER
                              ;       C534,C535 = USER T1 COUNT
                              ;       C536,C537 = USER T1 LATCH
                              ;       C53B      = TIMER CNTR REGISTER
                              ;
                              ;
                              ;
                              ;   STOP TIMERS
                              ;
$9000: A9 20                  STOP     LDA #20         ;TURN OFF OUPUT
$9002: 8D 3B C5                        STA $C53B       ;USER T1
$9005: EA                              NOP
$9006: 8D 0B C5                        STA $C50B       ;DED T1
                              ;
                              ;   READ COUNTS AND LATCHES
                              ;
$9009: AD 35 C5                        LDA $C535       ;USER T1 HIGH
$900C: 8D 70 91                        STA UT1H
```

```
                        src.time2  Page 02

$900F: AD 34 C5               LDA $C534       ;USER T1 LOW
$9012: 8D 71 91               STA UT1L
$9015: AD 05 C5               LDA $C505       ;DED T1 HIGH
$9018: 8D 72 91               STA DT1H
$901B: AD 04 C5               LDA $C504       ;DED T1 LOW
$901E: 8D 73 91               STA DT1L
$9021: AD 36 C5               LDA $C536       ;USER T1 LATCH
$9024: 8D 75 91               STA LATUL
$9027: AD 37 C5               LDA $C537
$902A: 8D 74 91               STA LATUH
$902D: AD 06 C5               LDA $C506       ;DED T1 LATCH
$9030: 8D 77 91               STA LATDL
$9033: AD 07 C5               LDA $C507
$9036: 8D 76 91               STA LATDH
                  ;
                  ;    ADJUST THE COUNTS
                  ;
$9039: AD 70 91               LDA UT1H        ;CHECK FOR
$903C: C9 FF                  CMP #FF         ;READ ON ROLL
$903E: D0 05                  BNE ROLL
$9040: A9 00                  LDA #00
$9042: 8D 70 91               STA UT1H
$9045: AD 70 91   ROLL        LDA UT1H        ;CORRECT FOR
$9048: D0 14                  BNE OK          ;ROLLOVERS
$904A: AD 71 91               LDA UT1L        ;THAT OCCUR
$904D: 10 0F                  BPL OK          ;DURING READ
$904F: 18                     CLC
$9050: 69 01                  ADC #01
$9052: F0 0A                  BEQ OK
$9054: 18                     CLC
$9055: 69 08                  ADC #08
$9057: 30 05                  BMI OK
$9059: A9 02                  LDA #02
$905B: 8D 70 91               STA UT1H
$905E: AD 71 91   OK          LDA UT1L        ;CORRECT FOR
$9061: 18                     CLC     ;DELAYS IN THE
$9062: 69 08                  ADC #08         ;READING STEPS
$9064: C9 FF                  CMP #FF
$9066: D0 0B                  BNE OK2
$9068: CE 70 91               DEC UT1H
$906B: AD 7A 91               LDA SAVE
$906E: F0 03                  BEQ OK2
$9070: CE 70 91               DEC UT1H
$9073: AD 71 91   OK2         LDA UT1L
$9076: 18                     CLC
$9077: 69 3F                  ADC #3F
$9079: 8D 71 91               STA UT1L
$907C: AD 70 91               LDA UT1H
$907F: 69 00                  ADC #00
$9081: 8D 70 91               STA UT1H
$9084: AD 73 91               LDA DT1L        ;SAME PROCEDURE
$9087: 18                     CLC     ;FOR DED TIMER
$9088: 69 08                  ADC #08
$908A: 18                     CLC
$908B: 69 8B                  ADC #8B         ;2F
$908D: 8D 73 91               STA DT1L
```

```
$9090: AD 72 91              LDA DT1H
$9093: 69 FD                 ADC #FD          ;00
$9095: 8D 72 91              STA DT1H
$9098: AD 70 91              LDA UT1H
$909B: 8D 7A 91              STA SAVE
                    ;
                    ;   DATA COLLECTION PERFORMED
                    ;     AT THIS POINT.
                    ;
$909E: 4C 00 91              JMP SKIP
$90A1: AD 70 91              LDA UT1H         ;PRINT UT1
$90A4: 20 DA FD              JSR $FDDA
$90A7: AD 71 91              LDA UT1L
$90AA: 20 DA FD              JSR $FDDA
$90AD: A9 A0                 LDA #A0
$90AF: 20 ED FD              JSR $FDED
$90B2: AD 74 91              LDA LATUH        ;PRINT LATU
$90B5: 20 DA FD              JSR $FDDA
$90B8: AD 75 91              LDA LATUL
$90BB: 20 DA FD              JSR $FDDA
$90BE: A9 8D                 LDA #8D
$90C0: 20 ED FD              JSR $FDED
$90C3: A9 A0                 LDA #A0
$90C5: 20 ED FD              JSR $FDED
$90C8: AD 72 91              LDA DT1H         ;PRINT DT1
$90CB: 20 DA FD              JSR $FDDA
$90CE: AD 73 91              LDA DT1L
$90D1: 20 DA FD              JSR $FDDA
$90D4: A9 A0                 LDA #A0
$90D6: 20 ED FD              JSR $FDED
$90D9: AD 76 91              LDA LATDH        ;PRINT LATD
$90DC: 20 DA FD              JSR $FDDA
$90DF: AD 77 91              LDA LATDL
$90E2: 20 DA FD              JSR $FDDA
$90E5: A9 A0                 LDA #A0
$90E7: 20 ED FD              JSR $FDED
$90EA: A9 A0                 LDA #A0
$90EC: 20 ED FD              JSR $FDED
$90EF: AD 39 C5              LDA $C539
$90F2: 20 DA FD              JSR $FDDA
$90F5: AD 38 C5              LDA $C538        ;PRINT UT2L
$90F8: 20 DA FD              JSR $FDDA
$90FB: A9 8D                 LDA #8D
$90FD: 20 ED FD              JSR $FDED
                    ;
                    ;   CHECK FOR MISSED T2 PULSES
                    ;
$9100: AD 75 91     SKIP     LDA LATUL
$9103: 18                    CLC
$9104: 69 02                 ADC #02
$9106: 8D 78 91              STA TEMP
$9109: AD 74 91              LDA LATUH
$910C: 69 00                 ADC #00
$910E: 8D 79 91              STA TEMP2
$9111: AD 71 91              LDA UT1L         ;CHECK FOR
$9114: 38                    SEC      ;USER T1>LATCH
```

```
                         src.time2  Page 04

$9115: ED 78 91                   SBC TEMP
$9118: 8D 78 91                   STA TEMP
$911B: AD 70 91                   LDA UT1H
$911E: ED 79 91                   SBC TEMP2
$9121: D0 11                      BNE RET
$9123: AD 78 91                   LDA TEMP          ;PULSE FOR
$9126: C9 47                      CMP #47           ;34<TEMP<43
$9128: B0 0A                      BCS RET
$912A: C9 34                      CMP #34
$912C: 90 06                      BCC RET
$912E: EE 72 91                   INC DT1H
$9131: EE 72 91                   INC DT1H
$9134: 60                RET      RTS
                         ;
                         ;    RESTART THE TIMERS
                         ;
$9135: AD 71 91          RESTART LDA UT1L           ;RELOAD USER T1
$9138: 8D 34 C5                  STA $C534
$913B: AD 70 91                  LDA UT1H
$913E: 8D 35 C5                  STA $C535          ;TIMER STARTED
$9141: AD 75 91                  LDA LATUL          ;RELOAD THE
$9144: 8D 36 C5                  STA $C536          ;LATCH
$9147: AD 74 91                  LDA LATUH
$914A: 8D 37 C5                  STA $C537
$914D: AD 73 91                  LDA DT1L           ;RELOAD DED T1
$9150: 8D 04 C5                  STA $C504
$9153: AD 72 91                  LDA DT1H
$9156: 8D 05 C5                  STA $C505          ;TIMER STARTED
$9159: AD 77 91                  LDA LATDL          ;LATCH RELOAD
$915C: 8D 06 C5                  STA $C506
$915F: AD 76 91                  LDA LATDH
$9162: 8D 07 C5                  STA $C507
                         ;
                         ;    OUTPUTS REACTIVATED
                         ;
$9165: A9 E0                     LDA #E0
$9167: 8D 3B C5                  STA $C53B          ;USER T1 SET
$916A: A9 40                     LDA #40
$916C: 8D 0B C5                  STA $C50B          ;DED T1 SET
$916F: 60                        RTS
                         ;
                         ;VARIABLES
                         ;
$9170:                   UT1H     .00      ;COUNT STORAGE SPACE
$9171:                   UT1L     .00
$9172:                   DT1H     .00
$9173:                   DT1L     .00
$9174:                   LATUH    .00      ;LATCH STORAGE SPACE
$9175:                   LATUL    .00
$9176:                   LATDH    .00
$9177:                   LATDL    .00
$9178:                   TEMP     .00      ;TEMPORARY STORAGE
$9179:                   TEMP2    .00
$917A:                   SAVE     .00
```

```
                              src.adc.chg  Page 01


                              @LST     =1
                              @ORG     =$9200
                              ;***********************************
                              ;*                                 *
                              ;*       DATA TAKING ROUTINE       *
                              ;*                                 *
                              ;* THIS ROUTINE READS THE INPUT FROM *
                              ;* THE ADC DURING THE SCAN.        *
                              ;*                                 *
                              ;* FOR EACH DATA TAKING POSITION IN  *
                              ;* THE SCAN, 'NUMB' DATA POINTS ARE  *
                              ;* TAKEN AND AVERAGED TO GIVE THE  *
                              ;* OVERALL RESULT.                 *
                              ;*   NUMB MUST BE POWER OF TWO     *
                              ;*   LOGN IS THEN LOG(2) OF NUMB   *
                              ;***********************************
                              ;
$9200: AD 6A 92               COLLECT LDA NUMB          ;INIT POINT
$9203: 8D 6C 92                       STA COUNT         ;COUNTER
$9206: A9 00                          LDA #00
$9208: A2 02                          LDX #02
$920A: 9D CF 92               ZERO    STA SUM0    ,X    ;SET SUMS TO
$920D: 9D D2 92                       STA SUM1    ,X    ;ZERO
$9210: 9D D5 92                       STA SUM2    ,X
$9213: CA                             DEX
$9214: 10 F4                          BPL ZERO
                              ;
                              ;    WAIT FOR VALID DATA POINT
                              ;
                              ;  THE PROGRAM MUST WAIT AT THIS POINT
                              ;  UNTIL A SIGNAL IS RECEIVED FROM THE
                              ;  BOXCARR INDICATING THAT A LASER
                              ;  PULSE HAS OCCURRED AND THE RESULT
                              ;  IS AVAILABLE
                              ;
$9216: 20 08 93               WAITPT  JSR WAIT
                              ;
                              ;    READ DATA
                              ;      ROUTINE TAKEN FROM AUTOSCAN
                              ;      AND MODIFIED AND REARRANGED
                              ;
                              ;
$9219: A2 00                  SWST01  LDX #00           ;INDEX TO DATA
$921B: BD 00 14               SWST03  LDA $1400   ,X    ;FLAG FOR BRNCH
$921E: F0 09                          BEQ SWST04        ;DON'T TAKE PT.
$9220: BD 03 14                       LDA $1403   ,X    :SELECT INPUT
$9223: 8D 31 C5                       STA $C531
$9226: 20 73 92                       JSR RUNADC        ;READ ADC
$9229: E8                     SWST04  INX
$922A: E0 03                          CPX #03
$922C: D0 ED                          BNE SWST03
$922E: 20 62 15                       JSR $1562         ;CHECK VET
$9231: 20 AE 92                       JSR PROCESS       ;PROCESS DATA
$9234: CE 6C 92                       DEC COUNT         ;ENOUGH PTS?
$9237: D0 DD                          BNE WAITPT        ;NO, LOOP.
```

```
$9239: 20 D8 92                JSR FINAL
$923C: A2 00                   LDX #00
$923E: BD 00 14      LOOPX     LDA $1400    ,X
$9241: F0 21                   BEQ NEXTX
$9243: AD 07 14                LDA $1407          ;YES, SAVE
$9246: 85 EF                   STA $EF            ;THE RESULT
$9248: 20 C0 16                JSR $16C0
$924B: BD 6D 92                LDA RESULTL,X
$924E: 91 FE                   STA ($FE     ),Y
$9250: E6 FE                   INC $FE
$9252: BD 70 92                LDA RESULTH,X
$9255: 91 FE                   STA ($FE     ),Y
$9257: E6 FE                   INC $FE
$9259: EE 06 14                INC $1406
$925C: EE 06 14                INC $1406
$925F: D0 03                   BNE NEXTX
$9261: EE 07 14                INC $1407
$9264: E8            NEXTX     INX
$9265: E0 03                   CPX #03
$9267: D0 D5                   BNE LOOPX
$9269: 60                      RTS
                     ;
$926A:               NUMB      .08
$926B:               LOGN      .03
$926C:               COUNT     .00
$926D:               RESULTL   .00 00 00
$9270:               RESULTH   .00 00 00
                     ;
                     ;    SLIGHTLY CHANGED ADC READING
                     ;    ROUTINE COPIED FROM AUTOSCAN
                     ;
$9273: C9 08         RUNADC    CMP #08
$9275: 90 1A                   BCC ADCON0
$9277: AD 30 C5                LDA $C530
$927A: 8D 72 C5                STA $C572
$927D: A9 10                   LDA #10
$927F: 2C 3D C5      ADCON1    BIT $C53D
$9282: F0 FB                   BEQ ADCON1
$9284: AD 73 C5                LDA $C573
$9287: 9D A8 92                STA DATAL    ,X
$928A: AD 72 C5                LDA $C572
$928D: 9D AB 92                STA DATAH    ,X
$9290: 60                      RTS
$9291: AD 00 C5      ADCON0    LDA $C500
$9294: 8D 10 C5                STA $C510
$9297: A9 01                   LDA #01
$9299: 20 A0 10                JSR $10A0
$929C: A9 00                   LDA #00
$929E: 9D A8 92                STA DATAL    ,X
$92A1: AD 10 C5                LDA $C510
$92A4: 9D AB 92                STA DATAH    ,X
$92A7: 60                      RTS
$92A8:               DATAL     .00 00 00
$92AB:               DATAH     .00 00 00
                     ;
                     ;    PROCESS THE INPUT DATA
```

```
                        ;
                        ; PRESENTLY, THE ONLY PROCESSING IS
                        ; SIMPLY TO COMPUTE THE SUM OF ALL THE
                        ; INPUT VALUES SO THAT AN AVERAGE CAN
                        ; BE COMPUTED.
                        ;
$92AE: A2 02            PROCESS LDX #02         ;SUMMING
$92B0: BD CF 92         ADDON   LDA SUM0    ,X  ;3-BYTE ADD
$92B3: 18                       CLC     ;ON ALL 3 OF
$92B4: 7D A8 92                 ADC DATAL   ,X  ;THE INPUTS
$92B7: 9D CF 92                 STA SUM0    ,X
$92BA: BD D2 92                 LDA SUM1    ,X
$92BD: 7D AB 92                 ADC DATAH   ,X
$92C0: 9D D2 92                 STA SUM1    ,X
$92C3: BD D5 92                 LDA SUM2    ,X
$92C6: 69 00                    ADC #00
$92C8: 9D D5 92                 STA SUM2    ,X
$92CB: CA                       DEX
$92CC: 10 E2                    BPL ADDON
$92CE: 60                       RTS
                        ;
                        ;
$92CF:                  SUM0    .00 00 00
$92D2:                  SUM1    .00 00 00
$92D5:                  SUM2    .00 00 00
                        ;
                        ;
                        ;   FINALIZE THE RESULT
                        ;
                        ; THE AVERAGE IS COMPUTED THROUGH A
                        ; DIVISION OF THE SUMS.
                        ;
$92D8: A2 02            FINAL   LDX #02         ;INDEX TO CHAN.
$92DA: AC 6B 92         NEXTDIV LDY LOGN        ;BIT COUNT
$92DD: F0 19                    BEQ DONE
$92DF: 18               DIVID   CLC     ;ROTATE THE
$92E0: BD D5 92                 LDA SUM2    ,X  ;SUMS RIGHT TO
$92E3: 6A                       ROR     ;PERFORM THE
$92E4: 9D D5 92                 STA SUM2    ,X  ;DIVISION
$92E7: BD D2 92                 LDA SUM1    ,X
$92EA: 6A                       ROR
$92EB: 9D D2 92                 STA SUM1    ,X
$92EE: BD CF 92                 LDA SUM0    ,X
$92F1: 6A                       ROR
$92F2: 9D CF 92                 STA SUM0    ,X
$92F5: 88                       DEY
$92F6: D0 E7                    BNE DIVID
$92F8: BD CF 92         DONE    LDA SUM0    ,X  ;TRANSFER THE
$92FB: 9D 6D 92                 STA RESULTL,X   ;RESULTS
$92FE: BD D2 92                 LDA SUM1    ,X
$9301: 9D 70 92                 STA RESULTH,X
$9304: CA                       DEX     ;NEXT CHAN.
$9305: 10 D3                    BPL NEXTDIV
$9307: 60                       RTS
                        ;
                        ;   THIS IS THE POSITION FOR THE
```

```
                        src.adc.chg  Page 04


                        ; SUBROUTINE THAT WAITS FOR THE LASER
                        ; PULSES BEFORE TAKING EACH DATA POINT
                        ;
$9308: 2C 61 C0         WAIT    BIT $C061       ;CHECK SW1 FOR
$930B: 10 FB                    BPL WAIT        ;PULSE RECEIVED
$930D: 60                       RTS
```

```
                        src.patch  Page 01


                        @LST    =1
                        @OBJ    =143B
                        @ORG    =143B
                        ;************************************
                        ;*                                  *
                        ;*  THIS SHORT ROUTINE REPLACES THE *
                        ;* ORIGINAL DATA COLLECTION PROCEDURE *
                        ;* WITHIN THE &SCAN SUBPROGRAM.  THE *
                        ;* ENTIRE POINT OF THE ROUTINE IS TO *
                        ;* SEND THE PROGRAM TO THE NEW DATA  *
                        ;* COLLECTION ROUTINE.               *
                        ;*                                  *
                        ;************************************
                        ;
$143B: 20 00 90         PATCH   JSR $9000       ;STOP TIMERS
$143E: 20 00 92                 JSR $9200       ;GET DATA
$1441: 20 35 91                 JSR $9135       ;RESTART TIMERS
$1444: 4C 68 14                 JMP $1468       ;SKIP OVER
                                ;UNUSED SPACE
```

Data Transfer to an IBM Compatible Computer

Two ways of transferring data to an IBM computer were implemented by modification of the Autoscan program.

1.) Sending complete datafiles:

After the datataking is finished the data contained in each channel can be send from the memory of the Apple computer to an ASCII file on the IBM computer. This is done with a so-called user subroutine (U2) which is actually a small Basic program that reads the data stored in memory, converts it to ASCII format and send it out through the RS232 port of the Apple computer by calling an assembly language subroutine. A Quickbasic program on the IBM captures the data and writes it to an ASCII file on disk.

2.) Sending data on each laser shot:

If more sophisticated data processing than a simple averaging is desired the collected data can be transferred to an IBM compatible computer on each lasershot. Processing the data on the Apple computer is not feasible, because there is very limited space in memory left after the Autoscan program is loaded and also because programming floating point arithmetic in Apple assembly language is very tedious due to the very limited instruction set of the 6502 microprocessor.

The modified Autoscan program uses the AUX-VIA (versatile interface adapter) in the ring laser interface to send data to the IBM. The RS232 port is used to transmit the information on the scan conditions and the filename etc. A Quickbasic program on the IBM computer captures the data, displays it on a graphics screen and writes it to an ASCII file.

The modified version of the data collection subroutine taken from the Autoscan2 program and the Quickbasic program that captures and processes the data are listed on the next pages.

Autoscan2 modified for data transfer to IBM compatible

by Rainer Beck

```
'****************************************************************************************************************
'APPLE TO IBM DATA TRANSFER FOR NEW DATAFILE FORMAT (WITH LESS HEADER INFO)
'written by RAINER BECK 7-MAY-1989
'****************************************************************************************************************
DIM FI$(0 TO 18)
OPEN "COM1:9600,S,7,2,DS0,CD0,OP0,RB 4000" FOR INPUT AS #1
CONTROLREG = &H3FC:
STARTCODE = INP(CONTROLREG): STOPCODE = STARTCODE AND 253
PRINT "ENTER A PATH FOR DATA STORAGE OR <CR> FOR THE DEFAULT"
INPUT " A:\ "; P$
IF P$ = "" THEN P$ = "A:\"

AGAIN:
PAUSE = 0
OUT CONTROLREG, STARTCODE
INPUT #1, test$: IF test$ = "-2" THEN STOP
IF test$ <> "-1" THEN PRINT "UNEXPECTED DATA ON RS 232 INTERFACE": STOP
INPUT #1, FILENAME$, K0#, LE, DP, IN, ST, CH, KT$
FOR I = 2 TO 7
INPUT #1, FI$(I)
NEXT I
OUT CONTROLREG, STOPCODE: PAUSE = 1:

OPEN P$ + FILENAME$ FOR OUTPUT AS #2
L$ = CHR$(13) + CHR$(10)
PRINT #2, FILENAME$, " TITLE"
PRINT #2, K0#, " STARTING WAVENUMBER"
PRINT #2, LE, " # OF BYTES"
PRINT #2, DP, " # OF DATAPOINTS IN 10 GHZ SCAN"
PRINT #2, IN, " INTERVAL IN MHZ"
PRINT #2, ST, " SCAN SPEED IN SEC/10GHZ"
PRINT #2, CH, " CHANNEL #"
PRINT #2, KT$, " SCAN LENGTH IN CM-1"
PRINT #2, FI$(2), " DATE"
PRINT #2, FI$(3), " SAMPLE"
PRINT #2, FI$(4), " DRIVING PRESSURE FOR JET OR STATIC PRESSURE"
PRINT #2, FI$(5), " BACKGROUND PRESSURE IN MTORR FOR JET EXPERIMENT"
PRINT #2, FI$(6), " NOZZLE DIAMETER IN MICRON"
PRINT #2, FI$(7), " COMMENTS"
PRINT #2, ""

OUT CONTROLREG, STARTCODE: PAUSE = 0:
COUNT = 0
FOR I = 0 TO 1000
NEXT I

STARTLOOP:
IF PAUSE = 0 AND LOC(1) > 3900 THEN OUT CONTROLREG, STOPCODE: PAUSE = 1:
INPUT #1, DATUM: IF DATUM = -1 GOTO EXITLOOP
PRINT #2, DATUM: COUNT = COUNT + 1
IF PAUSE = 1 AND LOC(1) < 10 THEN OUT CONTROLREG, STARTCODE: PAUSE = 0:
GOTO STARTLOOP
EXITLOOP:
OUT CONTROLREG, STOPCODE: PAUSE = 1
CLOSE #2
GOTO AGAIN
END
```

```
'DATA COLLECTION PROGRAM FOR RAMAN LOSS APPARATUS
'
'This program captures data collected by the apple commputer and performs
'various data processing tasks. It also displays data on the PC's screen
'and writes the data to a floppy disk file.

'first the header information is transfered through the serial port COM1:

DIM fi$(0 TO 10)
OPEN "com1:9600,s,7,2,op0,ds0,cd0" FOR INPUT AS #1 LEN - 4000
PRINT "com1 opened"
PRINT "start transfer from apple"
INPUT #1, filename$, e, k0, in: FOR i - 0 TO 10: INPUT #1, fi$(i): NEXT i
PRINT filename$, e, k0, in: FOR i - 0 TO 10: PRINT fi$(i): NEXT i
OPEN "B:" + filename$ FOR OUTPUT AS #2
WRITE #2, filename$: WRITE #2, e: WRITE #2, k0: WRITE #2, in
FOR i - 1 TO 10: WRITE #2, fi$(i): NEXT i
PRINT "header transfered"
CLOSE #1

'initialize some of the variables
count - 0
DIM a(1 TO e, 1 TO 3)

'initialize I/O board
OUT &H303, 145

'set up the graphics screen
SCREEN 2
VIEW (0, 0)-(639, 180)               'the bottom of the screen is reserved for
VIEW PRINT 24 TO 25                  'a wavenuber axis
WINDOW (0, 0)-(639, 8190)

'data transfer starts

DO

FOR j - 1 TO e                          'transfer e shots
FOR k - 1 TO 3                          'for each of the three data channels
'first wait for a trigger signal
DO
test0 - INP(&H302)                      'check bit 0 on port c
IF test0 - 0 GOTO sample
IF test0 - 3 GOTO done
LOOP

sample:
b - INP(&H300)                          'read high byte from port a
OUT &H301, 0: OUT &H301, 255            'send negtive pulse to signal dxtm

DO
test0 - INP(&H302)
IF test0 - 0 GOTO sample1
IF test0 - 3 GOTO done
LOOP

sample1:
c - INP(&H300)                          'read high byte from port a
OUT &H301, 0: OUT &H301, 255            'send dxtm
```

```
a(j, k) = 16 * b + c / 16                'combine high and low byte to 12 bit
                                         'number (0...4095)

NEXT k
NEXT j

'Done with collecting n shots on three channels. Now the processing begins
'to do a least square fit using channels 2 and 3 as x and y data we need
'to calculate the following sums. Note that for some reason the data channels
'2 and 3 are interchanged. What goes into channel 2 of the apple ends up
'in a(j,3) and what goes into data channel 3 of the apple ends up in a(j,2).

sumx = 0: sumy = 0: ratio = 0: sumx2 = 0: sum1 = 0
FOR j = 1 TO e
sumx = sumx + a(j, 3)
sumy = sumy + a(j, 2)
sum1 = sum1 + a(j, 1)
ratio = ratio + a(j, 2) * 2000 / a(j, 3)
NEXT j
data1 = sum1 / e
data2 = sumx / e
data3 = sumy / e
ratio = ratio / e

WRITE #2, data1, data2, data3, ratio

count = count + 1
PSET (count, data3)
PSET (count, ratio + 4095)
IF count = 639 THEN
CLS
count = 0
END IF
LOOP
done:
PRINT "program stopped"
PRINT count; " datapoints were collected and written to b: "; filename$
CLOSE #2
END
```

```
                        @LST     =1
                        @ORG     =$9200
                        ;*************************************
                        ;*                                   *
                        ;*       DATA TAKING ROUTINE         *
                        ;*                                   *
                        ;* THIS ROUTINE READS THE INPUT FROM *
                        ;* THE ADC DURING THE SCAN.          *
                        ;*                                   *
                        ;* FOR EACH DATA TAKING POSITION IN  *
                        ;* THE SCAN, 'NUMB' DATA POINTS ARE  *
                        ;* TAKEN AND AVERAGED TO GIVE THE    *
                        ;* OVERALL RESULT.                   *
                        ;*   NUMB MUST BE POWER OF TWO       *
                        ;*   LOGN IS THEN LOG(2) OF NUMB     *
                        ;*************************************
                        ;
$9200: AD 74 92         COLLECT LDA NUMB          ;INIT POINT
$9203: 8D 76 92                 STA COUNT         ;COUNTER
$9206: A9 00                    LDA #00
$9208: A2 02                    LDX #02
$920A: 9D FB 92         ZERO    STA SUM0    ,X    ;SET SUMS TO
$920D: 9D FE 92                 STA SUM1    ,X    ;ZERO
$9210: 9D 01 93                 STA SUM2    ,X
$9213: CA                       DEX
$9214: 10 F4                    BPL ZERO
                        ;
                        ;    WAIT FOR VALID DATA POINT
                        ;
                        ;  THE PROGRAM MUST WAIT AT THIS POINT
                        ;  UNTIL A SIGNAL IS RECEIVED FROM THE
                        ;  BOXCARR INDICATING THAT A LASER
                        ;  PULSE HAS OCCURRED AND THE RESULT
                        ;  IS AVAILABLE
                        ;
$9216: 20 34 93         WAITPT  JSR WAIT
                        ;
                        ;    READ DATA
                        ;      ROUTINE TAKEN FROM AUTOSCAN
                        ;      AND MODIFIED AND REARRANGED
                        ;
                        ;
$9219: A9 FF                    LDA #FF           ;SET AUX VIA
$921B: 8D 62 C5                 STA $C562         ;ALL PORTS OUT
$921E: A9 80                    LDA #80           ;PUT AND HAND
$9220: 8D 62 C5                 STA $C562         ;SHAKING
$9223: A2 00            SWST01  LDX #00           ;INDEX TO DATA
$9225: BD 00 14         SWST03  LDA $1400   ,X    ;FLAG FOR BRNCH
$9228: F0 09                    BEQ SWST04        ;DON'T TAKE PT.
$922A: BD 03 14                 LDA $1403   ,X    ;SELECT INPUT
$922D: 8D 31 C5                 STA $C531
$9230: 20 7D 92                 JSR RUNADC        ;READ ADC
$9233: E8               SWST04  INX
$9234: E0 03                    CPX #03
$9236: D0 ED                    BNE SWST03
```

```
$9238: 20 62 15              JSR $1562        ;CHECK VET
$923B: 20 B8 92              JSR PROCESS      ;PROCESS DATA
$923E: CE 76 92              DEC COUNT        ;ENOUGH PTS?
$9241: D0 D3                 BNE WAITPT       ;NO, LOOP.
$9243: 20 04 93              JSR FINAL
$9246: A2 00                 LDX #00
$9248: BD 00 14     LOOPX    LDA $1400    ,X
$924B: F0 21                 BEQ NEXTX
$924D: AD 07 14              LDA $1407        ;YES, SAVE
$9250: 85 EF                 STA $EF          :THE RESULT
$9252: 20 C0 16              JSR $16C0
$9255: BD 77 92              LDA RESULTL,X
$9258: 91 FE                 STA ($FE     ),Y
$925A: E6 FE                 INC $FE
$925C: BD 7A 92              LDA RESULTH,X
$925F: 91 FE                 STA ($FE     ),Y
$9261: E6 FE                 INC $FE
$9263: EE 06 14              INC $1406
$9266: EE 06 14              INC $1406
$9269: D0 03                 BNE NEXTX
$926B: EE 07 14              INC $1407
$926E: E8           NEXTX    INX
$926F: E0 03                 CPX #03
$9271: D0 D5                 BNE LOOPX
$9273: 60                    RTS
                    ;
$9274:              NUMB     .08
$9275:              LOGN     .03
$9276:              COUNT    .00
$9277:              RESULTL .00 00 00
$927A:              RESULTH .00 00 00
                    ;
                    ;    SLIGHTLY CHANGED ADC READING
                    ;    ROUTINE COPIED FROM AUTOSCAN
                    ;
$927D: C9 08        RUNADC   CMP #08
$927F: 90 1A                 BCC ADCON0
$9281: AD 30 C5              LDA $C530
$9284: 8D 72 C5              STA $C572
$9287: A9 10                 LDA #10
$9289: 2C 3D C5     ADCON1   BIT $C53D
$928C: F0 FB                 BEQ ADCON1
$928E: AD 73 C5              LDA $C573
$9291: 9D B2 92              STA DATAL   ,X
$9294: AD 72 C5              LDA $C572
$9297: 9D B5 92              STA DATAH   ,X
$929A: 60                    RTS
$929B: AD 00 C5     ADCON0   LDA $C500
$929E: 8D 10 C5              STA $C510
$92A1: A9 01                 LDA #01
$92A3: 20 A0 10              JSR $10A0
$92A6: A9 00                 LDA #00
$92A8: 9D B2 92              STA DATAL   ,X
$92AB: AD 10 C5              LDA $C510
$92AE: 9D B5 92              STA DATAH   ,X
$92B1: 60                    RTS
```

```
$92B2:                DATAL    .00 00 00
$92B5:                DATAH    .00 00 00
                      ;
                      ;   PROCESS THE INPUT DATA
                      ;
                      ; PRESENTLY, THE ONLY PROCESSING IS
                      ; SIMPLY TO COMPUTE THE SUM OF ALL THE
                      ; INPUT VALUES SO THAT AN AVERAGE CAN
                      ; BE COMPUTED.
                      ;
$92B8: A2 02          PROCESS LDX #02          ;SUMMING
$92BA: BD FB 92       ADDON    LDA SUM0    ,X   ;3-BYTE ADD
$92BD: 18                      CLC      ;ON ALL 3 OF
$92BE: 7D B2 92                ADC DATAL   ,X   ;THE INPUTS
$92C1: 9D FB 92                STA SUM0    ,X
$92C4: BD FE 92                LDA SUM1    ,X
$92C7: 7D B5 92                ADC DATAH   ,X
$92CA: 9D FE 92                STA SUM1    ,X
$92CD: BD 01 93                LDA SUM2    ,X
$92D0: 69 00                   ADC #00
$92D2: 9D 01 93                STA SUM2    ,X
$92D5: CA                      DEX
$92D6: 10 E2                   BPL ADDON
                      ;SEND DATA OUT THROUGH AUX PORT USING
                      ;AUX-VIA PORT B0-B7 AND CB1, CB2 FOR
                      ;HANDSHAKING
$92D8: A2 02                   LDX #02
$92DA: 8D 62 C5                STA $C562
$92DD: BD B2 92       HERE     LDA DATAL   ,X
$92E0: 8D 60 C5                STA $C560
$92E3: A9 10          LOOP     LDA #10
$92E5: 2C 6D C5                BIT $C56D
$92E8: F0 F9                   BEQ LOOP
$92EA: BD B2 92                LDA DATAL   ,X
$92ED: 8D 60 C5                STA $C560
$92F0: A9 10          LOOP1    LDA #10
$92F2: 2C 6D C5                BIT $C56D
$92F5: F0 F9                   BEQ LOOP1
$92F7: CA                      DEX
$92F8: 10 E3                   BPL HERE
$92FA: 60                      RTS
                      ;
                      ;
$92FB:                SUM0     .00 00 00
$92FE:                SUM1     .00 00 00
$9301:                SUM2     .00 00 00
                      ;
                      ;
                      ;   FINALIZE THE RESULT
                      ;
                      ; THE AVERAGE IS COMPUTED THROUGH A
                      ; DIVISION OF THE SUMS.
                      ;
$9304: A2 02          FINAL    LDX #02          ;INDEX TO CHAN.
$9306: AC 75 92       NEXTDIV LDY LOGN          ;BIT COUNT
$9309: F0 19                   BEQ DONE
```

adc.chg-new   Page 04

```
$930B: 18          DIVID   CLC       ;ROTATE THE
$930C: BD 01 93            LDA SUM2    ,X    ;SUMS RIGHT TO
$930F: 6A                  ROR       ;PERFORM THE
$9310: 9D 01 93            STA SUM2    ,X    ;DIVISION
$9313: BD FE 92            LDA SUM1    ,X
$9316: 6A                  ROR
$9317: 9D FE 92            STA SUM1    ,X
$931A: BD FB 92            LDA SUM0    ,X
$931D: 6A                  ROR
$931E: 9D FB 92            STA SUM0    ,X
$9321: 88                  DEY
$9322: D0 E7               BNE DIVID
$9324: BD FB 92    DONE    LDA SUM0    ,X    ;TRANSFER THE
$9327: 9D 77 92            STA RESULTL,X    ;RESULTS
$932A: BD FE 92            LDA SUM1    ,X
$932D: 9D 7A 92            STA RESULTH,X
$9330: CA                  DEX       ;NEXT CHAN.
$9331: 10 D3               BPL NEXTDIV
$9333: 60                  RTS
                   ;
                   ;   THIS IS THE POSITION FOR THE
                   ; SUBROUTINE THAT WAITS FOR THE LASER
                   ; PULSES BEFORE TAKING EACH DATA POINT
                   ;
$9334: 2C 61 C0    WAIT    BIT $C061        ;CHECK SW1 FOR
$9337: 10 FB               BPL WAIT         ;PULSE RECEIVED
$9339: 60                  RTS
```

patch2   Page 01

```
                   @LST    =1
                   @ORG    =$149F
$149F: EA                  NOP
$14A0: EA                  NOP
$14A1: EA                  NOP
```

patch1   Page 01

```
                   @LST    =1
                   @ORG    =$1418
$1418: EA                  NOP
$1419: EA                  NOP
$141A: EA                  NOP
```